UNIVERSITAT DE BARCELONA

Departament de Física Aplicada i Òptica

Electron-induced x-ray emission from solids. Simulation and measurements

Xavier Llovet Ximenes

Barcelona, Juny de 1998

UNIVERSITAT DE BARCELONA

Departament de Física Aplicada i Òptica

Electron-induced x-ray emission from solids. Simulation and measurements

Memòria presentada per Xavier Llovet i Ximenes
per a optar al grau de Doctor en Física.

Directors:
Dr. Francesc Salvat Gavaldà
Dr. Alberto Riveros de la Vega

Tutor: Dr. Ignasi Juvells Prades

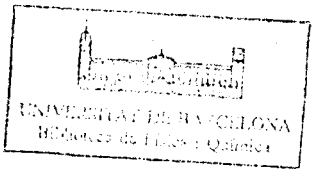

Programa de doctorat:
Micro i Optoelectrònica Física. Bienni 91-93

Barcelona, Juny de 1998

Agraïments

En primer lloc vull mostrar el meu agraïment a Francesc Salvat pel seu suport i dedicació, sense els quals no hagués estat possible la realització d'aquest treball. Al mateix temps, vull agraïr a Alberto Riveros el seu entusiasme i suport, fonamentals tant per a l'acompliment d'aquest treball com per a la meva trajectòria professional. Voldria agraïr, també, la col.laboració i ajut de Claude Merlet, que ha fet possible gran part de les mesures experimentals d'aquesta memòria.

Agraïments a Montserrat Baucells i Montserrat Roura, directora i sots-directora dels Serveis Científico-Tècnics, i a Ramón Fontarnau, cap de la secció de caracterització de materials, per totes les facilitats que m'han donat per a la realització d'aquest treball. Agraïments també a Eduardo Acosta i Enrique Coleoni, que han participat en bona part del desenvolupament d'aquest treball, i a José Maria Fernàndez-Varea, Josep Sempau i Josep Baró, sempre disposats a donar-me un cop de mà. Moltes gràcies a José Maria Fernández-Varea i a Gustavo Castellano per l'atenta lectura del primer esborrany i els seus suggeriments. A Alejandro del Giorgio li agraeixo la seva constant i valuosa assistència informàtica i les idees aportades durant els cafès dels matins. A Javier Garcia-Veigas i Ramón Fontarnau, gràcies per l'ajut en l'utilització del microscopi d'escombrat, i a Joaquim Portillo, disposat sempre a donar-me un cop de mà. Vull mostrar, també, el meu agraïment a tota la gent dels Serveis que m'ha animat durant aquests anys, en especial a Javier Garcia-Veigas i a Núria Cortadellas, amb els quals he compartit moltes estones. Agraïments a Guillaume Bastin per permetre'm presentar dades experimentals no publicades, i a Joan Esteve, per haver fabricat d'algunes de les mostres utilitzades. Agraïexo, també, les facilitats donades pel Departament de Física Aplicada i Òptica.

Finalment, vull agraïr als meus pares tot el suport que m'han donat, no només durant el doctorat, sino des que vaig començar la llicenciatura. Un petó a la Natalie pel seu constant suport i estimació.

Resum

Introducció

L'espectre de raigs x que emet un sólid quan es bombardeja amb un feix d'electrons proporciona informació sobre la composició química de la zona irradiada del sòlid. Per tal d'obtenir la composició a partir de l'intensitat de raigs x s'ha de conéixer, entre d'altres quantitats, la distribució d' ionitzacions produïda pel feix incident en funció de la profunditat. Per a materials homogenis (dins de l'abast de penetració dels electrons), la distribució d'ionitzacions en profundiatat es coneix relativament bé ja que hom disposa de dades experimentals per a diferents materials i energies. Això permet convertir l'intensitat de raigs x a concentració amb algorismes analítics, relativament simples. Tanmateix, la quantificació de mostres no homogènies, com ara capes primes dipositades en substrats, multicapes o partícules petites i inclusions, és difícil degut a la manca de coneixement de la distribució d'ionitzacions. Aquesta distribucició es pot obtenir també mitjançant métodes de càlcul sofisticats, com ara la simulació Monte Carlo (MC) o resolen l'equació de transport. Obviament, els resultats d'aquests càlculs depenen fortament de la validesa de les diferents seccions eficaces adoptades per descriure l'interacció dels electrons i fotons en el material.

En aquest treball, s'ha desenvolupat un programa de simulació MC per calcular l'espectre de raigs x que genera un sólid bombardejat amb un feix d'electrons de pocs keV. Al mateix temps, el programa ens proporciona quantitats d'interès com a ara la distribució d'ionitzacions en profunditat, etc.. Al mateix temps, s'han realitzat una sèrie de mesures experimentals amb una microsonda d'electrons, que ens permeten per una banda, validar el programa de simulació, i per altra, obtenir informació d'interès pràctic pels mètodes de microanàlisi convencional, especialment pel que fa a l'anàlisi de mostres no homogènies.

En el capítol 1 es descriuen els diferents mecanismes d'interacció dels electrons i fotons amb la matèria, així com les diferents seccions eficaces utilitzades per a descriure aquestes interaccions. En el capítol 2 es descriuen els principis de la simulació MC, en particular pel que fa a al paquet de subrutines PENELOPE, que ha estat la base de la simulació desenvolupada en aquest treball. En el capítol 3 es descriuen les característiques de la microsonda d'electrons utilitzada, una CAMECA model SX50, en especial pel que fa als espectròmetres de raigs x. En el capítol 4 es descriuen i presenten noves mesures experimentals de la secció eficaç (total) d'ionització, necesària per a la simulació dels raigs x característics. En el capítol 5 s'estudia la distribució d'ionitzacions en funció de la profunditat, en particular el seu valor a la superf'iicie. En el capítol 6, es descriu la simulació i mesura d'espectres de raigs x.

Resultats

Les possibles interaccions dels electrons amb la matèria són la dispersió elàstica, les col.lisions inelàstiques i l'emissió de radiació de frenat (emissió de bremsstrahlung). Tanmateix, en el rang d'energies d'interès per aquest treball, el poder de frenat associat a l'emissió de bremsstrahlung es molt petit, en comparació amb els altres mecanismes d'interacció, i per tant es pot despreciar quan es simulen les trajectòries dels electrons en el material.

La dispersió elàstica es descriu com la dispersió d'un projectil dins del camp electrostàtic de l' àtom fitó. La secció eficaç diferencial per dispersió elàstica s'obté resolen numèricament l'equació de Dirac pel moviment del projectil en el camp del fitó. Per tal de simplificar els càlculs que s'han de fer durant una simulació, sovint s'utilitzen expressions analítiques per a descriure la dispersió elàstica, com ara la fórmula de Wentzel. Tanmateix, aquesta expressió només és vàlida per a materials amb números atòmics relativament petits i energies moderadament altes. Relacionats amb la dispersió elàstica es defineixen quantitats d'interès per a la simulació, com ara el recorreguts lliure de transport.

Les colisions inelàstiques són aquelles en les quals l'àtom fitó queda en un estat excitat, és a dir, part de l'energia cinètica dels electrons incidents es transfereix als electrons atòmics. Les col.lisions inelàstiques inclouen l'excitació d'electrons en la banda de conducció o valència, excitació de plasmons i ionització de capes lligades. Per a descriure les col.lisions inelàstiques, la pràctica habitual consisteix en utilitzar la primera aproximació de Born, en la qual l'estat inicial i final del projectil es tracten com a ones planes. Aquest formalisme requereix el coneixement de l'anomenada intensitat d'oscil.lador generalitzada, una quantitat que es pot interpretar com el número efectiu d'electrons que participen en l'interacció inelàstica. L'intensitat d'oscil.lador generalitzada, en funció de l'energia i el moment transferit, es coneix com la superfície de Bethe. Malauradament, la superfície de Bethe només es pot calcular analíticament per l'àtom d'higróden. Per tant, a la pràctica la intensitat d'oscil.lador generalitzada es calcula amb métodes aproximats. En el límit de transferències de moment petites, la intensitat d'oscil.lador generalitzada coincideix amb la intensitat d'oscil.lador óptica, que alhora es proporcional a la secció eficaç d'efecte fotoelèctric. Utilitzant aquesta informació, i les propietats de la superfície de Bethe per altes transferencies de moment, es pot reconstruïr la superfície de Bethe i per tant avaluar la secció eficaç de col.lisions inelàstiques i quantitats com ara el poder de frenat. Aquesta darrera quantitat representa la pèrdua mitja d'energia del electrons per unitat de camí recorregut. En moltes simulacions, l'efecte promig de la pèrdua d'energia dels electrons es descriu mitjançant l'aproximació de pèrdues contínues. Tanmateix, aquesta aproximació no té en compte el fet que els electrons perden energia discretament i per tant, si bé pot reproduïr quantitats globals com ara el coeficient de

retrodifusió, l'aproximació de pèrdues contínues no reprodueix correctament quantitats com ara la distribució d'energia d'electrons transmesos per una làmina prima.

Pel que fa al fotons, els mecanismes d'interacció són la dispersió Compton (incoherent), la dispersió Rayleigh (coherent) i l'absorció fotoelèctrica. Aquests mecanismes estàn relacionats amb els coeficients d'absorció màssics. En mostres sota l'impacte d'un feix d'electrons, els fotons s'originen per relaxació atòmica després de la creació d'una vacant en una capa atòmica, i per l'emissió de bremsstrahlung. Encara que aquests dos processos són, en el rang d'energies considerat, molt poc probables, i per tant poc significatius en el procés de frenat dels electrons, són els dos processos responsables de l'emissió de raigs x, i per tant, la base de la microanàlisi quantitativa. Per tant, si hom vol reproduïr acuradament un espectre de raigs x haurà d'utilitzar seccions eficaces acurades per a aquests dos processos. Donat que són processos molt poc probables, es necessita utilitzar tècniques de reducció de variança per tal d'augmentar l'eficiència de la simulació. Així, per a poder simular ionitzacions de capes lligades, sovint s'utilitza la secció eficaç total d'ionització i es calcula el nombre d'ionitzacions promig que ocorren en un determinat interval de la trajectòria.

Per calcular seccions eficaces d'ionització hi ha diverses fórmules analítiques que per la seva simplicitat s'utilitzen habitualment en simulació. La majoria d'elles estàn basades en la fórmula de Bethe (Powell, 1976), que fou desenvolupada en la primera aproximació de Born, modificades empiríricament per tal d'extendre en el rang de validesa prop del llindar d'ionització (p.e. Worthington-Tomlin, 1965). Per altra banda, també hi ha formulacions semiclàssiques, com ara la fórmula de Gryzinski (1965). Recentment Mayol i Salvat (1990) han proposat un model de secció eficaç d'ionització que utilitza informació óptica per calcular la intensitat d'oscil.lador generalitzada.

Pel que fa a la secció eficaç d'emissió de bremsstrahlung, hom troba a la literatura les fórmules de Bethe-Heitler (1934), modificada per Salvat i Fernández-Varea (1992) i la fórmula de Kirkpatrick-Wiedmann-Statham (p.e. Statham, 1976). Aquests dos models es poden incorporar en un programa de simulació amb relativa facilitat. La fórmula de Bethe-Heitler modificada reprodueix correctament el poder de frenat calculat per Kissel et al. (1983). Aquests càlculs, d'ones parcials, es consideren els més acurats dels que hom disposa en l'actualitat. Malauradament, la fórmula de Bethe-Heitler no inclou la distribució angular dels fotons emesos, i per tant a l'hora de simular el fotó emés, hom ha d'utilitzar alguna altra distribució, com ara la distribució dipolar. Aquesta distribució dona resultats raonables per energies per sobre del 1 MeV però és incorrecta per electrons de baixa energia, que són els que ens interessen en aquest treball. Per altra banda, la distribució de Kirkpatrick-Wiedmann-Statham sobreestima els poder de frenat calculats per Kissel et al. (1983), com ja ha sigut apuntat per alguns autors. Sorprenentment aquesta distribució reproduiex correctament la dependència angular dels càlculs

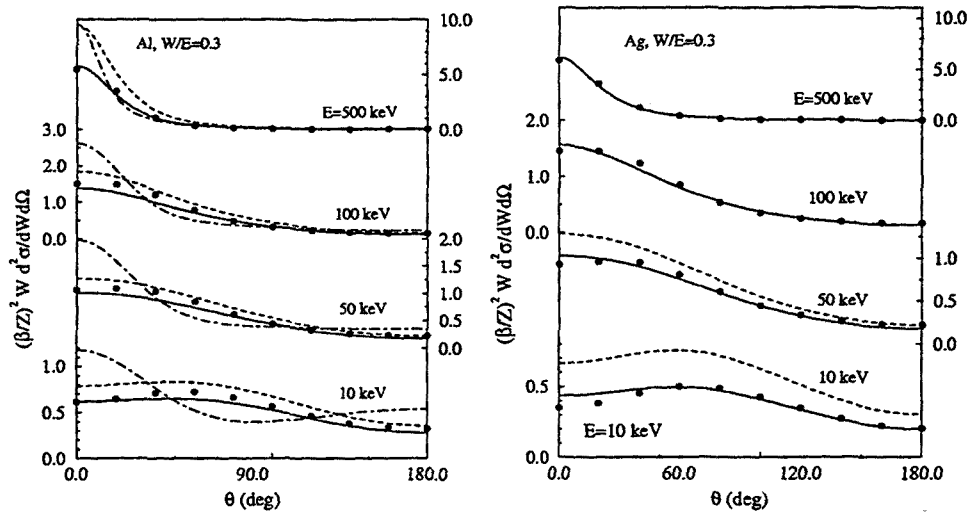

Figura 1. Secció eficaç diferencial d'emissió de bremsstrahlung per Al i Ag. La línia de punts representa la fórmula de Bethe-Heitler modificada, amb una distribució angular dipolar; la l'iinia discontinua es la distribució de Kirkpatrick-Wiedmann-Statham; la l'iinia contínua representa el model proposat, és a dir, la combinació de la fórmula de Bethe-Heitler modifcada i la distribució angular de Kirkpatrick-Wiedmann-Statham adequadament normalitzada. Els punts són els cálculs de Kissel et al. (1983).

de Kissel et al. (1983). Per tant, proposem la la utilització d'un nou model d'emissió de bremmstrahlung que consisteix en utilitzar la fórmula de Bethe-Heitler modificada per descriure la pèrdua d'energia i la fórmula de Kirkpatrick-Wiedmann-Statham, normlalitzada a l'unitat, per descriure la distribució angular dels fotons emesos. D'aquesta manera, es reprodueïxen correctament els càlculs efectuats per Kissel et al. (1983), tal com mostra la Fig. 1. Per altra banda, aquest model es pot implementar amb relativa facilitat en un programa de simulació.

La simulació MC consisteix en la generació numèrica de les trajectòries de les partícules dins del material. Cada trajectòria es vista com una seqüència de "vols lliures" que acaben amb un event de dispersió, on la partícula perd energia i canvia de direcció de moviment i pot generar una partícula secundària, com ara un electró o un raig x. La trajectòria d'una partícula acaba quan aquesta perd tota la seva energia o escapa del material. Les quantitats macroscòpiques d'interès es calculen promitjan sobre un nombre gran de trajectòries. Un mètode de MC particular queda especificat per les diferents seccions eficaces diferencials utilitzads per descriure els diferents mecanismes d'interacció i per l'algorisme de generació de trajectòries.

El conjunt de subrutines PENELOPE (Salvat et al., 1996) permeten simular el transport d'electrons, fotons i positrons, en materials arbitraris, per energies que van des de 1 keV fins 1 GeV. Les seccions eficaces implementades a PENELOPE són funcions

analítiques de l'angle de dispersió i la pèrdua d'energia, físicament plausibles, que permeten el sorteig de l'angle de dispersió i la pèrdua d'energia d'una manera analítica, evitant els errors que es poden derivar del mètodes d'interpolació numèrica. Encara que aquestes seccions eficaces són aproximacions de les reals, els resultats obtinguts són suficientment acurats, sempre i quan la dispersió sigui múltiple, és a dir, hi hagi de l'ordre d'unes 20 col.lisions o més. La dispersió elàstica s'expressa com una combinació de la secció eficaç diferencial de Wentzel i un procés de dispersió a angle fixat. Aquesta combinació conté tres paràmetres que es calculen de tal manera que el recorregut lliure entre col.lisions i el primer i segon recorreguts lliures de transport donin el mateix resultat que calculant-los amb un mètode d'ones parcials (Mayol i Salvat, 1997). La secció eficaç diferencial per col.lisions inelàstiques es basa en un model simple d'intensitat d'oscil.lador generalitzada proposat per Liljequist (1983). Aquest model associa un oscil.lador a cada capa atòmica amb una intensitat igual al número d'electrons en la capa i una energia de resonància proporcional a l'energia de lligam de la capa. Pel que fa a les interaccions de fotons amb la matèria, la secció eficaç diferencial per dispersió Rayleigh ve donada per la fórmula de Thompson multiplicada pel factor de forma atòmic. La dispersió Compton es calcula a partir de l'aproximació d'impuls, que conté el perfil Compton.

Per tal de demostrar la validesa de les seccions eficaces implementades en PENELOPE, pel que fa a la generació de trajectòries d'electrons en el rang d'energies d'interès, s'ha simulat el coeficient de retrodifusió i la dosi dipositada en funció de la profunditat i lateral, per a diversos materials i energies. Els resultats s'han comparat amb dades experimentals tretes de la literatura. L'acord entre la simulació i experiment és molt satisfactori (Fig. 2).

La microsonda d'electrons és un instrument que ens permet bombardejar una mostra amb un feix d'electrons focalitzat i enregistrar l'espectre de raigs x que emet el sólid, en una determinada direcció. Consta bàsicament d'un canó d'electrons i un (o varis) espectrómetres de raigs x, que poden ser de dos tipus. Per una banda hi ha els detectors d'estat sólid, com ara Si(Li), que s'anomenen dispersius en energia. Per altra banda hi ha els espectrómetres dispersius en longitud d'ona, que consisteixen en un cristall monocromador i un comptador proporcional. En aquest treball, s'han realitzat les mesures amb una microsonda d'electrons CAMECA SX50, equipada amb quatre espectroèmetres dispersius en longitud d'ona i un espectròmetre dispersiu en energia, pertanyent als Serveis Científic-Tècnics de la Universitat de Barcelona. Pel que fa al detector d'estat sòlid, s'ha determinat experimentalment la seva resolució en funció de l'energia del raig x. Al mateix temps, s'ha evaluat la seva eficiència calculant l'atenuació a les diferents finestres situades a l'entrada del detector.

S'ha determinat experimentalment la secció eficaç d'ionització per la capa K del Ni,

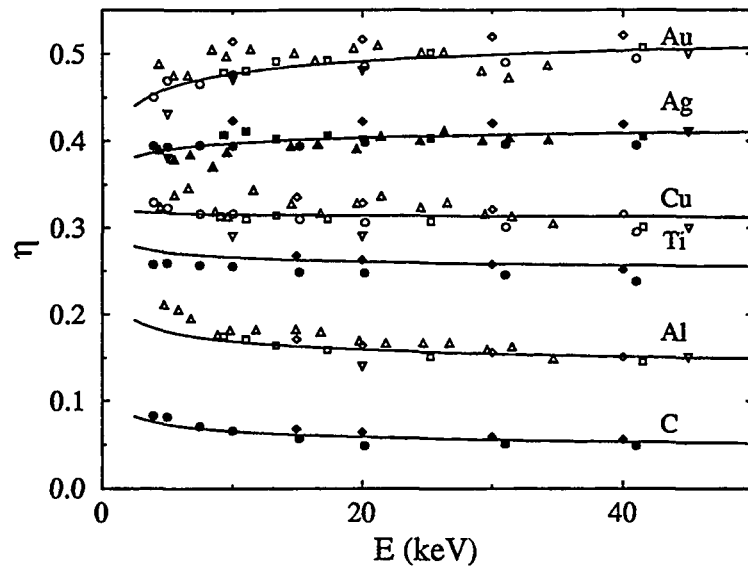

Figura 2. Coeficient de retrodifusió en funció de l'energia del feix incident. Els simbols són dades experimentals de diversos autors. Les línies sòlides son els resultats de la simulació.

Cr i Cu a partir de l'intensitat de raigs x que genera una làmina prima de cada material. Les llàmines primes s'han preparat per evaporació térmica dels esmentats materials en reixetes de TEM, on prèviament s'ha dipositat un film de carboni, d'uns 30 nm de gruix. Les intensitats de raigs x s'han mesurat amb l'espetrómetre dispersiu en longitud d'ona, utilitant els cristalls LiF i PET. La secció eficaç d'ionització és proporcional a l'intensitat de raigs x que genera la làmina del material, sempre i quan aquesta sigui molt prima, és a dir, el feix d'electrons no es dispersi en atravessar-la i els electrons no perdin energia apreciablement. En aquest treball, s'han utilitzat làmines de gruixos de l'ordre de 3-6 nm, que pels materials emprats i les capes atomiques ionitzades, garanteixen els esmentats requeriments. Això s'ha comprobat mitjançant una sèrie de simulacions utilitzant PENELOPE. La conversió de l'intensitat de raigs x a secció eficaç, en valor absolut, requereix conéixer del corrent d'electrons incident, el gruix del film, el rendiment de fluorescència, la fracció de línia, l'eficiència del detector i l'angle sòlid del detector i d'altres. El gruix dels films s'ha determinat mesurant la k-ratio, en funció de l'energia, per als mateixos films dipositats en un substrat de nombre atòmic semblant i composició coneguda. En aquestes condicions, es possible determinar el gruix del film utilitzant els mètodes convencionals de microanàlisi, amb una precisió de l'ordre del 5%. En aquest treball, s'ha utilitzat el procediment desenvolupat per Merlet (1995). L'eficiència de l'espectròmetre dispersiu en longitud d'ona, s'ha determinat amb dades mesurades amb el detector Si(Li), del qual en sabem, amb bona precisió, la seva eficiència i angle sòlid de detecció. Els rendiments de fluorescència i fracció de línia han estat trets de la literatura. El corrent d'electrons incident ha estat mesurat amb una caixa de Faraday col.locada al costat de la làmina autosuportada.

Els resultats obtinguts proporcionen una dependència en l'energia de la secció eficaç d'una incertesa del 3%. La transformació a secció eficaç, en unitats absolutes, incrementa l'incertesa de la mesura a un 12%. La comparació entre les dades experimentals i les fórmules analítiques o models teòrics confirma que el model proposat per Mayol i Salvat (1990) és el que millor descriu la dependència de la secció eficaç amb l'energia. Tot i que, en valor absolut, és difícil treure conclusions definitives respecte l'acuracitat de les diverses fórmules i models degut als errors experimentals, la base física del model de Mayol i Salvat i l'acord amb les mesures experimentals pel que fa a la seva dependència amb l'enegia, fan que adoptem aquest model per a la majoria de simulacions que es duran a terme en aquest treball (Fig. 3).

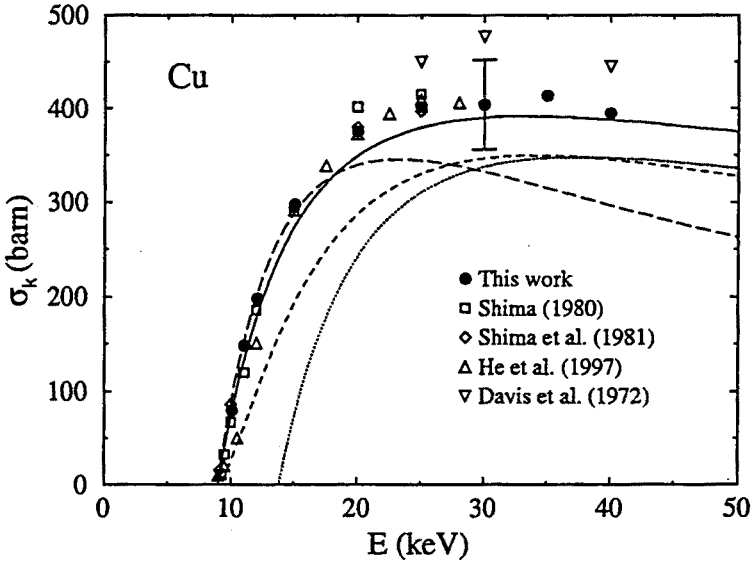

Figura 3. Secció eficaç d'ionització de la capa K pel coure. La línia continua és el model de Mayol and Salvat; la l'inia de punts és la fórmula de Bethe-Powell; la línia discontinua és la formula de Gryzinski; la l'inia discontinua llarga és la fórmula de Worthington–Tomlin. Els cercles negres són les mesures fetes en aquest treball. La resta de simbols correspon a altres mesures de diversos autors.

La distribució d'ionitzacions que genera el feix incident, en funció de la profunditat, es coneix habitualment com la funció $\Phi(\rho z)$, on ρ es la densitat i z és la profunditat. Aquesta funció és necessària per a poder convertir la intensitat de raigs x a concentració. Com ja s'ha esmentat anteriorment la simulació de la distribució d'ionitzacions requereix el coneixement de la secció eficaç total d'ionització; llavors, es calcula el nombre d'ionitzacions promig que es generen al llarg del segment de trajectòria. S'han simulat distribucions d'ionitzacions per a diversos materials, element traçadors i energies, per a mostres homogènies. Es comparen els resultats de simulació amb dades experimentals tretes de la literatura. També es comparen resultats pel que fa només a l'ionització superficial, de la qual, hom disposa de més dades experimentals. En un primer estudi, s'han simulat funcions $\Phi(\rho z)$ utilitzant diferents models per la secció

eficaç d'ionització. Per a les mostres simulades, els resultats confirmen que el model de Mayol i Salvat (1990) proporciona els millors resultats. En general, l'acord entre la simulació i les mesures experimentals es satisfactori (Fig. 4), tot i que hi ha casos en que les diferències són importants. Aquestes diferències podrien ésser degudes a errors experimentals, com ja han apuntat alguns autors, degut bàsicament a l'utilització de traçadors massa gruixuts i amb un nombre atòmic promig molt diferent de la matriu, i també degut al efecte de la fluorescència secúndaria, és a dir, reforçament de raigs x produïts per la pròpia absorció d'altres raigs x generats en la mateixa mostra.

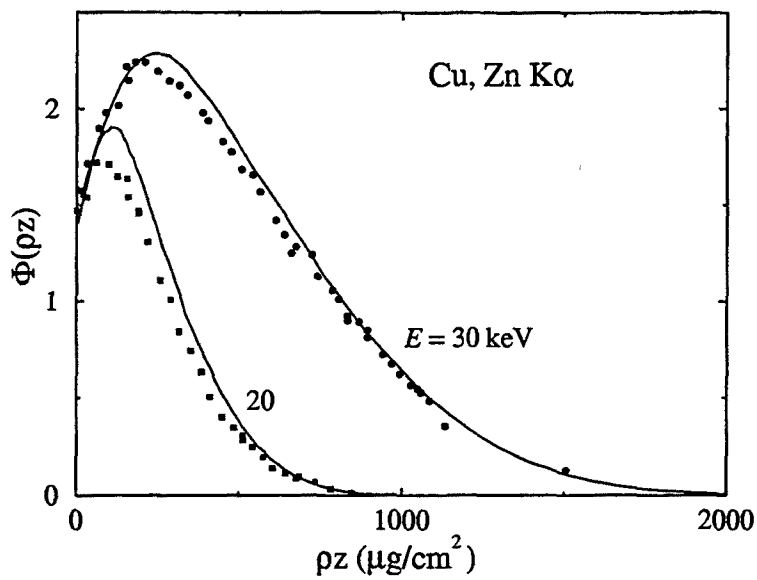

Figura 4. Distribució d'ionitzacions en profunditat per Cu amb un traçador de Zn Kα. Les línees són resultats de la simulació. Els punts corresponen a resultats experimentals trets de la literatura.

Ens interessa, però, estudiar la distribució d'ionitzacions en mostres no homogénies com ara capes primes dipositades en substrats o multicapes. Malauradament, no hi ha dades experimentals que proporcionin directament aquesta informació. Només es troben mesures de l'intensitat total de raigs x que genera el film o el substrat. Aquesta mesura, però correspon a l'integral, atenuada, de la $\Phi(\rho z)$, per la qual cosa és una mesura indirecta en la qual també intervenen els coeficients d'absorció màssics. S'han realitzat simulacions de l'intensitat total de raigs x en films i substrats; en general els resultats mostren un bon acord amb les mesures experimentals, si bé no són concloents.

S'ha iniciat la mesura sistemàtica de $\Phi(\rho z)$ per a films prims dipositats en substrats, començant per estudiar el seu valor a la superfície, és a dir, el paràmetre $\Phi(0)$. Això ens permet estudiar amb més flexibilitat la influència del substrat i el gruix del film. $\Phi(0)$ és un paràmetre interessant perqué, per una banda apareix en qualsevol intent de parametritzar analíticament la distribució $\Phi(\rho z)$, i per altra banda, és un excel.lent test de l'acuracitat de la simulació, com el coeficient de retrodifusió, però incloent l'emissió

de raigs x. S'ha mesurat experimentalment el valor de $\Phi(0)$ per Ni Kα, en làmines de Cu, de diversos gruixos, dipositats en diferents substrats, amb nombre atòmics que cobreixen tota la taula periòdica. Els gruixos de les diferents capes s'han mesurat, amb la tècnica convencional de la k-ratio en aquelles mostres on el nombre atòmic promig de la capa i substrat són similars, utilitzant novament el programa de Merlet (1995). Al mateix temps, el gruix dels films s'ha determinat pesant la quantitat de material dipositat, utilitzant una balança de precisió. L'acord d'ambdos mètodes es satisfactori. La particular elecció de l'element traçador (Ni) i el film (Cu), ha estat motivat per la necesitat de minimitzar els errors experimentals. Els elements Ni i Cu ténen nombres atòmics propers, per tant, ténen similar comportament a l'hora de dispersar i frenar els electrons, i a més, el film de Cu redueix la fluorescència secundària de raigs x originada pel substrat. Les principals dificultats de la mesura han estat la preparació de la mostra i la pròpia mesura de l'intensitat del pic de Ni Kα, ja que la relació pic-fons es molt petita. Aquestes dificultats fan que l'incertesa de les mesures no puguin baixar del 5%. Al mateix temps, s'ha simulat el valor de $\Phi(0)$, utilitzant el model de secció eficaç de Mayol i Salvat (1990). La comparació entre els resultats de simulació i l'experiment mostra un acord satisfatori dins d'un 5%. Els resultats mostren que, en general, la ionització de la superfície incrementa a mesura que incrementa el nombre atòmic del substrat (Fig. 5). En efecte, quan més pesat és el substrat més electrons es dispersen cap enrera i arriben al film amb suficient energia per poder ionitzar. De la mateixa manera, el valor de $\Phi(0)$ disminueix quan el gruix del film augmenta i/o quan l'energia del feix d'electrons decreix, és a dir, quan el nombre d'electrons que penetren el substrat amb suficient energia per retornar a la superfície disminueix.

Les simulacions fetes ens han permès derivar una expressió analítica, de clar interest pràctic, per descriure la $\Phi(0)$ a partir dels valors de $\Phi(0)$ del material de la capa i el substrat, en mostres gruixudes. En l'expressió analítica el gruix del film es normalitza per l'abast efectiu d'ionització, és a dir, el camí recorregut en promig dels electrons amb energia energia suficient per ionitzar. D'aquesta manera, s'evita la dependència amb l'energia incident, que queda englobada en aquest gruix normalitzat. L'abast d'ionització es pot calcular fàcilment integrat el poder de frenat o bé utilitzant alguna expressió analítica senzilla. L'expressió analítica derivada per a la $\Phi(0)$ ens permet reproduïr acuradament els resultats de simulació i és una bona base per obtenir expressions més generals, per altres materials i condicions experimentals. Alhora, la relació trobada per a $\Phi(0)$ pot ésser generalitzada per a altres paràmetres utilitzats en les fórmules analítiques de $\Phi(\rho z)$.

S'ha utilitzat la simulació per estudiar la distribució $\Phi(\rho z)$ en capes primes dipositades sobre substrats i multicapes. Ens interessa estudiar les diferències en la funció $\Phi(\rho z)$ entre un material gruixut i el mateix material en forma de capa prima dipositada sobre un substrat d'un altre material o bé en forma de substrat sobre el qual s'ha

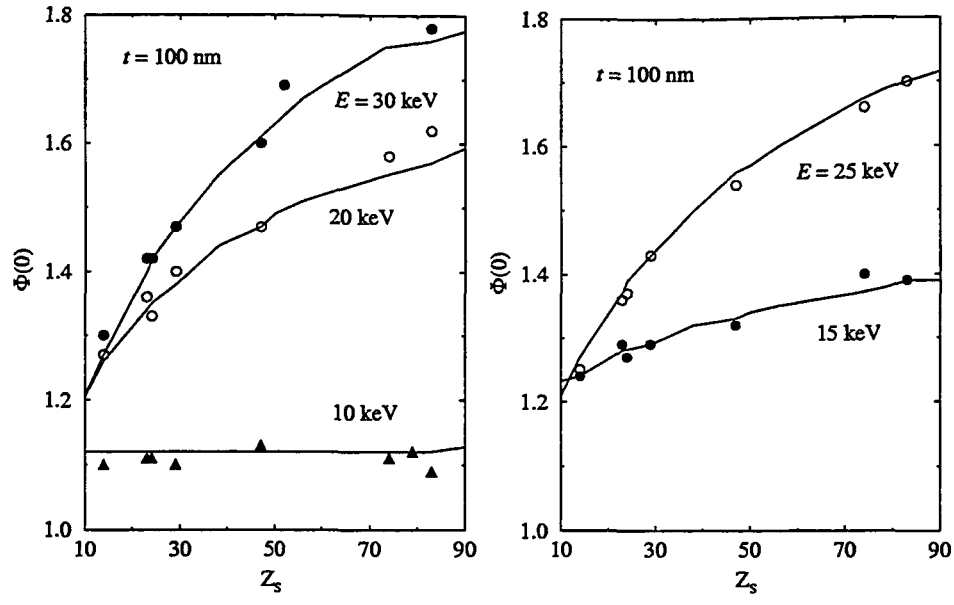

Figura. 5 Ionització superficial (Ni Kα) per a una capa de Cu de 100 nm de gruix en funció del número atòmic del substrat sobre el qual està dipositada. Les linees son els resultats de la simulació. Els punts són les mesures experimentals fetes en aquest treball.

dipositat una capa prima. Els resultats ens mostren que hi ha una clara influència del substrat en la distribució d'ionitzacions del film, sobretot quan la diferència dels seus nombres atòmics és important. Aquestes diferències són més importants en la interfície, on la influència del substrat és més gran i fan que la forma funcional de la funció $\Phi(\rho z)$ pel film sigui significativament diferent a la del mateix material gruixut. Respecte als substrats, es veu que les modificacions a la funció $\Phi(\rho z)$ ocasionada per la presència del film es poden descriure suposant que el film està formar pel mateix material que el substrat, però amb un gruix efectiu. Finalment, es mostren les distribucions d'ionitzacions per a multicapes, on s'observa la influència dels materials que envolten el film d'interès.

S'ha desenvolupat un programa per a la simulació de l'espectre complert de raigs x, que incorpora les seccions eficaces d'ionització i emissió de bremsstrahlung descrites i validades anteriorment. La inclusió de la nova secció eficaç d'emissió de bremsstrahlung ha suposat la modificació de PENELOPE. El programa simula tant el transport d'electrons com el transport dels raigs x, per tant es pot utilitzar fàcilment per analitzar qualsevol mostres composades de diferents fases, sempre i quan es puguin descriure geomètricament amb quàdriques. S'ha utilitzat sistemàticament el mètode de reducció de variança, anomenat interacció forçada, ja que els dos processos d'emissió de raigs x són molt poc probables, en comparació amb la resta de possibles interaccions.

Per validar el programa de simulació desenvolupat, s'han mesurat espectres de raigs x per a diversos materials i energies del feix d'electrons. Aquests espectres, s'han convertit

a unitats absolutes, és a dir, fotons per unitat d'angle sólid, energia i per electró incident. La conversió d'un espectre de raig x a unitats absolutes evita les incerteses originades per una possible normalització, i per tant proporciona una manera directe de validar globalment les diferents aproximacions fetes en la simulació, si be es poden produïr errors de tipus sistemàtic. Aquesta conversió requereix el coneixement del corrent incident, l'eficiència i l'angle sòlid de detecció i l'amplada del canal de l'espectre. A més, els espectres mesurats contenen els propis errors estadístics del procés de detecció de raigs x. En el nostre cas, aquests són de l'ordre del 3-6% per fotons de bremsstrahlung, i de l'ordre de 1-2% per a fotons dels pics característics. La contribució de totes les fonts d'error fa que l'incertesa global dels espectres mesurats siguin de l'ordre d'un ~5-7%. Els espectres s'han adquirit amb el detector de Si(Li), ja que aquest té una eficiència intrínsicament constant per a un ampli interval d'energia dels fotons emesos, ~3-15 keV. Fora d'aquest interval, l'eficiència decau fortament degut, per una banda, a l'absorció de radiació de baixa energia en les diferents finestres que hi ha a l'entrada del detector, i per altra banda, degut a que els fotons d'alta energia travessen tot el cristall sense interaccionar. Ja que es difícil avaluar la baixada de l'eficiència, els espectres mesurats només es poden comparar amb els simulats en l'interval on l'eficiciència es constant. Els espectres simulats s'han convolucionat per una funció Gaussiana, depenen de l'energia del fotó i prèviament determinada, per tal de tenir en compte la resposta del detector.

S'han simulat i mesurat diversos espectres de raigs x per a diferent tipus de mostres, homogenenies i multilaminars, per incidència normal oblícua amb feixos d'electrons de diferents energies. La comparació entre els espectres simulats i els mesurats és satisfactòria en l'interval on l'eficiència es constant, tal com mostra la Fig. 6. S'ha de dir que els espectres experimentals contenen alguns artefactes del propi procés de la detecció, els quals no s'han tingut en compte en la simulació, com ara, l'anomenada colecció incomplerta de càrrega, els pics suma i d'escapament i les regions d'apilament de fotons. Un dels avantatges del programa desenvolupat és que permet obtenir l'espectre per a mostres com ara partícules o inclusions en materials, que són de difícil tractament analític. Per altra banda, la simulació ens permet obtenir la contribució al pic característic de la fluorescència secundària, és a dir, a la fluorescència ocasionada per l'absorció d'altres raigs x generats en la pròpia mostra, efecte que és difícil d'aïllar experimentalment.

Finalment, s'utilitza la simulació per determinar l'eficiència d'un espectròmetre dispersiu en longitud d'ona, de gran interès en els métodes de microanàlisi que no utilizen patrons de referència. Aquesta s'ha obtingut dividint adeqüadament espectres mesurats amb espectres simulats, utilitzant els cristalls LiF and PET. Els resultats ens mostren clarament que l'eficiència depen fortament de l'energia, sobretot pel cristall PET, i és una funció creient de l'energia. S'han ajustat aquesta eficiència a una funció polinomica (Fig. 7).

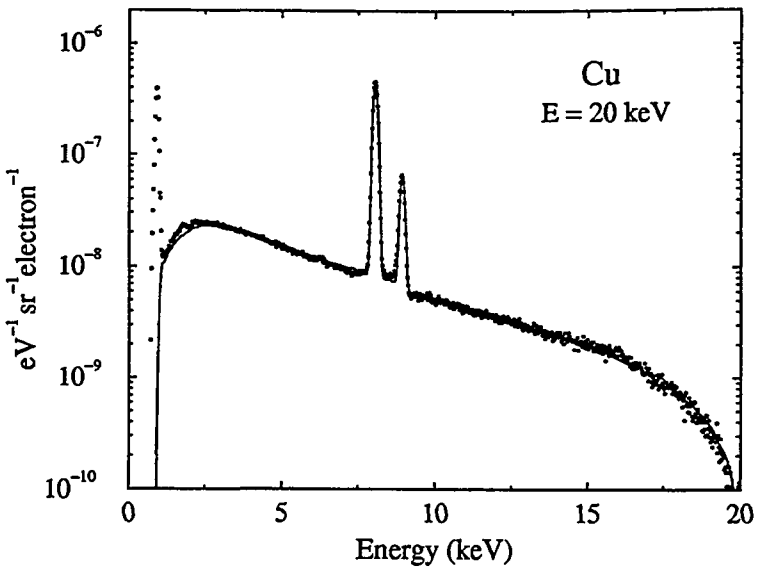

Figura 6. Comparació d'espectres de raigs x simulats (linia solida) amb les mesures fetes (punts), per una mostra de Cu.

Conclusions

S'ha desenvolupat un programa de simulació MC per a calcular espectres de raigs x i altres quantitats com ara la distribució d'ionizacions en funció de la profunditat. El programa es basa en el paquet de subrutines PENELOPE, que s'han modificat adeqüadament per extendre el seu rang de validesa a baixa energia. En particular, s'ha incorporat una nova secció eficaç doblement diferencial que combina la secció eficaç de Bethe-Heitler modificada per Salvat i Fernández-Varea, amb la distribució angular de Kirkpatrick-Wiedmann-Statham. La ionització de capes lligades es descriu mitjançant un model basat en informació óptica proposat per Mayol i Salvat. El mètode d'interacció forçat s'aplica sistemàticament per millorar l'eficiència de la simulació. El programa de simulació es aplicable a mostres amb geometria i composició arbitràries (multicapes, partícules, inclusions...)

S'ha proposat i aplicat un mètode sistemàtic per a la mesura de la secció eficaç d'ionització, utilitzant la microsonda d'electrons. S'han realitzat mesures de la secció eficaç d'ionització pel Ni, Cu i Cr, des del llindar d'ionització fins 40 keV. Els resultats ens proporcionen la dependència de la secció eficaç amb l'energia amb una precisió del ~3%. La transformació al valor absolut de la secció eficaç d'ionització incrementa l'incertesa a ~12%. La comparació entre experiment i diversos càlculs i fórmules empíriques de la literatura confirma que el model de Mayol i Salvat reprodueix millor la dependència amb l'energia de la secció eficaç d'ionització.

S'ha simulat la distribució d'ionitzacions i la ionització superficial per a diversos

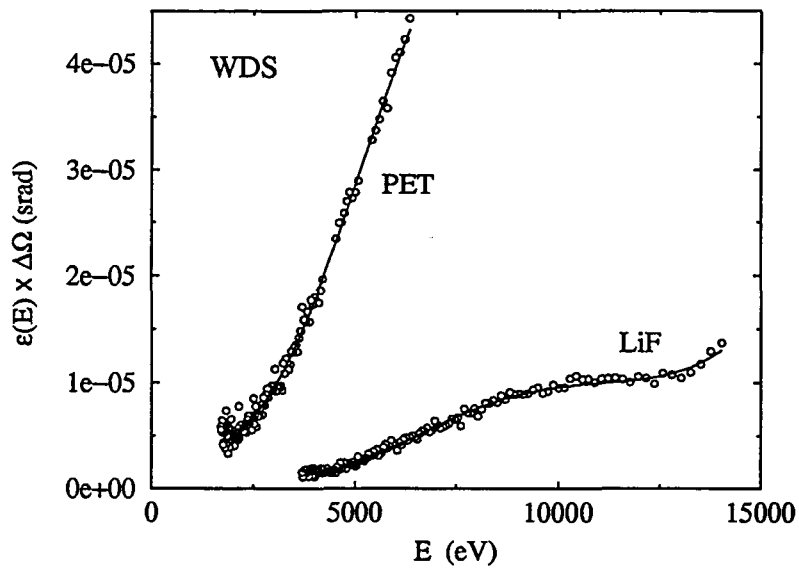

Figura 7. Eficiència absoluta d'un espectròmetre dispersiu en longitud d'ona, amb cristalls LiF i PET, determinada comparant espectres simulats i mesurats amb la microsonda.

materials homogénis, utilitzant el programa desenvolupat, i s'han comparat aquests resultats amb dades experimentals tretes de la literatura. L'acord entre simulació i experiment és satisfactori.

S'han realitzat mesures de la ionització superficial per a films de Cu de diferents gruixos, dipositats sobre diversos substrats amb nombres atòmics repartits per a tota la taula peridòdica. El traçador ha estat Ni Kα. Degut a les dificultats en preparar les mostres i les incerteses estadístiques associades a la mesura dels raigs x, els errors experimentals no han pogut ésser inferiors del 5%. Els resultats experimentals i la simulació mostren un acord satisfactori en un 5%. S'ha derivat una fórmula analítica que reprodueix els valors de $\Phi(0)$ mesurats i simulats. Es presenten distribucions d'ionització en funció de la profunditat per a mostres multilaminars.

La fiabilitat del programa de simulació desenvolupat s'ha valorat globalment comparant espectres de raigs x simulats i mesurats, en unitat absolutes. Les mesures s'han efectuat amb un detector Si(Li), en diferents tipus de mostres i condicions experimentals. Les diferents fonts d'error fan que els espectres experimentals tinguin una incertesa de l'ordre del 5-7%. L'acord entre simulació i experiment és raonable dins de l'interval d'energies on l'eficiència del detector és constants, és a dir, de ~3-15 keV. Fora d'aquest interval la comparació no té sentit, ja que es difícil estimar l'eficiència del detector. Utilitzant el programa desenvolupat, s'ha determinat l'eficiència d'un espectrómetre dispersiu en longitud d'ona, amb cristalls LiF i PET, des d'aproximadament ~2-15 keV. Aquesta informació és essencial pel microanàlisi sense utilització de patrons de

referència.

En resum, hem desenvolupat un programa de simulació Monte Carlo que permet la simulació acurada d'espectres de raigs x generats per feixos d'electrons, amb energies de l'ordre del keV, per mostres de qualsevol composició i geometries relativament complexes (capes primes dipositades en substrats, multicapes, particules, incidència no normal...). Al mateix temps, s'han efectuat mesures amb la microsonda d'electrons (secció eficaç d'ionització, ionització superficial, espectres de raigs x) que ens han permès validar experimentalment els resultats de la simulació i obtenir informació d'interès pràctic pel mètodes de microanàlisi.

Referències

H.A. Bethe and W. Heitler (1934), *Proc. R. Soc. London* **A146**, 83.

M. Gryzinski (1965), *Phys. Rev.* **138**, 336.

L. Kissel, C.A. Quarles, R.H. Pratt (1983), *At. Data Nucl. Data Tables* **28**, 381.

R. Mayol and F. Salvat (1990), *J. Phys. B: At. Mol. Opt. Phys.* **23**, 2117.

C.J. Powell (1976), *Rev. Mod. Phys.* **48**, 33.

F. Salvat and J.M. Fernández-Varea (1992), *Nucl. Instr. and Meth.* **B63**, 255.

F. Salvat, J.M. Fernández-Varea, J. Baró and J. Sempau (1996), Informes Técnicos Ciemat n. 799 (CIEMAT, Madrid).

P.J. Statham (1976), *X-Ray Spectrom.* **5**, 154 (1976).

C.R. Worthington and S.G. Tomlin (1965), *Proc. Phys. Soc.* (London) **A 69**, 401.

Contents

Preface

Electron beams are used in different spectroscopic techniques for materials analysis, such as electron probe microanalysis (EPMA), Auger electron spectroscopy (AES) and electron energy loss spectroscopy (EELS). Electrons penetrating matter suffer multiple interactions with the atoms of the target, and originate a cascade of secondary radiations. The radiation, electrons and photons, that escapes from the irradiated target has characteristic energy spectra, from which we can obtain quantitative information regarding the composition and structure of the sample. To take full advantage of these techniques, a quantitative understanding of the electron transport process and the generation of secondary radiations is required.

Electron beam instruments equipped with x-ray detectors are available in many laboratories. These instruments allow us to record the x-ray emission spectra induced by a focussed kV electron beam impinging on the sample. The name EPMA usually refers to any technique that uses the measured x-ray spectra, to obtain the "local" composition of the irradiated specimen. Developed by R. Castaing in 1952, EPMA is nowadays a well established analytical tool. The problem of quantitative analysis, i.e. the transformation of the measured signal into element concentrations, is solved by means of relatively simple, approximate semi-empirical algorithms. For bulk samples (i.e., homogeneous within the volume probed by the incident electron beam) available quantification algorithms yield fairly accurate results. However, for inhomogeneous samples (e.g. mutilayered specimens) the simplifications underlying these algorithms are not firmly established and there is a need for more realistic procedures.

Radiation transport problems can be conveniently studied by means of Monte Carlo (MC) simulation methods. The usefulness of MC simulation stems mainly from its ability to incorporate realistic physical interaction models and to describe situations with relatively complex geometries. Moreover, it is easy to keep track of the evolution of all secondary radiations generated by primary electrons. The only drawback of MC is that it requires very large computing times and, therefore, it is not suited for practical quantification, which frequently involves iteration procedures where the parameters of the interaction model and/or the geometry must be varied to fit the measured spectrum. Nevertheless, MC simulation is a valuable tool to check the reliability of practical approximate quantification methods and to guide the development of improved algorithms.

Obviously, the reliability of MC simulation results largely depends on the accuracy of the differential cross sections adopted to describe the interactions of electrons and photons with matter. As these cross sections are usually obtained from purely theoretical arguments, it is important to assess the adequacy of a MC code to the particular application of interest.

This thesis has two main objectives. First, to develop a general-purpose MC code for the simulation of electron-induced x-ray spectra from solids, covering the energy range of interest in EPMA. And, second, its validation by comparison of simulated x-ray spectra with measurements using the electron microprobe. After validating the code, it can be systematically used to generate information of practical interest in EPMA. The combination of simulation and measurements largely increases the potential of the technique. For instance, it makes it possible to determine the global efficiency of the x-ray detection system and to transform the measured spectrum into an absolute scale. Measurements on well-characterized samples can then be used to determine basic parameters, e.g. inner-shell ionization cross sections that, in turn, are of primary importance for quantification.

The thesis is structured in six chapters. In chapter 1, we briefly consider the physics of the interactions of kV electrons and photons with matter, and we describe differential cross sections for the various interaction mechanisms. Chapter 2 is devoted to the principles of Monte Carlo simulation, we also describe the structure of the PENELOPE code system, which is adopted as the basis of our simulations. The characteristics of the electron microprobe is the subject of chapter 3, where we describe the peculiarities of the CAMECA instrument used in the experiments reported in this work. Chapter 4 describes our measurements of K-shell ionization cross sections and we study the validity of various formulas of common use in quantification algorithms. Measurements and simulations of ionization distributions are presented in chapter 5; we study in detail the surface ionization, a parameter that is explicitly used in many quantification procedures. In chapter 6 we describe the simulation of the complete x-ray spectrum and we compare our simulation results with electron probe measurements.

Chapter 1

Electron and photon interactions

Knowledge of the interaction properties of low-energy ($\sim$ 0.1 to 100 keV) electrons and photons with solids is of primary importance in taking full advantage of many spectroscopic techniques such as Auger electron spectroscopy, (AES), x-ray photoelectron spectroscopy (XPS or ESCA), electron probe x-ray microanalysis (EPXMA or somewhat more ambiguously EPMA), electron energy loss spectroscopy, EELS, analytical electron microscopy (AEM), etc... Normally, each interaction mechanism is characterized by a corresponding atomic differential cross section (DCS), which is a function of the variables that are necessary to describe the individual interactions (i.e. scattering angles, energy transfer, initial energy and direction of generated secondary particles, if any). We should note that, strictly speaking, the concept of an atomic DCS is adequate only for very thin monoatomic gases, where each atom behaves as if it were isolated. In the case of solids, however, coherent scattering (i.e. interference between waves scattered by different atoms) may lead to measurable effects, which depend on the crystalline structure of the sample (e.g. charged particle channelling and near-edge and extended x-ray absorption fine structure). We shall limit our considerations to amorphous (or polycrystalline) samples, for which these coherent effects are relatively weak and can be disregarded. On the other hand, when inter-atomic distances are small (e.g. in molecules and in solids) there are strong interactions between neighbouring atoms that modify the structure of their outer shells and, hence, interaction properties may be somewhat different from those of isolated atoms.

The direct measurement of DCSs is a difficult experimental problem. Experiments with crossed electron and atomic beams, for example, provide reliable data about elastic and inelastic interactions with free atoms, but the information available is still fragmentary. In experimental studies of interactions with solids, targets are normally thin self-supporting films. This is the case for EELS, which provides valuable information on inelastic electron scattering. Measurements using thick samples have also been performed, but the results are hidden by multiple scattering within the target. Owing to

the difficulties of the experiments and to the scarcity of measured data, theoretical DCSs (in either analytical or numerical form) are normally used.

In principle, elaborate quantum mechanical computations may provide a realistic description of the various interaction DCSs. Indeed, the calculations of DCSs have reached a high degree of sophistication, with spectacular advances during the last three decades due to the advent of fast computers. In practice, however, these computations are too complicated for practical quantitative analysis and for Monte Carlo simulation; the common practice is to use DCSs obtained from relatively simple approximation methods. With the help of suitable approximations we achieve a better insight into the physics of the process and, in some cases, the resulting DCSs are given by analytical formulas. These formulas, although approximate, also provide a convenient basis to parameterize the numerical results obtained from more sophisticated calculations.

In this chapter, we shall briefly consider the physics of the various interaction processes and describe computational methods to obtain the corresponding atomic DCSs. We have selected those methods that either do not require extensive calculations or that are based on available numerical compilations and, at the same time, are reliable enough to meet the needs of quantitative EPMA. The approximations underlying the different theoretical models and their range of application will also be discussed. For the sake of simplicity, we shall consider that radiation penetrates an amorphous single-element medium of atomic number Z and density ρ with $\mathcal{N} = N_A\rho/A$ atoms per unit volume, where N_A is Avogadro's number and A is the atomic weight of the element. In the case of compounds, we shall assume that the molecular DCSs can be obtained by simply adding the atomic DCSs of all the atoms in a molecule (additivity rule); for many practical purposes, this is a fairly good approximation.

1.1 Electron interactions

The possible interactions of kV electrons (mass m, charge $-e$) with matter are elastic and inelastic collisions and bremsstrahlung emission. By definition, elastic interactions are those in which the initial and final quantum states of the target atom are the same, normally the ground state. These interactions change the direction of movement of the projectile and there is also a certain energy transfer from the projectile to the target, which causes the latter to recoil. Because of the large mass of the target ($\sim 1850Am$), the average energy lost by the projectile is a very small fraction of its initial energy (a few meV for elastic scattering of 30 keV electrons by Al atoms) and is usually neglected, which is equivalent to assuming that the target has an infinite mass and does not recoil.

Inelastic interactions are those in which the target is brought to an excited state, i.e. a part of the projectile's kinetic energy is taken up by the atomic electrons. These

include the excitation of single electrons in the conduction or valence bands, collective plasmon-like excitations and bound-shell ionization. Hard inelastic interactions (i.e. with relatively large energy transfers) normally cause the ionization of the target atom. In inelastic collisions, the projectile also changes its direction of motion, but to a lesser extent than in elastic collisions. Emission of bremsstrahlung takes place when the projectile is accelerated within the electrostatic field of the target atom; at the considered energies, this process occurs very seldomly and its stopping effect is much smaller than that of inelastic collisions.

1.1.1 Elastic scattering

Elastic interactions of electrons can be described as scattering of the projectile by the electrostatic field of the target (Mott and Massey, 1965). Assuming that the atomic electron density $\rho(r)$ is spherically symmetric, the interaction energy between the projectile at the position $\mathbf{r}$ and the target atom (placed at the origin of coordinates) is given by

$$V_{\rm st}(r) = -\frac{Ze^2}{r} + e^2\,4\pi\left[\frac{1}{r}\int_0^r \rho(r')r'^2\,{\rm d}r' + \int_r^\infty \rho(r')r'\,{\rm d}r'\right]. \qquad (1.1)$$

Accurate atomic electron densities can be calculated by using available Hartree-Fock codes (e.g. Desclaux, 1975). Analytical approximations to the field (1.1), usually as sums of several Yukawa-type terms, are also available from various authors (Cox and Bonham, 1967; Salvat et al., 1987).

As the incident electron is indistinguishable from those of the target, we must account for the occurrence of rearrangement collisions, in which the projectile exchanges places with an atomic electron. A formal treatment of exchange effects leads to a non-local potential (similar to that found in the Hartree-Fock method for bound states), which is difficult to handle. A convenient approach is to use the approximate local exchange potential of Furness and McCarthy (1973), which is given by

$$V_{\rm exch}(r) = \frac{1}{2}\left[E + V_{\rm st}(r)\right] - \frac{1}{2}\left\{\left[E + V_{\rm st}(r)\right]^2 + 4\pi a_0 e^4 \rho(r)\right\}^{1/2}, \qquad (1.2)$$

where E is the kinetic energy of the projectile and $a_0 = 0.529$ Å is the Bohr radius. Thus, the effective interaction potential is given by

$$V(r) = V_{\rm st}(r) + V_{\rm exch}(r). \qquad (1.3)$$

Within the static-field approximation (Mott and Massey, 1965; Walker, 1971), the DCS for elastic scattering is obtained by solving the partial-wave expanded Dirac equation for the motion of the projectile in the field (1.3). The result of elastic interactions reduces to a deflection of the projectile trajectory, characterized by the polar and azimuthal scattering angles θ and ϕ, respectively. For a central field (and spin-unpolarized

projectiles), the angular distribution of singly scattered electrons is axially symmetric about the direction of incidence, i.e. independent of ϕ. The DCS (per unit solid angle) for elastic scattering into the solid angle element $\mathrm{d}\Omega$ about the direction (θ, ϕ) is given by (Walker, 1971)

$$\frac{\mathrm{d}\sigma}{\mathrm{d}\Omega} = |f(\theta)|^2 + |g(\theta)|^2, \tag{1.4}$$

where

$$\begin{aligned} f(\theta) &= \frac{1}{2\mathrm{i}k} \sum_{\ell=0}^{\infty} \{(\ell+1)\,[\exp(2\mathrm{i}\delta_{\ell+}) - 1] + \ell\,[\exp(2\mathrm{i}\delta_{\ell-}) - 1]\}\, P_\ell(\cos\theta), \\ g(\theta) &= \frac{1}{2\mathrm{i}k} \sum_{\ell=0}^{\infty} \{\exp(2i\delta_{\ell-}) - \exp(2\mathrm{i}\delta_{\ell+})\}\, P_\ell^1(\cos\theta), \end{aligned} \tag{1.5}$$

are the direct and spin-flip scattering amplitudes, respectively.

$$k = \frac{1}{\hbar c}\left[E(E + 2mc^2)\right]^{1/2} \tag{1.6}$$

is the wave number of the projectile, $P_\ell(\cos\theta)$ are Legendre polynomials, $P_\ell^1(\cos\theta)$ are associated Legendre functions and $\delta_{\ell\pm}$ are the phase shifts. These are determined from the asymptotic behaviour of the Dirac radial functions for large r (Walker, 1971). Thus, to determine each phase shift we must solve the radial Dirac equations for the potential $V(r)$. Salvat and Mayol (1993) have written a computer program for the numerical evaluation of the DCS (1.4) for potentials given in numerical form, or as sums of Yukawa-type terms, which is available from the Computer Physics Communications Program Library. Computed DCSs for elastic scattering of electrons with various energies by aluminium and gold atoms are displayed in Fig. 1.1.

Absolute DCSs obtained from experiments with crossed electron and atom beams agree well with the results of static-field calculations for projectile energies above ~2 keV. For lower energies, the polarization of the target by the field of the projectile must be taken into account. To describe scattering in condensed matter (and in molecular gases), we should introduce the effect of aggregation, i.e. the alteration of the atomic electron density caused by nearby atoms. A plausible approach for solids is to describe the interaction by using a muffin-tin model potential (Salvat and Mayol, 1993), or the potential computed from a Hartree-Fock electron density satisfying Wigner-Seitz boundary conditions (see e.g. Kittel, 1976). It is found that the DCS obtained with these solid-state potentials differs from the free-atom DCS only at small scattering angles, which correspond to large impact parameters in a semi-classical image.

The total elastic cross section is given by

$$\sigma_{\mathrm{el}} = 2\pi \int_0^\pi \frac{\mathrm{d}\sigma_{\mathrm{el}}}{\mathrm{d}\Omega} \sin\theta\, \mathrm{d}\theta, \tag{1.7}$$

ant the mean free path between elastic collisions is

$$\lambda_{\mathrm{el}} = 1/\mathcal{N}\sigma_{\mathrm{el}}. \tag{1.8}$$

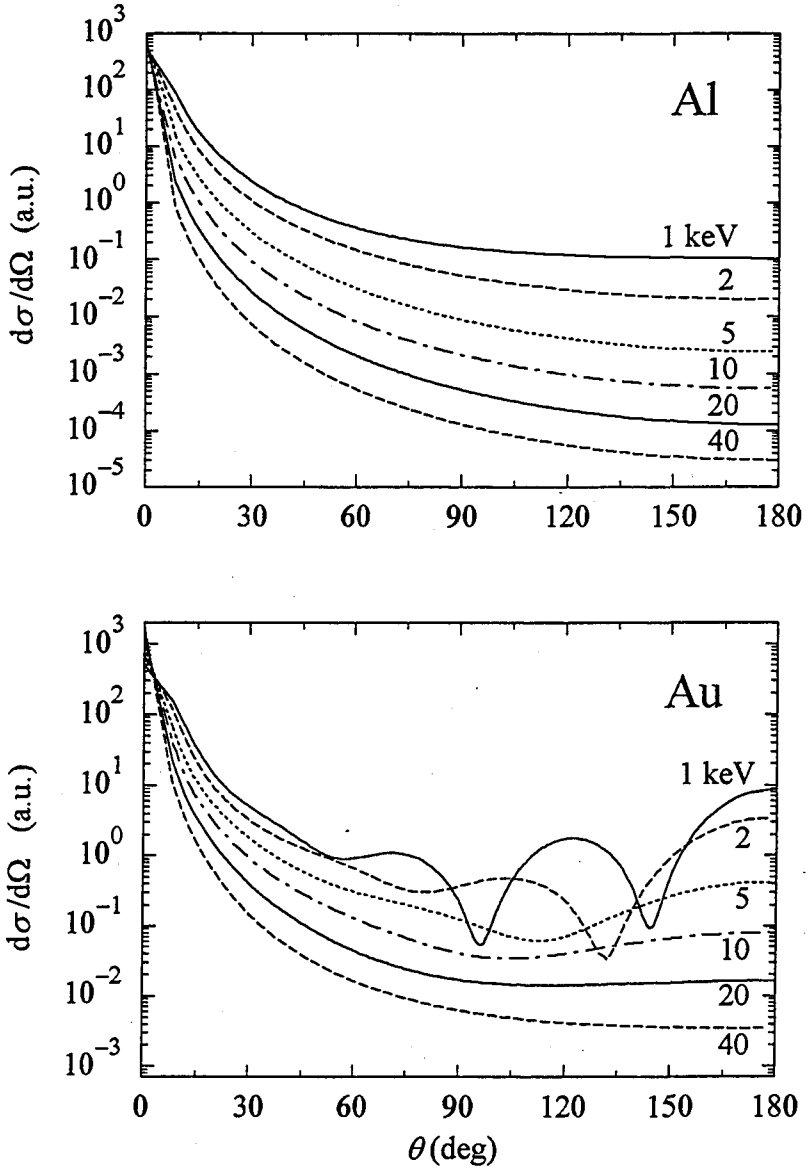

Figure 1.1. Elastic DCSs for electrons of the indicated energies scattered by aluminium and gold atoms.

Other parameters of interest are the first transport mean free path λ_1, which is defined by

$$\lambda_1^{-1} = \mathcal{N}2\pi \int_0^{\pi} (1 - \cos\theta) \frac{\mathrm{d}\sigma_{\mathrm{el}}}{\mathrm{d}\Omega} \sin\theta \mathrm{d}\theta = \frac{1 - \langle \cos\theta \rangle}{\lambda_{\mathrm{el}}}, \tag{1.9}$$

and the second transport mean free path λ_2,

$$\lambda_2^{-1} = \mathcal{N}2\pi \int_0^{\pi} \frac{3}{2}(1 - \cos^2\theta) \frac{\mathrm{d}\sigma_{\mathrm{el}}}{\mathrm{d}\Omega} \sin\theta \mathrm{d}\theta = \frac{3}{2} \frac{1 - \langle \cos^2\theta \rangle}{\lambda_{\mathrm{el}}}, \tag{1.10}$$

where $\langle \cdots \rangle$ indicates the average value in a single collision. The quantity $1 - \langle \cos\theta \rangle$ is a measure of the angular deflection in single elastic collisions. Therefore, the inverse of the first transport mean free path can be interpreted as the average angular deflection per unit path length. By analogy with the stopping power, which is defined as the mean energy loss per unit path length (see section 1.1.2), λ_1^{-1} is related to the "scattering power". Mean free paths and first transport mean free paths of electrons in aluminium and gold are plotted in Fig. 1.2 as functions of the electron energy.

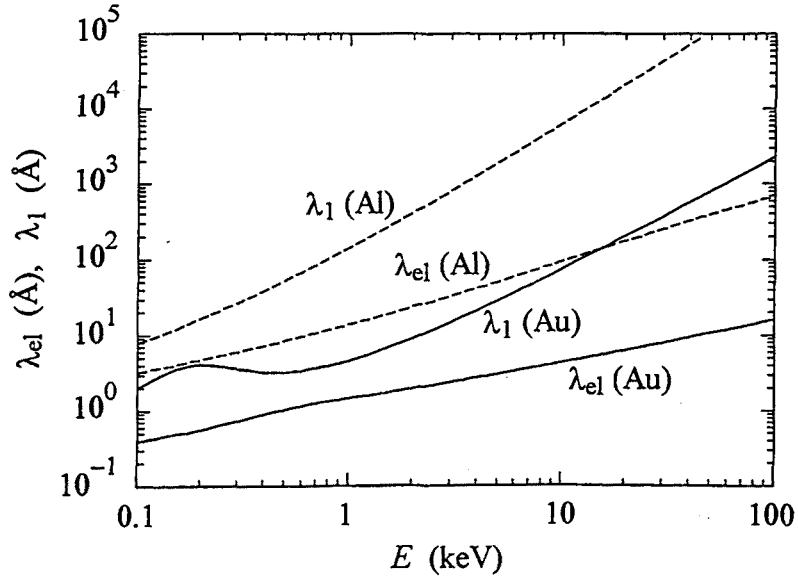

Figure 1.2. Elastic mean free paths and transport mean free paths of electrons in aluminium ($\rho = 2.7$ g/cm^3) and gold ($\rho = 19.3$ g/cm^3) as functions of the electron kinetic energy.

The Wentzel model

For practical calculations, it is useful to have a simple analytical formula for the elastic DCS. A convenient one is provided by the Wentzel (1927) model, in which the scattering field is approximated as an exponentially screened Coulomb field

$$V(r) = -\frac{Ze^2}{r} \exp(-\alpha r) \tag{1.11}$$

and the screening parameter α is given by

$$\alpha \simeq 2Z^{1/3}\ \text{Å}^{-1}, \tag{1.12}$$

which incorporates the $Z^{1/3}$ scaling predicted by the Thomas-Fermi atomic model. The corresponding DCS, obtained by means of the first Born approximation (see e.g. Bransden and Joachain, 1983), is

$$\frac{\mathrm{d}\sigma_{\mathrm{W}}}{\mathrm{d}\Omega} = \frac{Z^2e^4}{E}\frac{1}{(2\eta + 1 - \cos\theta)^2}, \tag{1.13}$$

where $\eta = (\alpha^2\hbar^2)/(4mE)$. In the literature, this formula is usually referred to as the screened Rutherford DCS.

The Wentzel model has been frequently used as the basis of simplified Monte Carlo simulations of kV electron transport. It predicts an angular distribution which is physically plausible (i.e. it has a nearly correct shape for intermediate energies), but the mean free path and the transport mean free path derived from this model differs markedly from the results of partial-wave calculations and experiments. It is worth recalling that the condition for the Born approximation to be valid is (Mott and Massey, 1965)

$$E \gg \frac{1}{2}Z^2\frac{me^4}{\hbar^2} = 13.6057Z^2\ \text{eV}. \tag{1.14}$$

Hence, the use of this approximation is only justified for relatively small atomic numbers and moderately high energies. The quantity on the right-hand side of the inequality is 85 keV for gold, 30 keV for Ag and 2.6 keV for aluminium. This means that for these and smaller energies, the Born approximation is not applicable.

1.1.2 Inelastic scattering

Individual inelastic interactions will be described by the scattering angle θ and the energy loss W of the projectile. Let $\mathbf{p}$ and E be the momentum and the kinetic energy of the incident electron just before the collision, the corresponding quantities after the collision are denoted by $\mathbf{p}'$ and $E' = E - W$, respectively. The momentum transfer in the collision is $\mathbf{q} \equiv \mathbf{p} - \mathbf{p}'$. It is customary to introduce the recoil energy Q defined by (Fano, 1963)

$$Q = \frac{q^2}{2m} = 2E - W - 2\sqrt{E(E-W)}\cos\theta, \tag{1.15}$$

which, in the particular case of collisions with a free electron at rest, coincides with the recoil energy of the target electron after the collision, i.e. $Q = W$ (for the time being we consider the projectile electron as distinguishable from those in the target). The maximum energy loss is W_{max}=E and, for a given W, the kinematically allowed recoil

energies are those in the interval $Q_- \leq Q \leq Q_+$ with end points given by (1.15) with $\cos\theta = \pm 1$:

$$Q_\pm = \left[E^{1/2} \pm (E - W)^{1/2}\right]^2. \tag{1.16}$$

The usual practice is to describe inelastic collisions by means of the non-relativistic first Born approximation (see e.g. Mott and Massey, 1965): the interaction between the projectile and the target system is treated by first-order perturbation theory and the initial and final states of the projectile are approximated as plane waves. The Born inelastic DCS can be expressed as

$$\frac{\mathrm{d}^2\sigma}{\mathrm{d}Q\mathrm{d}W} = \frac{\pi e^4}{E}\frac{1}{WQ}\frac{\mathrm{d}f(Q,W)}{\mathrm{d}W}, \tag{1.17}$$

where the quantity $\mathrm{d}f(Q,W)/\mathrm{d}W$ is the generalized oscillator strength (GOS), which completely characterizes the response of the target. It may be interpreted as the "effective number of atomic electrons" that participate in an inelastic interaction with given values of the energy and momentum transfer. The GOS satisfies the Bethe sum rule

$$\int_0^\infty \frac{\mathrm{d}f(Q,W)}{\mathrm{d}W}\,\mathrm{d}W = Z, \tag{1.18}$$

which backs up the interpretation.

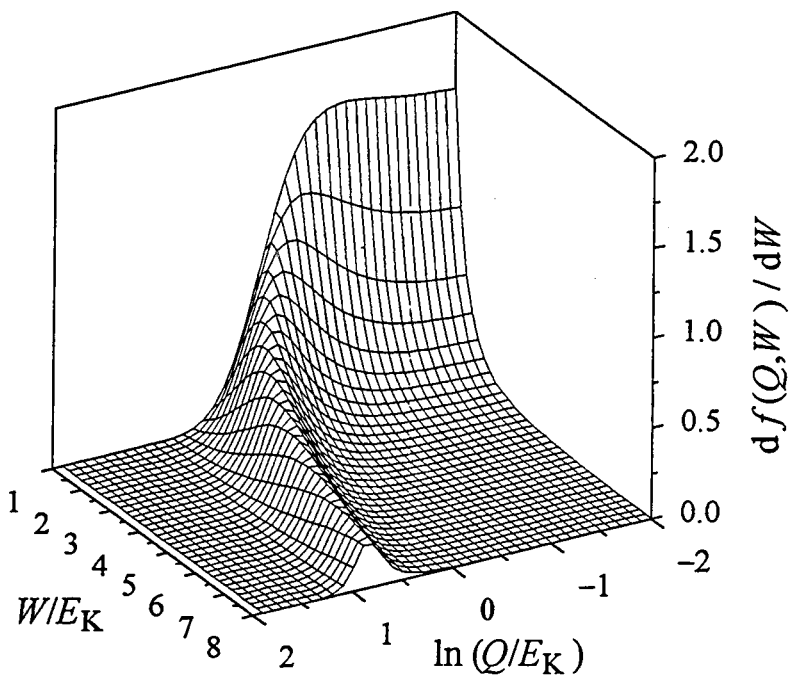

Figure 1.3. Bethe surface of the hydrogen atom. The vertical scale has been multiplied by 2 and the variables Q and W are expressed in units of the ionization energy E_K. This GOS is adequate to describe K-shell ionization of atoms.

The GOS is known analytically for only the simplest atomic target, namely the hydrogen atom (see Inokuti, 1971, and references therein). GOSs for other atoms and

ions have been computed numerically by a number of authors (McGuire, 1971; Manson, 1972) using independent electron models. The GOS can be represented as a surface over the plane (Q, W), which is known as the Bethe surface (Inokuti, 1971). The GOS of hydrogen, Fig. 1.3, illustrates the global features of the Bethe surface. In the high-W limit or, more specifically, for W much larger than the binding energies E_i of the electrons in the target, these behave as if they were free and at rest (i.e. collisions can be considered as binary electron-electron collisions). For binary collisions we have $Q = W$ and, therefore, the GOS vanishes except for $Q \simeq W$. Consequently, for $W \gg E_i$ the Bethe surface reduces to a ridge, the Bethe ridge, which peaks around the line $Q = W$. Accordingly,

$$\frac{\mathrm{d}f(Q,W)}{\mathrm{d}W} \simeq Z\delta(W-Q). \tag{1.19}$$

Actually, the Bethe ridge has a finite width which arises from the momentum distribution of the atomic electrons.

In the optical limit $Q = 0$, the GOS coincides with the optical oscillator strength (OOS),

$$\frac{\mathrm{d}f(Q,W)}{\mathrm{d}W} \simeq \frac{\mathrm{d}f(W)}{\mathrm{d}W}, \tag{1.20}$$

and the Bethe sum rule Eq. (1.18) reduces to the Thomas-Reiche-Kuhn sum rule (see e.g. Bransden and Joachain, 1983). The OOS is proportional to the (dipole) photoelectric cross section $\sigma_{\mathrm{ph}}(W)$ for photons of energy W (Fano and Cooper, 1968),

$$\frac{\mathrm{d}f(W)}{\mathrm{d}W} = \frac{mc}{2\pi^2 e^2 \hbar}\sigma_{\mathrm{ph}}(W). \tag{1.21}$$

Thus, within the Born approximation, the inelastic DCS for charged particles is intimately related to the photoabsorption cross section, which may be measured experimentally. In the limited range of Q values where relation (1.20) holds, the DCS given by (1.17) decreases rapidly with Q. It then follows that the OOS is the key quantity in determining the DCS for low-Q excitations, which correspond to moderately small energy losses and small angular deflections θ.

- For condensed media, it is convenient to consider the (complex) dielectric function $\epsilon(Q, W)$, which describes the response of an isotropic medium to a small electromagnetic disturbance. The dielectric function of the free-electron gas, derived from the Random Phase Approximation, has been given in analytical form by Lindhard (1954). The GOS and the dielectric function are related by (Inokuti, 1971; Fano, 1956)

$$\frac{\mathrm{d}f(Q,W)}{\mathrm{d}W} = \frac{2W}{\pi\Omega_{\mathrm{p}}^2} Z \cdot \mathrm{Im}\left[\frac{-1}{\epsilon(Q,W)}\right], \tag{1.22}$$

where

$$\Omega_{\mathrm{p}} = (4\pi\hbar^2 e^2 \mathcal{N} Z/m)^{1/2} \tag{1.23}$$

is the plasmon energy of an homogeneous electron gas with a density equal to the average electron density in the material. With the aid of relation (1.22), the GOS —which originally is an atomic concept— can also be applied to the solid state.

In practice, it is very difficult to evaluate the GOS of atoms in solids from first principles and we must rely on approximate GOS models. The so-called optical-data models combine empirical OOSs (obtained either from experimental optical data, EELS measurements or from available calculations) with suitable extension algorithms (normally based on the free-electron gas theory) to generate the GOS for $Q > 0$. For low-energy losses, the required optical information is available (only for selected materials) in the form of refractive index n and extinction coefficient κ (Palik, 1985). These are functions of the angular frequency ω of the field (which is related to the photon energy W through $W = \hbar\omega$) and are related to the energy-dependent dielectric function: $\epsilon(W) \equiv \epsilon(Q = 0, W) = (n + \mathrm{i}\kappa)^2$. The OOS can then be evaluated as

$$\frac{\mathrm{d}f(W)}{\mathrm{d}W} = \frac{2W}{\pi\Omega_\mathrm{p}^2} Z \cdot \mathrm{Im}\left[\frac{-1}{\epsilon(W)}\right] = \frac{2W}{\pi\Omega_\mathrm{p}^2} Z \cdot \mathrm{Im}\left[\frac{-1}{(n+\mathrm{i}\kappa)^2}\right]. \tag{1.24}$$

In the high-energy-loss range, the OOS can be obtained from (1.21) by using available photoelectric cross section data (see section 2.3). The most appealing feature of the optical-data models lies in the fact that the DCS for the most probable excitations (i.e. those involving low momentum transfers, which correspond to small scattering angles) is almost completely determined by the OOS. Hence, an optical-data model incorporating an accurately measured OOS should yield a fairly accurate description of these excitations.

It is worth recalling that, within the Born approximation, the DCS can be split into contributions from the various atomic shells (only single electron excitations are allowed in first-order perturbation theory), and each contribution can be interpreted as the DCS for binary collisions with bound electrons. In these interactions, the "atomic number" of the target is unity. Therefore, we may conclude that the Born approximation is generally adequate in describing inelastic collisions provided only binding effects are small, i.e. whenever W is much larger than the ionization energy of the active electron shell. Moreover, the largest contributions to the cross section arise from the most weakly bound shells and, therefore, the Born approximation turns out to be fairly accurate for all energies.

As the projectile is indistinguishable from the target electrons, exchange effects must be taken into account. These are conventionally introduced by means of the Ochkur (1965) approximation, which leads to the Born-Ochkur DCS,

$$\frac{\mathrm{d}^2\sigma}{\mathrm{d}Q\mathrm{d}W} = \frac{\pi e^4}{E}\frac{1}{WQ}\sum_i \left[1 - \frac{Q}{E + E_i - W} + \left(\frac{Q}{E + E_i - W}\right)^2\right]\frac{\mathrm{d}f_i(Q,W)}{\mathrm{d}W}, \tag{1.25}$$

where $\mathrm{d}f_i(Q,W)/\mathrm{d}W$ is the partial GOS of the active electron shell. The Born-Ochkur

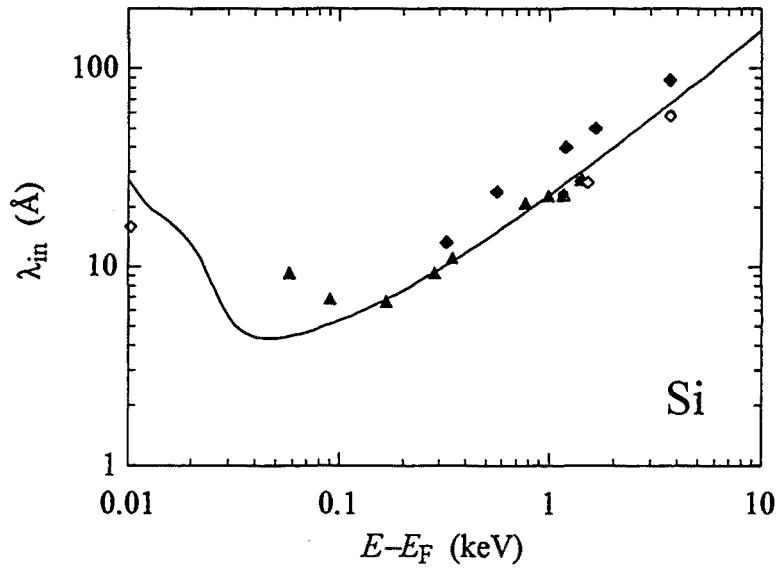

Figure 1.4. Inelastic mean free path of electrons in silicon ($\rho = 2.33$ g/cm^3). The abscissa is the electron energy above the Fermi level E_F. The continuous curve is the result of an optical data model (Fernández-Varea et al., 1993a). Symbols represent experimental data from various authors.

DCS for binary collisions with free electrons at rest ($Z = 1, E_i = 0$) is given by

$$\frac{\mathrm{d}^2\sigma}{\mathrm{d}Q\mathrm{d}W} = \frac{\pi e^4}{E}\frac{1}{WQ}\left[1 - \frac{Q}{E-W} + \left(\frac{Q}{E-W}\right)^2\right]\delta(Q-W), \tag{1.26}$$

which coincides with the exact non-relativistic (Born approximation) result known as the Møller DCS (Møller, 1932). In ionizing collisions, it is natural to consider that the faster electron after the collision is the "primary" one. Consequently, the maximum energy loss is $W_{\max} = E/2$ instead of E.

The inelastic total cross section σ_0 and the stopping cross section σ_1 are defined by

$$\sigma_n \equiv \int_0^{W_{\max}} W^n \,\mathrm{d}W \int_{Q_-}^{Q_+} \mathrm{d}Q \,\frac{\mathrm{d}^2\sigma}{\mathrm{d}Q\mathrm{d}W}. \tag{1.27}$$

The inelastic mean free path λ_{in} between inelastic collisions is

$$\lambda_{\mathrm{in}} = \frac{1}{\mathcal{N}\sigma_0}. \tag{1.28}$$

Fig. 1.4 illustrates the variation of λ_{in} with the electron energy in the case of silicon.

Another quantity of practical interest is the stopping power S, which is defined as the average energy loss per unit path length and is given by

$$S = \frac{\langle W \rangle}{\lambda_{\mathrm{in}}} = \mathcal{N}\sigma_1. \tag{1.29}$$

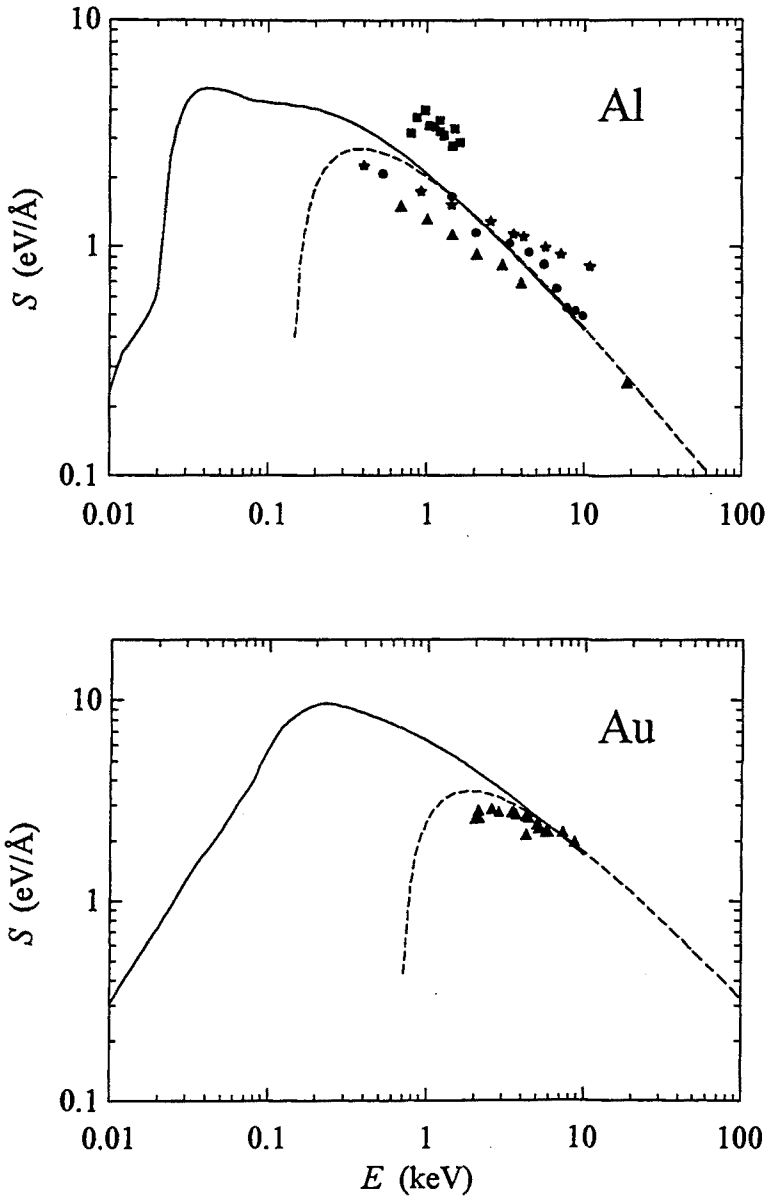

Figure 1.5. Stopping power of electrons in aluminium and gold. Solid curves are results from an optical-data model calculation; the dashed curves are calculated from the Bethe formula, Eq. (1.30). Symbols represent experimental data from different authors.

For projectiles with energy larger than the ionization energy of the most tightly bound shell, the stopping power is given by the Bethe formula

$$S(E) = \mathcal{N} Z \frac{2\pi e^4}{E} \ln\left(\sqrt{\frac{e}{2}}\frac{E}{I}\right), \tag{1.30}$$

where I is the mean excitation energy defined as

$$Z \ln I = \int_0^\infty \ln W \frac{\mathrm{d}f(Q=0,W)}{\mathrm{d}W} \mathrm{d}W. \tag{1.31}$$

Empirical values of I for single-element materials and some compounds are given, e.g. by Berger and Seltzer (1982). Fig. 1.5 displays the stopping power of electrons in aluminium

(I=166 eV) and in gold (I=790 eV) obtained from an optical-data model together with the prediction of the Bethe formula.

Continuous-slowing-down approximation

In many calculations, the average effect of inelastic collisions is taken into account by means of the continuous-slowing-down approximation (CSDA), which consists of assuming that electrons lose energy continuously; the energy loss along a short path length Δs is set equal to $S(E)\Delta s$. The stopping power $S(E)$ is usually obtained from the Bethe formula (1.30), empirically modified at low-electron energies (see e.g. Joy and Luo, 1989). However, it is worth recalling that the use of the CSDA may lead to erroneous results, since energy straggling (i.e. the fact that energy is lost in discrete collisions and in fluctuating amounts) is not accounted for. The CSDA can be used to describe global quantities, such as the backscattering coefficient, but it fails to reproduce, for example, the energy distribution of electrons backscattered or transmitted through thin foils.

1.1.3 Inner-shell ionization

In spite of the fact that inner-shell ionization is a relatively rare process, knowledge of the corresponding total (integrated) cross section is necessary to evaluate the generation of characteristic x-rays and Auger electrons. Quantum-mechanical calculations of inner-shell ionization cross sections have been reported by several authors (see the review by Powell, 1985). In most cases, the calculations do not lead to simple analytical formulae and must be evaluated numerically. For this reason, a variety of empirical and semi-empirical formulas have been proposed to approximate calculated and measured inner-shell ionization cross sections. These parameterizations however have limited ranges of validity and, furthermore, different formulae may lead to fairly different results. For the sake of simplicity, we shall limit ourselves to considering ionizations in the K-shell, for which the fluorescence yield is relatively well known (Sevier, 1972).

Using the topological properties of the GOS and the proper kinematical limits, Bethe (1932) expressed the integrated ionization cross section σ_K, Eq. (1.27), as

$$\sigma_K^2 E_K^2 = \frac{\pi e^4 \, Z_K \, b_K}{U_K} \ln(c_K U_K), \tag{1.32}$$

where E_K denotes the ionization energy of the K-shell, $U_K \equiv E/E_K$ is the over-voltage and Z_K is the number of electrons in the shell (=2, except for hydrogen) and b_K and c_K are parameters specific for the considered element. From values of b_K and c_K calculated theoretically, and derived from fits to experimental data, Powell (1985) recommends taking $b_K = 0.9$ and $c_K = 0.65$ for all elements. The resulting formula is approximately

valid in the energy range $4 \leq U_K \leq 25$. Notice that expression (1.32) is derived from the first Born approximation, with the additional assumption that U_K is sufficiently large. Therefore, it does not reproduce the actual dependence of σ_K on E near the ionization threshold. Unfortunately, this is often the working regime in EPMA.

Worthington and Tomlin (1956) introduced an empirical modification to extend the validity of the asymptotic Bethe formula to energies closer to the ionization threshold. Their formula reads

$$\sigma_K^2 E_K^2 = \pi e^4 \, Z_K \, a_K \frac{\ln(U_K)}{U_K} \ln\left[\frac{4U_K}{1.65 + 2.35\exp(1 - U_K)}\right], \tag{1.33}$$

with $a_K = 0.35$.

On the other hand, a number of classical and semiclassical formulations to obtain analytical expressions for the ionization cross section have also been proposed. Thus, Gryzinski (1965) obtained the following widely used formula

$$\sigma_K^2 E_K^2 = \pi e^4 \, Z_K \, g(U_K), \tag{1.34}$$

where

$$g(U_K) = \frac{1}{U_K}\left[\frac{U_K - 1}{U_K + 1}\right]^{3/2}\left[1 + \frac{2}{3}\left(1 - \frac{1}{2U_K}\right)\ln[2.7 + (U_K - 1)^{1/2}]\right]. \tag{1.35}$$

It should be noted however that this formula is derived from purely classical arguments and, therefore, its validity is open to question.

Ionization cross sections can be obtained by means of an optical-data model (Mayol and Salvat, 1990) in which the OOS is set equal to the photoelectric cross section and extended to $Q > 0$ by using a simple algorithm (the delta-oscillator) proposed by Liljequist (1983). The physical basis of this optical-data model is equivalent to that of the Weizsäcker-Williams method of virtual quanta (see Jackson, 1975) as used e.g. by Kolbenstvedt (1967). With exchange effects accounted for by means of the Ochkur approximation, the resulting DCS reads

$$\begin{aligned}\frac{\mathrm{d}^2\sigma_{\mathrm{ion}}}{\mathrm{d}Q\mathrm{d}W} &= \frac{\pi e^4}{E}\frac{1}{WQ}\frac{mc}{2\pi^2 e^2\hbar^2}\int \sigma_{\mathrm{ph}}(W')\left[1 - \frac{Q}{E + W' - W} + \left(\frac{Q}{E + W' - W}\right)^2\right] \\ &\quad \times \left[\delta(W - W')\Theta(W' - Q) + \delta(W - Q)\Theta(Q - W')\right]\mathrm{d}W',\end{aligned} \tag{1.36}$$

where $\sigma_{\mathrm{ph}}(W')$ is the photoelectric cross section for ionization of the considered shell by photons of energy W' (which is proportional to the optical oscillator strength). $\delta(x)$ represents the Dirac δ-distribution and $\Theta(x)$ (= 1 if $x > 0$, = 0 otherwise) is the Heaviside step function. The total ionization cross section is

$$\sigma_K(E) = \int_{E_K}^{E/2} \mathrm{d}W \int_{Q_-}^{Q_+} \frac{\mathrm{d}^2\sigma}{\mathrm{d}Q\mathrm{d}W}\,\mathrm{d}Q. \tag{1.37}$$

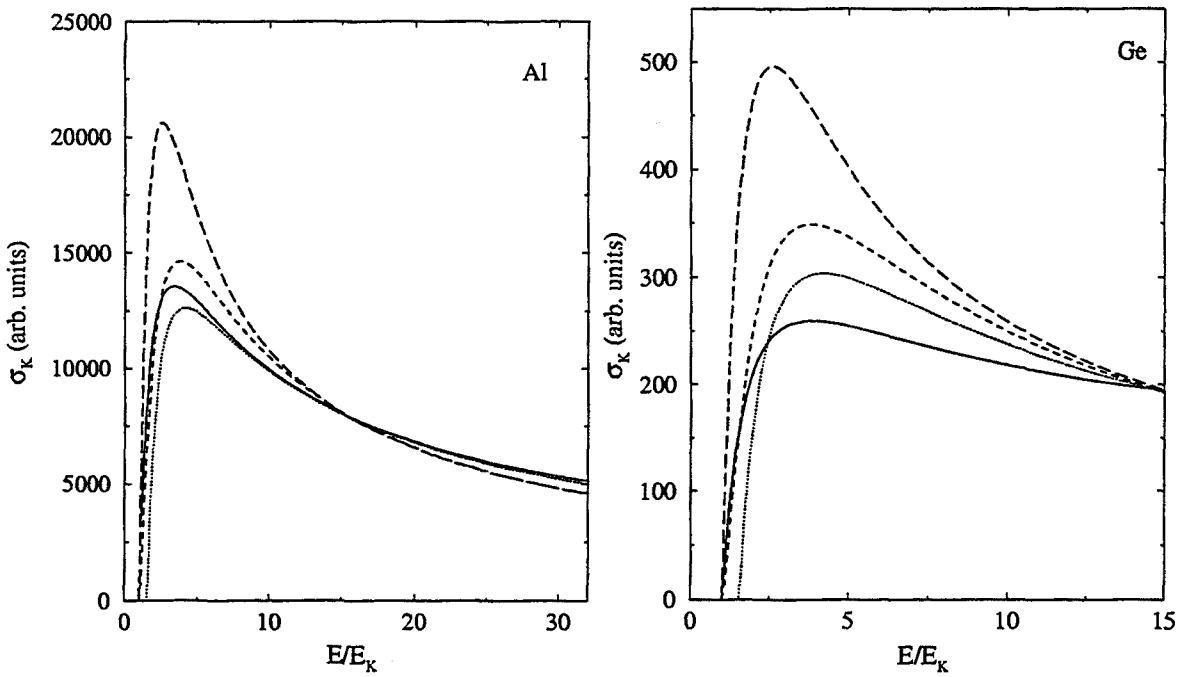

Figure 1.6. *Comparison of ionization cross sections and experimental values for Al (a) and Ge (b). Different curves are the results of the Bethe-Powell formula (1.32), dotted; the Gryzinski formula (1.34), dashed, and the Worthington-Tomlin formula (1.33), long-dashed; the optical-data model of Mayol and Salvat (1.37), continuous.*

To improve the cross section near the ionization threshold, a Coulomb-like correction is also incorporated. For ionization of K-shells, the OOS of hydrogen, suitably re-scaled, provides a simple and sufficiently accurate analytical approximation for $\sigma_{\rm ph}$; the integrand in Eq. (1.37) can then be expressed analytically and the integrals evaluated with the aid of simple numerical quadrature routines.

Fig. 1.6 displays K-shell ionization cross-sections of aluminium and germanium calculated from formulas (1.32-37). For future reference, the different curves have been re-scaled to coincide for $U_{\rm K} = 15$. For higher energies, the Born approximation should be accurate (and hence the Bethe-Powell and optical-data results should nearly coincide).

1.1.4 Bremsstrahlung emission

Bremsstrahlung photons are produced with a continuous energy spectrum that extends from zero to the energy of the projectile. Although the process has a negligible stopping effect for kV electrons, it is the source of the continuous background in x-ray spectra. The bremsstrahlung DCS depends on the energy W and direction of the emitted photon and on the final direction of the outgoing electron. We shall assume that the deflection of the incoming electron is accounted for by elastic scattering, thus the direction of the

projectile is not modified by the emission of bremsstrahlung photons. This assumption is plausible for soft bremsstrahlung emission; it is also well justified for hard radiative events since these occur with extremely small probability. In contrast to the emission of characteristic x-rays, bremsstrahlung emission is anisotropic.

Bremsstrahlung DCSs, differential in the energy W and direction $\Omega = (\theta, \phi)$ of the emitted photon, for electrons with energies E between 1 keV and 500 keV have been obtained by Kissel et al. (1983) from partial-wave calculations. Their results are the most accurate data available for the energy range of interest here, but they consist of extense tables, which are difficult to handle. Actually, Kissel et al. (1983) computed the DCS only for six elements at selected energies and obtained those of the other elements by interpolation and extrapolation. As the amount of numerical data for these six elements is relatively modest (a few hundred kbytes), one can reduce the database to these elements and generate the required DCSs, for any element and any electron energy, by cubic spline interpolation. Unfortunately, there is no simple analytical expression that reproduces the trends of Kissel et al.'s tabulation.

A common practice in x-ray microanalysis is to use a parameterization of the DCS obtained from Sommerfeld's theory (Sommerfeld, 1931) due to Kirkpatrick and Wiedmann (1945) and Statham (1976), hereafter referred to as the KWS formula. However, it will be shown that this parameterization differs very significantly from the more accurate partial-wave calculation results of Kissel et al. (1983).

The Kirkpatrick–Wiedmann–Statham (KWS) double-differential cross section (DDCS) is given by the following general expression

$$\frac{\mathrm{d}^2\sigma_{\mathrm{KWS}}}{\mathrm{d}W\mathrm{d}\Omega} = \frac{\sigma_x(1-\cos^2\theta)+\sigma_y(1+\cos^2\theta)}{(1-\beta\cos\theta)^2}, \tag{1.38}$$

where σ_x and σ_y are parameters that depend on the electron incident energy E, the emitted photon energy W and the atomic number Z of the target. Kirkpatrick and Wiedmann (1945) obtained analytical approximations for the x and y components of the atomic DCS in terms of the dimensionless quantities

$$Q \equiv \frac{W}{E} \quad \text{and} \quad U \equiv \frac{E}{0.2998 Z^2\,\mathrm{keV}}. \tag{1.39}$$

Their expressions are

$$\sigma_x = \frac{0.252 + a(Q-0.135) - b(Q-0.135)^2}{UW} \times 10^{-50}\ \mathrm{cm}^2/(\mathrm{sr\ keV}) \tag{1.40}$$

and

$$\sigma_y = \frac{-g + h/(Q+f)}{UW} \times 10^{-50}\ \mathrm{cm}^2/(\mathrm{sr\ keV}), \tag{1.41}$$

with the definitions

$$\begin{aligned} a &= 1.47B - 0.507A - 0.833, & f &= \frac{-0.214y_1 + 1.21y_2 - y_3}{1.43y_1 - 2.43y_2 + y_3}, \\ b &= 1.70B - 1.090A - 0.627, & g &= (1+2f)y_2 - 2(1+f)y_3, \\ & & h &= (1+f)(y_3+g), \end{aligned} \tag{1.42}$$

where

$$\begin{aligned} A &= \exp(-0.2230U) - \exp(-57.0U), & y_1 &= 0.22[1 - 0.39\exp(-26.9U)], \\ B &= \exp(-0.0828U) - \exp(-84.9U), & y_2 &= 0.067 + \frac{0.023}{U + 0.75}, \\ & & y_3 &= -0.00259 + \frac{0.00776}{U + 0.116}. \end{aligned} \tag{1.43}$$

Statham (1976) introduced a modification to produce a better fit to the theoretical data at small electron energies and proposed the following formulas for the energy range $U < 0.0604$,

$$\begin{aligned} \sigma_x &= \exp(a_x) \times 10^{-50}\ \mathrm{cm}^2/(\mathrm{sr\ keV}), \\ \sigma_y &= \exp(a_y) \times 10^{-50}\ \mathrm{cm}^2/(\mathrm{sr\ keV}), \end{aligned} \tag{1.44}$$

where

$$\begin{aligned} a_x &= (-1.019040 + 0.1460140\mathcal{Q} - 0.0501077\mathcal{Q}^2)\ln U \\ &\quad -1.483110 + 0.9474840\mathcal{Q} - 0.3500140\mathcal{Q}^2, \\ a_y &= (-0.882129 + 0.0366934\mathcal{Q} - 0.3396460\mathcal{Q}^2)\ln U \\ &\quad -1.040880 - 1.8635500\mathcal{Q} - 0.7230680\mathcal{Q}^2. \end{aligned} \tag{1.45}$$

These expressions are applicable for $\mathcal{Q} > 0.2$. For smaller $\mathcal{Q}$-values, Statham suggested a further modification that consists of multiplying σ_x and σ_y by the factors

$$f_x = 1 - 0.567\exp(-20\mathcal{Q}), \tag{1.46}$$

and

$$f_y = \begin{cases} 1 & \text{, if } U > 0.0604 \\ 1 - (-0.55 + 4.83U)\exp(-20\mathcal{Q}) & \text{, otherwise} \end{cases} \tag{1.47}$$

respectively.

The Bethe-Heitler (BH) DCS (Bethe and Heitler, 1934) provides a simple analytical formula for the energy distribution of the emitted photons, which is well suited for random sampling. It is based on the Born approximation and, therefore, is valid only for high-energy electrons. Salvat and Fernández-Varea (1992) introduced an empirical

correction term that extends its validity to lower energies. The modified energy-loss Bethe-Heitler DCS for an element of atomic number Z is given by

$$\frac{\mathrm{d}\sigma_{\mathrm{BH}}}{\mathrm{d}W} = C_{\mathrm{BH}} \left(\varphi_1(\varepsilon) + \frac{1}{\varepsilon}\varphi_2(\varepsilon)\right), \tag{1.48}$$

where ε is the reduced energy of the emitted photon,

$$\varepsilon \equiv \frac{W}{E + mc^2}, \tag{1.49}$$

and C_{BH} is a constant determined as explained below.

The quantities $\varphi_1(\varepsilon)$ and $\varphi_2(\varepsilon)$ are functions of ε given by

$$\varphi_1(\varepsilon) = f_1(b) + f_0(\varepsilon), \qquad \varphi_2(\varepsilon) = \frac{4}{3}(1-\varepsilon)[f_2(b) + f_0(\varepsilon)], \tag{1.50}$$

where

$$b \equiv \frac{Rmc}{\hbar}\frac{1}{2\gamma}\frac{\varepsilon}{1-\varepsilon}, \qquad \gamma = 1 + \frac{E}{mc^2} \tag{1.51}$$

and

$$\begin{aligned} f_0(\varepsilon) &= 4\ln(Rmc/\hbar) + F_2(Z,\gamma) \\ f_1(b) &= 2 - 2\ln(1+b^2) - 6b\tan^{-1}(b^{-1}), \\ f_2(b) &= \frac{7}{3} - 2\ln(1+b^2) - 6b\tan^{-1}(b^{-1}) \\ &\quad -b^2\left[4 - 4b\tan^{-1}(b^{-1}) - 3\ln(1+b^{-2})\right] \end{aligned} \tag{1.52}$$

The parameter R is the screening radius of the element, which is given by Salvat and Fernández-Varea (1992). The term $F_2(Z,\gamma)$ is the empirical low-energy correction introduced by these authors. From a numerical fit of the radiative cross sections given by Seltzer and Berger (1985) they obtained the following analytical approximation for this term

$$\begin{aligned} F_2(Z,\gamma) &= \left(4.650 - 6.005(\alpha Z) + 2.946(\alpha Z)^2\right)(\gamma-1)^{-1} \\ &\quad - \left(32.42 - 67.08(\alpha Z) - 3.906(\alpha Z)^2\right)\gamma^{-1} \\ &\quad + \left(20.33 + 23.38(\alpha Z) - 77.42(\alpha Z)^2\right)\gamma^{-2}. \end{aligned} \tag{1.53}$$

The "normalization" constant C_{BH} is determined in such a way that the modified DCS given by Eq. (1.48) exactly reproduces the radiative stopping powers for electrons in single-element materials given by Berger and Seltzer (1982), which were derived from the partial-wave calculations of Kissel et al. (1983). Thus the DCS (1.48) provides a fairly good approximation for the electron mean free path between radiative events and for the distribution of energy losses in those events. However, the angular distribution of the emitted photons must be obtained by other means.

The direction of the emitted photon, relative to that of the primary electron, is defined by the polar angle θ and the azimuthal angle ϕ. Considering that the atomic field is spherically symmetric, the angular distribution of the emitted photon is independent of ϕ; hence, the azimuthal scattering angle is distributed uniformly in the interval $(0,2\pi)$. The probability distribution of the polar angle can be obtained from the classical dipole approximation (see e.g. Jackson, 1975),

$$p_{\text{dipole}}(\cos\theta) = \frac{3}{16\pi}\left[1+\left(\frac{\cos\theta-\beta}{1-\beta\cos\theta}\right)^2\right]\frac{1-\beta^2}{(1-\beta\cos\theta)^2}, \tag{1.54}$$

where $\beta = v/c$ is the velocity of the electron in units of the speed of light c ($\beta^2 = 1-\gamma^{-2}$). This angular distribution is reasonably accurate for energies above ~ 1 MeV, but becomes incorrect at lower energies.

The DDCS can then be written as

$$\frac{\mathrm{d}^2\sigma_{\text{BHd}}}{\mathrm{d}W\mathrm{d}\Omega} = C_{BH}\left(\varphi_1(\varepsilon)+\frac{1}{\varepsilon}\varphi_2(\varepsilon)\right)\frac{1}{2\pi}p_{\text{dipole}}(\cos\theta). \tag{1.55}$$

Sempau et al. (1997) have shown that this DDCS gives a fairly accurate description of bremsstrahlung spectra generated by kV electrons in thick samples, in spite of the limitations of the intrinsic angular distribution (1.54). The reason for this is that, in the case of bulk targets, the electron trajectories are rapidly randomized by elastic scattering and the angular distribution of photons emerging through the surface is practically insensitive to the intrinsic angular distribution. However, for thin films and small particles the effect of the angular dependence of the cross section may be important and a more accurate intrinsic distribution should be used, as it has been shown by Acosta (1997).

Energy-loss bremsstrahlung DCSs obtained from the modified Bethe-Heitler formula (1.48) and from the KWS formula (1.38) integrated over angles are compared with Kissel et al.'s data in Fig. 1.7. Notice that, for low-energy electrons, the Bethe-Heitler formula gives an energy-loss DCS proportional to W^{-1}, in accordance with the numerical results. Moreover, owing to the definition of the normalization constant C_{BH} in Eq. (1.48), the areas below the modified BH curves and below Kissel et al.'s data are equal. We see that the KWS formula clearly overestimates the energy-loss DCS in the considered energy range, as pointed out by e.g. Chapman et al. (1983). Surprisingly, it predicts angular distributions in fairly good agreement with the calculations of Kissel et al.

1.1.5 New DCS for bremsstrahlung emission

In order to obtain a more accurate formula for the DDCS than the approximations given by eqs. (1.55) and (1.38), we shall tentatively combine the modified Bethe-Heitler DCS,

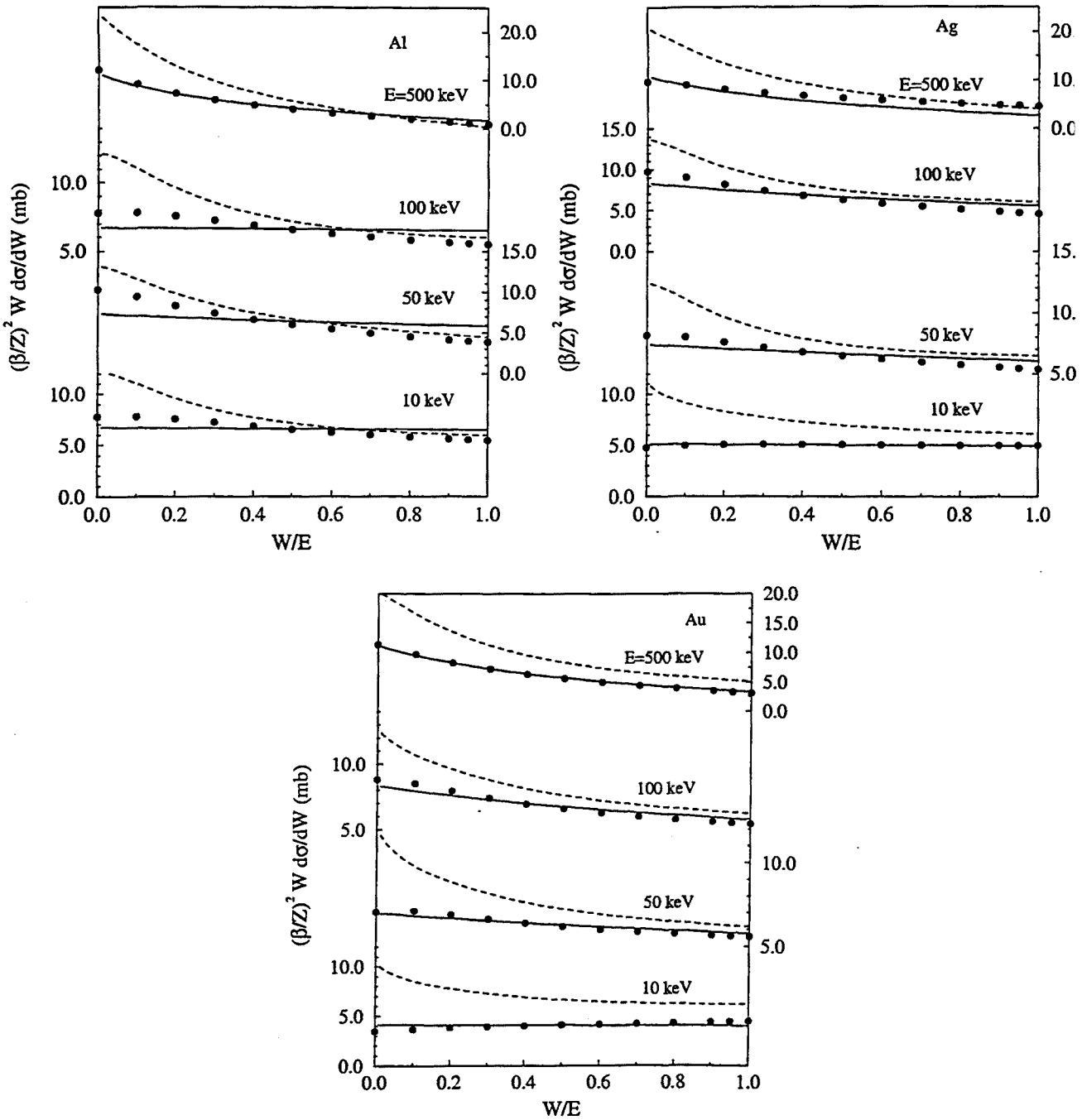

Figure 1.7. Reduced energy-loss DCSs, i.e. DDCSs integrated over angles and multiplied by $(\beta/Z)^2 W$, for bremsstrahlung emission by electrons in Al (a), Ag (b) and Au (c). Dashed curves, Kirkpatrick-Wiedmann-Statham formula (1.38); continuous lines, modified Bethe-Heitler formula (1.48). Dots represent tabulated results of Kissel et al.

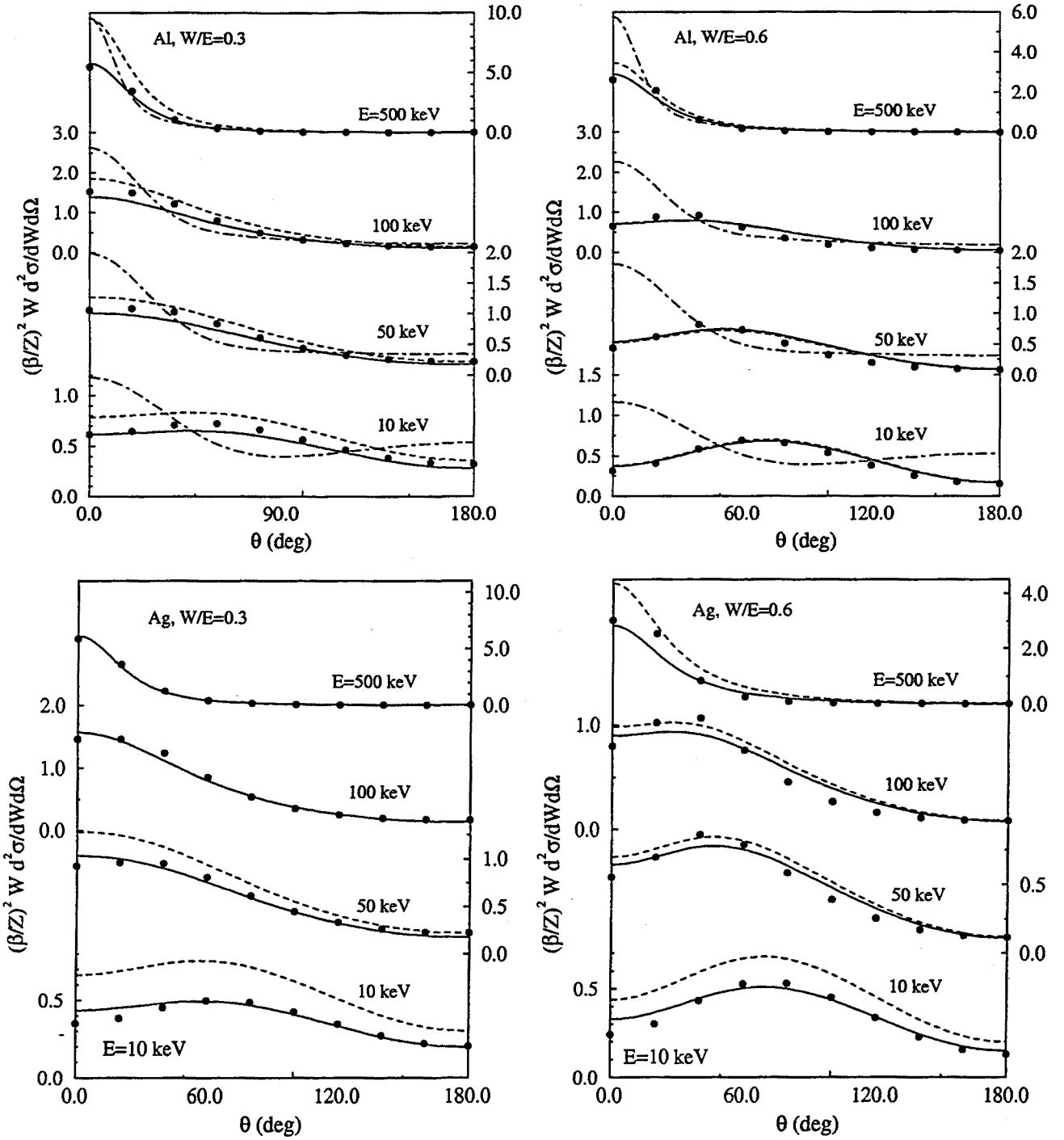

Figure 1.8a. Electron bremsstrahlung reduced DDCSs for Al and Ag and different photon-to-electron energy ratios W/E: $W/E = 0.3$, $W/E = 0.6$. Dot-dashed curves, modified Bethe-Heitler DCS model with dipole angular distribution (1.55); dashed curves, Kirkpatrick-Wiedmann-Statham DDCS (1.38); solid curves, modified Bethe-Heitler DCS with KWS angular distribution (1.59). Dots represent numerical data calculated by Kissel et al.

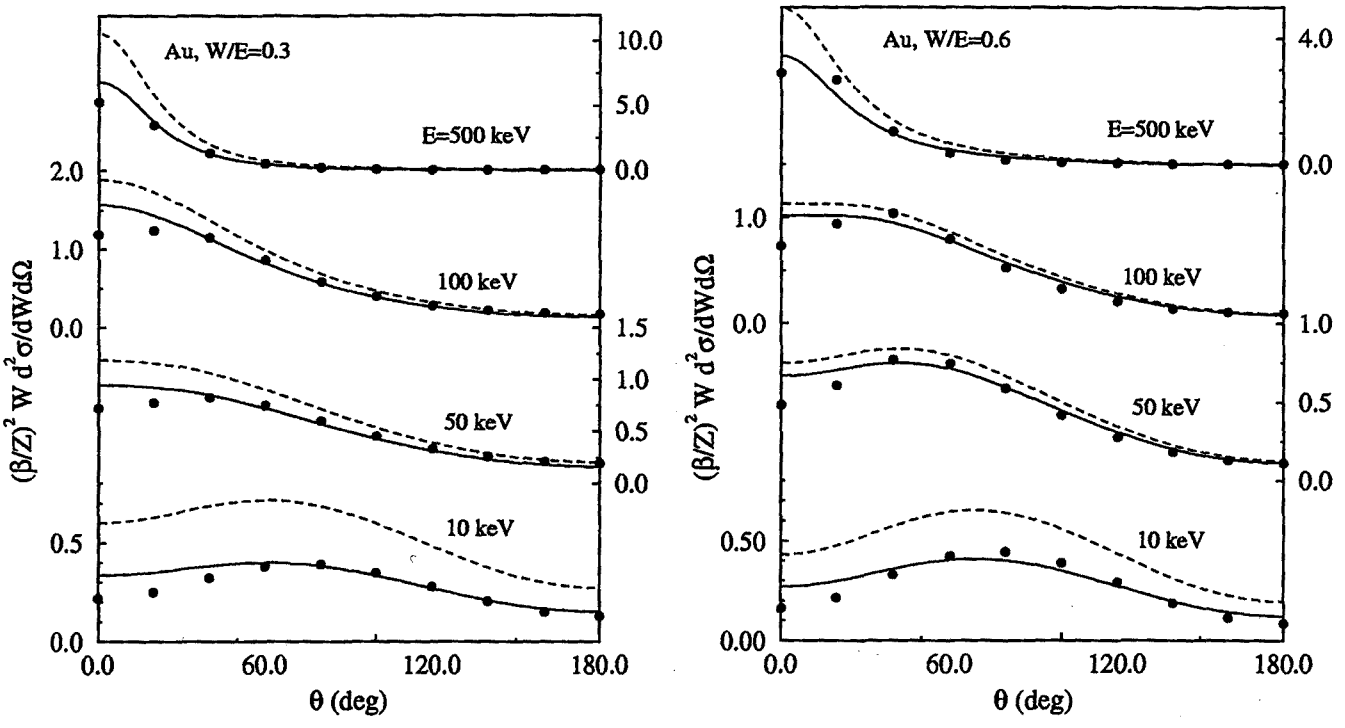

Figure 1.8b. Electron bremsstrahlung reduced DDCSs for Au and different photon-to-electron energy ratios W/E: $W/E = 0.3$ (a), $W/E = 0.6$ (b). Dashed curves, Kirkpatrick-Wiedmann-Statham DDCS (1.38); solid curves, modified Bethe-Heitler DCS with KWS angular distribution (1.56). Dots represent numerical data calculated by Kissel et al.

Eq. (1.48), with the KWS angular distribution (normalized to unity),

$$p_{\mathrm{KWS}}(\cos\theta) = N_\theta \frac{\sigma_x(1-\cos^2\theta)+\sigma_y(1+\cos^2\theta)}{(1-\beta\cos\theta)^2}, \tag{1.56}$$

where

$$N_\theta = \frac{\beta^3(1-\beta^2)}{2\{2\beta\sigma_y - 2\beta(1-\beta^2)\sigma_x + [\log(1-\beta)-\log(1+\beta)](1-\beta^2)(\sigma_y-\sigma_x)\}} \tag{1.57}$$

is a normalization constant such that

$$\int_{-1}^{1} p_{\mathrm{KWS}}(\cos\theta)\mathrm{d}(\cos\theta) = 1. \tag{1.58}$$

The proposed DDCS reads

$$\frac{\mathrm{d}^2\sigma_{\mathrm{BK}}}{\mathrm{d}W\mathrm{d}\Omega} = C_{\mathrm{BH}}\left(\varphi_1(\varepsilon)+\frac{1}{\varepsilon}\varphi_2(\varepsilon)\right)\frac{1}{2\pi}p_{\mathrm{KWS}}(\cos\theta). \tag{1.59}$$

Fig. 1.8 shows bremsstrahlung-reduced DDCSs obtained from the modified Bethe-Heitler formula with dipolar distribution, the KWS formula and the proposed analytical DDCS, Eq. (1.59), for different elements and photon-to-electron energy ratios. We see that the Bethe-Heitler formula with dipolar distribution is in marked disagreement with

the tabulation of Kissel et al. (1983), at least in the considered energy range. On the other hand, the KWS formula is seen to have a nearly correct behaviour of the reduced DDCS as a function of the emitted photon angle. The proposed analytical DDCS predicts values that are in closer agreement with the numerical cross sections tabulated by Kissel et al. (1983).

1.2 Photon interactions

Photons with energy E in the range 0.1-100 keV interact via photoelectric absorption, Compton (incoherent) scattering and Rayleigh (coherent) scattering. Photoelectric absorption is a process in which the photon is absorbed and an atomic electron is ejected from the target atom with kinetic energy equal to $E-E_i$, where E_i is the binding energy of the active atomic electron shell. In Compton scattering, the incident photon interacts with an atomic electron, which is promoted to a free state and a secondary (Compton) photon with energy $E' < E$ is re-emitted. Rayleigh scattering is the process by which photons are scattered without excitation of the target atom, i.e. the energies of the incident and scattered photons are the same. The scattering is qualified as "coherent" as there are interference effects between the waves diffracted by different parts of the atomic charge distribution.

1.2.1 Rayleigh scattering

The atomic DCS per unit solid angle for coherent scattering is given approximately by (see e.g. Born, 1969)

$$\frac{\mathrm{d}\sigma_{\mathrm{co}}}{\mathrm{d}\Omega} = \frac{\mathrm{d}\sigma_{\mathrm{T}}}{\mathrm{d}\Omega}\left[F(q,Z)\right]^2, \tag{1.60}$$

where

$$\frac{\mathrm{d}\sigma_{\mathrm{T}}(\theta)}{\mathrm{d}\Omega} = r_{\mathrm{e}}^2\frac{1+\cos^2\theta}{2} \tag{1.61}$$

is the classical Thompson DCS for scattering by a free electron at rest and $F(q,Z)$ is the atomic form factor. The quantity $r_{\mathrm{e}} = e^2/mc$ is the classical electron radius and q is the magnitude of the momentum transfer given by

$$q = 2(E/c)\sin(\theta/2) = (E/c)\left[2(1-\cos\theta)\right]^{1/2}. \tag{1.62}$$

The atomic form factor can be expressed as the Fourier transform of the atomic electron density $\rho(\mathbf{r})$ which, for a spherically symmetrical atom, simplifies to

$$F(q,Z) = 4\pi\int_0^\infty \rho(r)\frac{\sin(qr/\hbar)}{qr/\hbar}r^2\,\mathrm{d}r. \tag{1.63}$$

$F(q,Z)$ is a monotonically decreasing function of q that varies from $F(0,Z) = Z$ to $F(\infty,Z) = 0$. Accurate atomic form factors obtained from Hartree-Fock atomic structure calculations have been tabulated by Hubbell et al. (1975).

1.2.2 Compton scattering

In Compton scattering, a photon of energy E interacts with an atomic electron, which absorbs it and re-emits a secondary (Compton) photon of energy E' in the direction $\Omega = (\theta,\phi)$ relative to the direction of the original photon. A common practice is to use the Klein-Nishina DCS, which assumes that atomic electrons are free and at rest,

$$\frac{\mathrm{d}^2\sigma_{\mathrm{in}}^{\mathrm{KN}}}{\mathrm{d}E'\mathrm{d}\Omega} = Z\frac{r_{\mathrm{e}}^2}{2}\left(\frac{E_{\mathrm{C}}}{E}\right)^2\left(\frac{E_{\mathrm{C}}}{E}+\frac{E}{E_{\mathrm{C}}}-\sin^2\theta\right)\delta(E'-E_{\mathrm{C}}), \tag{1.64}$$

where

$$E_{\mathrm{C}} \equiv E\frac{mc^2}{mc^2+E(1-\cos\theta)} \tag{1.65}$$

is the energy of the Compton line. The formula (1.64) describes the scattering by Z free electrons at rest, i.e. binding effects are neglected. As a consequence, secondary photons emitted in a given direction θ are assigned a well-defined energy. To partially account for binding effects, some authors use the Waller-Hartree approximation (see e.g. Cooper, 1971) that leads to a DCS equal to the Klein-Nishina DCS multiplied by the incoherent scattering function (tabulated by Hubbell et al., 1975).

A more satisfactory approach is provided by the relativistic impulse approximation (Ribberfors, 1983), which accounts for electron binding effects and Doppler broadening (i.e. the effect of the velocity distribution of atomic electrons). Essentially, the atomic DCS is obtained by performing a Lorentz transform on a reference frame where the target electron is at rest, describing the interaction by means of the Klein-Nishina DCS and inverting the Lorentz transform. After a Compton interaction with the i-th shell, the target electron is ejected to a free state with kinetic energy $E_{\mathrm{e}} = (E-E') - E_i$, where E_i is the ionization energy of the considered shell. Of course, only interactions such that $E_{\mathrm{e}} > 0$ are allowed, which explicitly accounts for the effect of binding.

The atomic DCS obtained from the impulse approximation (Brusa et al., 1996) is approximately given by

$$\frac{\mathrm{d}^2\sigma_{\mathrm{in}}}{\mathrm{d}E'\mathrm{d}\Omega} = \frac{r_{\mathrm{e}}^2}{2}\left(\frac{E_{\mathrm{C}}}{E}\right)^2\left(\frac{E_{\mathrm{C}}}{E}+\frac{E}{E_{\mathrm{C}}}-\sin^2\theta\right)J(p_z)\frac{\mathrm{d}p_z}{\mathrm{d}E'}. \tag{1.66}$$

The momentum transfer vector is defined as $\mathbf{q} \equiv \mathbf{k}-\mathbf{k}'$, where $\mathbf{k}$ and $\mathbf{k}'$ are the momenta of the incident and scattered photons. The quantity p_z is the projection of the initial momentum $\mathbf{p}$ of the bound electron on the direction $-\mathbf{q}$; it is given by

$$p_z \equiv -\frac{\mathbf{p}\cdot\mathbf{q}}{q} = \frac{EE'(1-\cos\theta)-mc^2(E-E')}{c^2q} = mc\frac{E(E'-E_{\mathrm{C}})}{E_{\mathrm{C}}\,cq}. \tag{1.67}$$

The function $J(p_z)$ in Eq. (1.66) is the Compton profile,

$$J(p_z) \equiv \iint \rho(\mathbf{p})\, \mathrm{d}p_x\, \mathrm{d}p_y, \tag{1.68}$$

where $\rho(\mathbf{p})$ is the momentum distribution of the atomic electrons. For an electron in an orbital $\psi(\mathbf{r})$, $\rho(\mathbf{p}) \equiv |\psi(\mathbf{p})|^2$, where $\psi(\mathbf{p})$ is the orbital wave function in the momentum representation. In the Hartree-Fock approximation for closed-shell configurations, the momentum distribution of the electrons in an atomic shell, obtained by adding the contributions of the orbitals in that shell, is isotropic. The atomic Compton profile is given by

$$J(p_z) = \sum_i Z_i\, J_i(p_z), \tag{1.69}$$

where Z_i is the number of electrons in the i-th shell and $J_i(p_z)$ is the one-electron profile of this shell. $J_i(p_z)\, \mathrm{d}p_z$ gives the probability that the component of the electron momentum in a given direction is in the interval $(p_z, p_z + \mathrm{d}p_z)$. Extensive tables of Hartree-Fock Compton profiles for the elements have been published by Biggs et al. (1975).

1.2.3 Photoelectric effect

Photoionization of a given shell is only possible when the photon energy exceeds the corresponding ionization energy, E_i; this gives rise to the characteristic absorption edges in the photoelectric cross section σ_{ph}. In the energy range between successive absorption edges, the atomic photoelectric cross section is a continuous function of the photon energy.

Tables of photoelectric cross sections for all the elements and photon energies from 10 eV to 10^5 MeV have been elaborated by Cullen et al. (1989) on the basis of Scofield's theoretical calculations of subshell photoelectric cross sections (Saloman et al., 1988) and Hubbell's total cross sections (Hubbell et al., 1980). The XCOM program of Berger and Hubbell (1987) generates values of σ_{ph} for all elements and for photon energies in the range from 1 keV to 1 GeV. The Berger-Hubbell values practically coincide with those of Cullen et al., but may differ significantly from previous tabulations. More recently, Henke et al. (1993) have published a compilation of photoelectric cross sections that covers the range E =10 eV - 30 keV for Z = 1-92; their values are again close to those of Berger and Hubbell in the energy range covered by both tabulations.

1.2.4 Attenuation coefficients

The attenuation coefficient of a medium is defined as

$$\mu = \mathcal{N}\,(\sigma_{\mathrm{co}} + \sigma_{\mathrm{in}} + \sigma_{\mathrm{ph}}), \tag{1.70}$$

where σ_{co}, σ_{in} are the total atomic cross sections for Rayleigh and Compton scattering, respectively, which are obtained by integration of the corresponding DCSs. As before, σ_{ph} represents the photoelectric cross section. The quantity μ/ρ, which is independent of the density of the medium, is known as the mass-attenuation coefficient (MAC).

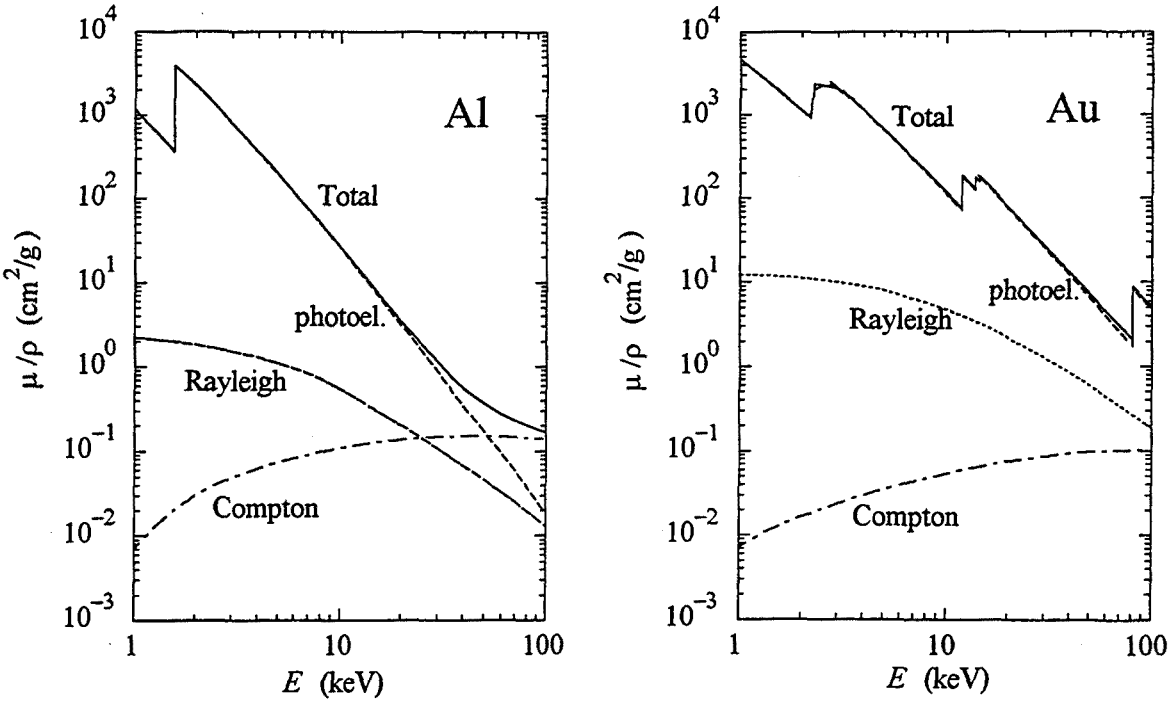

Figure 1.9. Photon mass attenuation coefficients for aluminium and gold (see text for calculation details).

Tabulations of MACs and polynomial approximations have been published by several authors. To our knowledge, the XCOM program (Berger and Hubbell, 1987) and the tabulations of Henke et al. (1993) are the most up to date and reliable general references for MACs. It should be noted, however, that XCOM uses Compton cross sections obtained from the Waller-Hartree theory, which are less accurate than those derived from the impulse approximation. The MACs displayed in Fig. 1.9 are photoelectric and Rayleigh MACs generated by the XCOM program and Compton MACs calculated from the impulse approximation. In all the calculations reported below, we use MACs obtained in this way.

1.3 Atomic relaxation

After ionization of an inner shell, the atom is left in a highly excited state and de-excites by migration of the initial vacancy to outer electron shells through a cascade of electron transitions and energy is released by emission of either fluorescent (or characteristic)

x-rays or Auger electrons. X-rays emitted in the filling of a vacancy in a K-shell are denoted by $K\alpha_1$, $K\alpha_2$, $K\beta$, ... and correspond to K-L3, K-L2, K-M3, ... transitions, respectively. A similar series of lines labelled $L\alpha_1$, $L\alpha_2$, $L\beta_1$, ... arises from transitions in which a vacancy in the L shell is filled by an electron coming from an outer shell. Tables of transition probabilities for the initial vacancy in different atomic shells have been published by Perkins et al. (1991).

The fluorescent yield, ω_i, for the i-th shell or subshell of is defined as $\omega_i = \frac{f_i}{\nu_i}$, where f_i is the average number of fluorescent x-rays emitted as a result of ν_i vacancies created in the considered shell (see e.g. Hubbell et al., 1994). Fluorescence yields of K-shells are relatively well known; those of outer shells require a more detailed definition to account for the occurrence of the Coster-Kronig transitions, which involve migration of a vacancy between subshells of the same shell. Tabulations of fluorescence yields have been published by e.g. Bambynek (1972), Fink and Rao (1974) and more recently reviewed by Hubbell et al. (1994). A related quantity is the line fraction, which is defined as the relative intensity of a given characteristic X-ray in the corresponding series.

Inner-shell ionization can be produced, not only by the impact of the incident electrons, but also by photoelectric absorption (and, to a lesser extent, by Compton interactions) of characteristic X-rays and bremsstrahlung produced elsewhere in the medium. If $E > E_K$, the probability that a photon of energy E is absorbed in the K-shell of an atom is given by

$$P_K(E) = \frac{\sigma_{ph}^K(E)}{\sigma_{ph}(E)}, \tag{1.71}$$

where σ_{ph}^K and σ_{ph} are the partial atomic cross section for K-shell ionization and the total atomic photoelectric cross section, respectively. Therefore, when the photon energy exceeds the K-shell ionization energy, we can consider that the photoabsorption takes place either in the K-shell (with probability P_K) or in outer shells (with probability $1 - P_K$.

From calculated subshell photoelectric cross sections (Cullen et al., 1989) it is found that $P_K(E)$ is practically independent of the photon energy. It can then be estimated from the K-edge jump ratio, which is defined by

$$J_K = \frac{\sigma_{ph}(U_K^+)}{\sigma_{ph}(U_K^-)}, \tag{1.72}$$

where $\sigma_{ph}(U_K^+)$ and $\sigma_{ph}(U_K^-)$ are the total atomic photoelectric cross sections for energies immediately above and below the K-edge, respectively. As a consequence,

$$P_K = 1 - \frac{1}{J_K}. \tag{1.73}$$

Numerical values of this quantity for all elements can be obtained from the photoelectric cross section tables of Cullen et al. (1989).

Chapter 2

Monte Carlo simulation

The DCSs described in the previous chapter furnish the "microscopic" information required for a quantitative description of radiation transport in matter. The penetration and slowing down of a particle (electron or photon) is the result of a sequence of interactions in which the particle is deflected and loses energy. Historically, transport problems were studied on the basis of the Boltzmann equation. This is an integro-differential equation where the unknown is the particle flux, a function that depends on seven independent variables (position, direction of movement, energy and time). In practice, the numerical solution of this equation is extremely difficult (see e.g. Case and Zweifel, 1967). An alternative approach is to take advantage of the random nature of the interactions, which makes the problem particularly suited for solution by Monte Carlo (MC) simulation methods.

The first MC simulations of kV electron transport were performed at the beginning of the sixties, when fast computers became generally available to the scientific community. Since then, MC simulation methods have been widely used to obtain quantitative information on the different signals that can be recorded in electron beam instruments, namely, secondary and backscattered electrons, characteristic x-rays, bremsstrahlung, etc. At the beginning, simulations were based on simple empirical formulations (e.g. Green, 1963; Bishop, 1965; Curgenven and Duncumb, 1971) and occasionally used multiple scattering theory to speed up the simulation, following the ideas introduced by Martin Berger in his seminal paper (Berger, 1963). A second generation of MC studies used simple scattering models, normally a screened Rutherford DCS for elastic scattering and the CSDA for energy losses (e.g. Shimizu et al., 1966; Reimer, 1968, and Murata et al., 1971). The next real improvement was the introduction of energy straggling effects by means of approximate inelastic DCSs (Shimizu et al., 1976; Liljequist, 1978; Salvat and Parellada, 1984).

The limitations of these simple models soon became evident and stimulated the development of simulation codes based on more accurate DCSs. Reimer and Krefting

(1976) demonstrated that the use of elastic DCSs computed by partial-wave analysis largely improved the reliability of the simulation results, especially for low energies. At the end of the seventies, attempts were also made to incorporate detailed inelastic models into MC simulations. The differential inelastic cross section of Gryzinki (1965) has been repeatedly used (e.g. by Ichimura and Shimizu, 1981) to simulate core ionization. Recently, optical-data models have been successfully included in MC simulations (Ding and Shimizu, 1989; Martínez et al., 1990; Jensen and Walker, 1993; Fernández-Varea et al., 1996). Some MC codes are available to the public, for example, Reimer and Stelter (1986) or Hénoc and Maurice (1991) explicitly give the corresponding source listings of their programs.

The simulations described in the present work have been performed using a modified version of the code system PENELOPE. This program, which simulates coupled electron-photon transport, was developed by F. Salvat and co-workers (Salvat et al., 1996) and is available from the Nuclear Energy Agency Data Bank [1].In this chapter we briefly describe the general aspects of the MC simulation method as well as the scattering models and simulation algorithms implemented in PENELOPE. We also provide benchmark comparisons of simulation results with experimental transport data that validate the use of PENELOPE for the energies of interest here.

2.1 General aspects

The MC method consists of the numerical generation of particle trajectories (histories) within a material medium. Each trajectory is viewed as a sequence of free flights of definite length that end with a scattering event, where the particle changes its direction of movement, loses energy and may generate secondary particles. The trajectory finishes when the particle is stopped in the material or escapes from it. Quantities of interest are obtained by averaging over a great number of simulated trajectories. A particular MC simulation method consists of a "scattering model", which is used to describe individual scattering events, and the "simulation algorithm", i.e. the set of numerical procedures used to generate particle trajectories. The reliability of a MC code is then determined by that of the underlying scattering model and by the accuracy of the adopted simulation algorithm.

Let us consider a particle with energy E that can interact with the medium through two independent mechanisms denoted by "A" and "B". In each interaction, the particle loses an energy W, changes its direction of movement and can generate secondary particles. The angular deflection is determinated by the polar scattering angle θ and the azimuthal angle ϕ. The scattering model consists of the set of atomic (or molecular)

[1]Nuclear Energy Agency Data Bank. Le Seine Saint-Germain, 12 Boulevard des Iles, 92130 Issy-les-Moulineaux, France (e-mail: NEA@db.nea.fr)

DCS for the possible scattering mechanism, i.e.

$$\frac{\mathrm{d}^2\sigma_\mathrm{A}}{\mathrm{d}W\mathrm{d}\Omega}(E;W,\theta,\phi) \quad \text{and} \quad \frac{\mathrm{d}^2\sigma_\mathrm{B}}{\mathrm{d}W\mathrm{d}\Omega}(E;W,\theta,\phi), \tag{2.1}$$

which can be derived from experiments or calculated theoretically (see chapter 1). The quantity

$$\mathcal{N}\frac{\mathrm{d}^2\sigma_\mathrm{A}}{\mathrm{d}W\mathrm{d}\Omega}(E;W,\theta,\phi)\mathrm{d}W\mathrm{d}\Omega \tag{2.2}$$

gives the probability per unit path length that the particle has an interaction of type A in the medium, losing an energy between W and $W+\mathrm{d}W$ and changing its direction of movement to the solid angle element $\mathrm{d}\Omega$ around the direction (θ,ϕ). The probability per unit path length that the particle interacts with the medium through the mechanism A, irrespectively of the energy loss and angular deflection, is given by the corresponding inverse mean free path

$$\frac{1}{\lambda_\mathrm{A}} = \mathcal{N}\sigma_\mathrm{A}(E) = \mathcal{N}\int_0^E \mathrm{d}W \int_{4\pi} \mathrm{d}\Omega \, \frac{\mathrm{d}^2\sigma_\mathrm{A}}{\mathrm{d}W\mathrm{d}\Omega}(E;W,\theta,\phi), \tag{2.3}$$

where $\sigma_\mathrm{A}(E)$ is the total (integrated) cross section for interactions of type A. The quantities W, θ and ϕ that determine each interaction event are considered as random variables with a probability distribution function (PDF) given by

$$p_\mathrm{A}(E;W,\theta,\phi) = \frac{1}{\sigma_\mathrm{A}(E)}\frac{\mathrm{d}^2\sigma_\mathrm{A}}{\mathrm{d}W\mathrm{d}\Omega}(E;W,\theta,\phi). \tag{2.4}$$

Considering that the atoms (or molecules) in the medium are oriented at random, the DCS is independent of the azimuthal scattering angle.

The probability of interaction, of any kind, per unit path length is given by

$$\frac{1}{\lambda_\mathrm{T}} = \frac{1}{\lambda_\mathrm{A}} + \frac{1}{\lambda_\mathrm{B}} = \mathcal{N}(\sigma_\mathrm{A}+\sigma_\mathrm{B}) = \mathcal{N}\sigma_\mathrm{T}, \tag{2.5}$$

where λ_T is the total mean free path between collisions and σ_T is the total cross section. The PDF of the path length s between consecutive interactions is given by (see e.g. Salvat et al., 1996)

$$p(s) = \frac{1}{\lambda_\mathrm{T}}\exp(-s/\lambda_\mathrm{T}). \tag{2.6}$$

The kind of interaction taking place is a discrete random variable, which takes the values "A" and "B" with probabilities

$$P_\mathrm{A} = \frac{\sigma_\mathrm{A}}{\sigma_\mathrm{T}} \quad \text{and} \quad P_\mathrm{B} = \frac{\sigma_\mathrm{B}}{\sigma_\mathrm{T}}. \tag{2.7}$$

In summary, the DCSs of the scattering model determine the probability distribution functions of the random variables which characterize a track: 1) the free path between successive scattering events, 2) the kind of scattering event that takes place and 3) the energy loss and the angular deflection in a particular event.

An essential part of any Monte Carlo calculation is the sampling of random variables x from a given PDF $p(x)$. Normally, sampling algorithms transform random numbers, ξ, uniformly distributed in the interval (0,1) into values x that follow the given PDF. Uniform random numbers are provided by available computer routines, the so-called random number generators (see e.g. James, 1980). The simplest sampling algorithms use the inverse transform method, which consists of obtaining x as the solution of the equation

$$\int_a^x p(x)\,\mathrm{d}x = \xi \int_a^b p(x)\,\mathrm{d}x. \tag{2.8}$$

For example, in the case of the exponential distribution (2.6), the inverse transform method gives the sampling formula

$$s = -\lambda_{\mathrm{T}} \ln(1-\xi) = -\lambda_{\mathrm{T}} \ln \xi. \tag{2.9}$$

In the latter equality we have used the fact that $1-\xi$ is also a uniform random number in (0,1); this avoids an unnecessary subtraction. The inverse transform method can also be applied to discrete distributions. Thus, in the case of the distribution given by Eq. (2.7), the sampling formula gives

$$\begin{aligned} x &= A \quad \text{if } \xi < p_{\mathrm{A}} \\ &= B \quad \text{if } p_{\mathrm{A}} \le \xi < p_{\mathrm{A}} + p_{\mathrm{B}}. \end{aligned} \tag{2.10}$$

A detailed review of sampling methods is given in Rubinstein's book (1981).

With the term "simulation algorithm" we refer to the way in which the random particle trajectories are generated. For photons and electrons with relatively low energies, the number of interactions along the particle history is small enough to allow detailed simulation of the individual scattering events in chronological succession. For high-energy electrons, however, the average number of events experienced by the particle is very large (a few thousand for 200 keV electrons), and detailed simulation is too slow for practical uses. In this case, it is convenient to resort to the results of multiple scattering theories to simulate the global effect of all the events that occur along a path segment of a given length. Thus, each trajectory is simulated as a small number of steps, of length much larger than the mean free path between real collisions. This procedure is known as condensed simulation. It is also possible to combine detailed simulation of hard events, with large angular deflections or energy losses, and condensed simulation of soft events, with small deflections and energy losses.

Detailed simulation algorithms proceed as follows. Each particle starts at a given position, with a given initial direction and energy. The state of the particle immediately after a collision is specified by giving its position coordinates $\mathbf{r} = (x, y, z)$, its energy E and the direction cosines of the direction of movement $\mathbf{d} = (u, v, w)$. We have

$$u = \sin\theta\cos\phi$$

$$v = \sin\theta \sin\phi$$
$$w = \cos\phi. \tag{2.11}$$

Let us assume that a trajectory has already been simulated up to a certain state $\mathbf{r}_n, E_n, \mathbf{d}_n$. Then,

1. The mean free path $\lambda_T(E_n)$ is determined (normally interpolated from a table stored in memory) and the length s of the free flight to the next collision is sampled using Eq. (2.9).

2. The particle advances the distance s in the direction of flight $\mathbf{d}$; the following interaction occurs at the position $\mathbf{r}_{n+1} = \mathbf{r}_n + s\mathbf{d}_n$.

3. The kind of interaction is selected from the point probabilities given by Eq. (2.7). The polar scattering angle θ and the energy loss W is sampled from the corresponding DCS. The azimuthal angle ϕ is sampled uniformly in the interval (0,2π).

4. The particle energy is reduced, $E_{n+1} = E_n - W$, and the new direction of movement $\mathbf{d}_{n+1} = (u', v', w')$ is obtained by rotating the unit vector $\mathbf{d}_n = (u, v, w)$ according to the sampled scattering angles,

$$u' = u\cos\theta + \frac{\sin\theta}{\sqrt{1-w^2}}\left[uw\cos\phi - v\sin\phi\right]$$
$$v' = v\cos\theta + \frac{\sin\theta}{\sqrt{1-w^2}}\left[uw\cos\phi + v\sin\phi\right]$$
$$w' = w\cos\theta - \sqrt{1-w^2}\sin\theta\cos\phi. \tag{2.12}$$

The simulation of the trajectory then proceeds by repeating these steps, until the particle energy becomes less than a pre-selected absorption energy E_{abs} or the particle escapes from the material. If, as a result of an interaction, a secondary particle is emitted, the initial state of this particle is stored. Secondary particles generated by the primary particle and its descendants are simulated, after completion of the primary history, down to the adopted absorption energy.

The MC estimate of a quantity Q is obtained as the average of scores of a large number N of simulated histories,

$$Q = \frac{1}{N}\sum_{i=1}^{N} q_i, \tag{2.13}$$

where q_i is the score of the i-th history. The standard deviation σ_Q of the N independent observations is given by

$$\sigma_Q = \sqrt{\frac{1}{N}\,\mathrm{var}(Q)} = \sqrt{\frac{1}{N}\left[\frac{1}{N}\sum_{i=1}^{N} q_i^2 - Q^2\right]}. \tag{2.14}$$

For sufficiently large values of N, σ_Q measures the statistical uncertainty of the result. The error interval $Q \pm 3\sigma_Q$ contains the actual value of Q with 99.7% probability.

In practical calculations it may happen that the quantity of interest Q has a large statistical uncertainty σ_Q, normally because only a very minor fraction of the simulated tracks contribute to the score. The obvious method to reduce the statistical uncertainty is to increase the number of simulated trajectories. Unfortunately, the statistical uncertainty is proportional to $N^{-1/2}$ [see Eq. (2.14)] and, therefore, to reduce the statistical uncertainty to half its value, we need to simulate $4N$ trajectories. Obviously, this sets a practical limit to the attainable accuracy. In some cases, it is possible to reduce the statistical uncertainty, without increasing the computing time, by means of specific variance reduction techniques (Bielajew and Rogers, 1987; Sempau, 1995).

2.1.1 Transport integrals

MC simulation provides essentially the same information as the numerical solution of the Boltzmann transport equation. With MC we obtain "macroscopic" quantities of interest by simply averaging the accumulated scores of a large number of histories. On the contrary, the solution of the transport equation gives the particle flux as a function of position, energy, direction of movement and time (for non-stationary problems). It is of interest to clarify the relationship between the information generated from the MC calculation and the particle flux. Normally, the quantities generated from the MC simulation are integrals of the particle flux with adequate weights.

Let $n(t, \mathbf{r}, E, \Omega)\,\mathrm{d}\mathbf{r}\,\mathrm{d}E\,\mathrm{d}\Omega$ denote the number of particles in the volume element $\mathrm{d}\mathbf{r}$ that move with directions within $(\Omega, \Omega + \mathrm{d}\Omega)$ and energy in the interval $(E, E + \mathrm{d}E)$ at time t. The quantity $n(t, \mathbf{r}, E, \Omega)$ is the particle density and completely describes the transport process. The *particle flux* is defined as

$$\Psi(t, \mathbf{r}, E, \Omega) \equiv v(E) n(t, \mathbf{r}, E, \Omega). \tag{2.15}$$

Notice that $\Psi(t, \mathbf{r}, E, \Omega)\,\mathrm{d}E\,\mathrm{d}\Omega\,\mathrm{d}S\,\mathrm{d}t$ is the number of particles in the ranges $\mathrm{d}E$ and $\mathrm{d}\Omega$ that cross a small area $\mathrm{d}S$ placed at $\mathbf{r}$ and perpendicular to Ω in a time interval $\mathrm{d}t$. Assuming that particles are emitted from the source only during a finite time interval (as happens from real sources), it can be shown that the time-integrated flux formally satisfies the same equation than the solution of a stationary problem (Salvat et al., 1998). Therefore, in electron microscopy and microanalysis, we can consider that the electron beam sets a stationary electron flux inside the sample and the argument t in the function Ψ can be dropped.

In electron microscopy and microanalysis of planar samples, the composition of the scattering medium only depends on one of the space coordinates, say z, and the dependence of the electron flux on the "lateral" coordinates x and y can be disregarded.

Moreover, we consider that the beam has rotational symmetry about the z-axis, so that the flux does not depend on the azimuthal angle ϕ. Under these circumstances, to study the z-dependence of the flux, we can limit ourselves to considering its integral over the two remaining space variables x and y and the azimuthal angle ϕ, i.e.

$$\psi(z,E,\mu) \equiv \int_{-\infty}^{\infty} \mathrm{d}x \int_{-\infty}^{\infty} \mathrm{d}y \int_{0}^{2\pi} \mathrm{d}\phi\, \Psi(\mathbf{r},E,\mathbf{\Omega}), \tag{2.16}$$

where $\mu \equiv \cos\theta$ is the z-component of the unit vector $\mathbf{\Omega}$. The zeroth-order moment of the integrated flux,

$$\psi_0(z,E) = v(E) \int_{-1}^{1} n(z,E,\mu)\, \mathrm{d}\mu, \tag{2.17}$$

is the *total electron flux*. The quantity $\psi_0(z,E)\,\mathrm{d}z\,\mathrm{d}E$ is the sum of the path lengths travelled by all electrons with energies between $(E, E+\mathrm{d}E)$ contained in the volume between z and $z+\mathrm{d}z$. The first-order moment

$$\psi_1(z,E) = v(E) \int_{-1}^{1} n(z,E,\mu)\, \mu\, \mathrm{d}\mu \tag{2.18}$$

can be identified as the *total electron current*. The quantity $\psi_1(z,E)\,\mathrm{d}E$ represents the net number of electrons that cross the plane z with energies within $\mathrm{d}E$: particles that move upwards, i.e. with $\mu > 0$, are counted as "positive" and those that move downwards, with $\mu < 0$, are counted as "negative". Thus,

$$\psi_1(z,E) = \int_{-1}^{0} \psi_{\mathrm{B}}(z,E,\mu)\, \mu\, \mathrm{d}\mu + \int_{0}^{1} \psi_{\mathrm{F}}(z,E,\mu)\, \mu\, \mathrm{d}\mu, \tag{2.19}$$

where $\psi_{\mathrm{B}}(z,E,\mu)$ and $\psi_{\mathrm{F}}(z,E,\mu)$ are the backward and forward components of the flux. Quantities of interest can be expressed as integrals of these two functions:

- The backscattering coefficient η, i.e. the fraction of electrons that, after penetrating the material, return to the vacuum from the irradiated surface is given by

$$\eta = J_0^{-1} \int \mathrm{d}E \int_{-1}^{0} \mathrm{d}\mu\, \psi_B(0,E,\mu)|\mu| \tag{2.20}$$

  where

$$J_0 \equiv \int \mathrm{d}E \int_{0}^{1} \psi_{\mathrm{F}}(0,E,\mu)\mu \tag{2.21}$$

  is the incident electron current.

- The angular distribution of backscattered electrons,

$$P_{\mathrm{B}}(\mu) = J_0^{-1} \int \mathrm{d}E \psi_{\mathrm{B}}(0,E,\mu)\, |\mu|. \tag{2.22}$$

- The energy spectrum of backscattered electrons,

$$P_{\mathrm{B}}(E) = J_0^{-1} \int_{-1}^{0} \mathrm{d}\mu \psi_{\mathrm{B}}(0,E,\mu)\, |\mu|. \tag{2.23}$$

- The energy and angular distribution of backscattered electrons,

$$P_{\mathrm{B}}(E,\mu) = J_0^{-1}\,\psi_{\mathrm{B}}(0,E,\mu)\,|\mu|. \tag{2.24}$$

- The depth-dose function, which is defined as the energy deposited per unit depth,

$$D(z) = J_0^{-1}\int \mathrm{d}E\; S(E)\int_{-1}^{1}\mathrm{d}\mu\psi(z,E,\mu), \tag{2.25}$$

  where $S(E)$ is the stopping power.

- The ionization-depth distribution

$$\phi(z) = J_0^{-1}\int \mathrm{d}E\,\mathcal{N}\sigma(E)\int_{-1}^{1}\mathrm{d}\mu\,\psi(z,E,\mu), \tag{2.26}$$

  where $\sigma(E)$ is the total ionization cross section for the considered shell.

2.2 The simulation code PENELOPE

The simulation package PENELOPE consists of a series of FORTRAN 77 subroutines which perform MC simulation of coupled electron-photon showers, in arbitrary materials, covering the energy range from about 1 keV to 1 GeV. It allows users to write their own simulation code to follow the particle tracks generated by PENELOPE and to keep score of the quantities of interest. The code system also contains a geometry subroutine package (for simulation with complex material systems) and interaction forcing subroutines (a variance reduction method).

The atomic DCSs adopted in PENELOPE are simple analytical functions of the scattering angle and energy loss. These DCSs have a physically reasonable shape and allow random sampling of the scattering angle and energy loss in individual interactions in a completely analytical way, so that sampling errors that could originate from numerical interpolation are completely avoided. Although these analytical DCSs are approximations to the actual ones, they lead to essentially the same simulation results, only provided that the scattering is multiple (i.e. the average number of events along an electron track must be of the order of 20 or larger). The validity of the whole simulation scheme rests on the fact that multiple scattering distributions are determined by the values of a few integrals of the DCSs; the effect of finer details is washed out after repeated interactions. This statement can be "experimentally" verified through Monte Carlo simulation; a formal proof can also be given on purely theoretical grounds (Fernández-Varea et al., 1993b). Thus, the simulation code can be largely simplified by using analytical approximate DCSs leading to the correct values of these relevant integrals. The price paid for this simplicity is that simulation results are reliable only under multiple scattering conditions, a condition which is normally fulfilled in the cases we shall consider.

2.2.1 Electron transport

The DCS for single elastic scattering of electrons is expressed as a combination of the Wentzel (screened Rutherford) DCS and a fixed-angle scattering process, referred to as the model W2D (Baró et al., 1994),

$$\frac{\mathrm{d}\sigma_{\mathrm{W2D}}}{\mathrm{d}\Omega} = \frac{\sigma_{\mathrm{el}}}{4\pi}\left[(1-B)\frac{4a(1+A)}{(1-\cos\theta+2A)^2} + B\delta(\cos\theta-\cos\theta_0)\right]. \tag{2.27}$$

The parameters A, B and θ_0 are calculated by requiring that "realistic" values of the mean free path between collisions and the mean and the variance of the angular deflection in each elastic collision are exactly reproduced. In fact, the precise form of the adopted DCS is quite irrelevant and accurate results can also be obtained by using other analytical DCSs that reproduce the total and two first transport cross sections, provided the scattering is multiple. The required mean free path λ_{el} and the first λ_1 and second λ_2 transport mean free paths have been calculated (and stored in a database) for the atomic number elements ranginf from Z =1–92 and energies from 100 eV to 100 keV using the Dirac partial-wave method with the free-atom Dirac-Hartree-Fock field corrected for exchange effects (Mayol and Salvat, 1997). This simple model allows us to considerably reduce the information required for the simulation: instead of the DCS, a function of the energy and scattering angle, we only need the total and transport cross sections, three functions of the energy. Moreover, the sampling of scattering angle is done analytically.

The DCS for inelastic collisions is based on the simple GOS model proposed by Liljequist (1983). This model associates a single oscillator to each atomic shell with strength f_i equal to the number of electrons in the shell, and resonance energy $W_i = aE_i$, where E_i is the ionization energy of the shell and a is an adjustable parameter. The Liljequist GOS can be written as

$$\frac{\mathrm{d}f(Q,W)}{\mathrm{d}W} = \sum_{i=1}^{M} f_i F_\delta(W_i;Q,W), \tag{2.28}$$

where the excitation spectrum $F_\delta(W_i;Q,W)$ of the i-th oscillator is

$$F_\delta(W_i;Q,W) = \delta(W-W_i)\Theta(W-Q) + \delta(W-Q)\Theta(Q-W), \tag{2.29}$$

where $\delta(x)$ is the Dirac delta function and $\Theta(x)$ is the step function. Excitations of the conduction band are accounted for by a single oscillator with binding energy $U_{\mathrm{p}} = 0$, oscillator strength f_{cb} and resonance energy W_{cb}. The parameters W_{cb} and f_{cb} are the plasmon energy and the effective number of electrons participating in the plasmon excitation. The first term in (2.29) corresponds to excitations with small momentum transfer, that is, distant collisions (large impact parameter), with a resonant-like character ($W = W_i$). The second term corresponds to close collisions, which are described

as binary collisions with free electrons at rest ($Q = W$) by means of the Møller formula (1.26).

The excitation energies and oscillator strengths must satisfy the Bethe sum rule (1.18) and the relation (1.31), that is

$$\sum f_i = Z, \quad \sum f_i \ln W_i = Z \ln I. \tag{2.30}$$

The value of a is determined in such a way that the mean excitation energy I recommended by Berger and Seltzer (1982) is exactly reproduced. The model permits the evaluation of the inelastic mean free path and the stopping power analytically. The calculated stopping powers normally agree with those recommended by the ICRU (1984) to within 0.05%, for the whole energy range covered by the ICRU tabulation. Secondary electron emission is also simulated according to the Liljequist oscillator model. It is assumed that, as a result of an inelastic collision with an oscillator of energy E_i, a secondary electron with energy $W - E_i$ is ejected in the direction of the momentum transfer.

In PENELOPE, simulation of bremsstrahlung emission is performed by using the modified Bethe-Heitler DCS, Eq. (1.55). The polar angle of the photon is sampled from the distribution obtained from the classical dipole distribution (1.54).

PENELOPE generates electron histories by means of a mixed procedure. Interactions of the electrons with the medium are classified as hard events, in which the angle of deflection θ and the energy loss W are greater than certain cut-offs θ_S and W_S, and soft interactions (with $\theta < \theta_S$ or $W < W_S$). Hard events are simulated in detail; the effect of the usually many soft interactions that occur between a pair of consecutive hard events is described as a single "artificial" event in which the particle is deflected and loses energy according to a multiple scattering theory. Between each pair of consecutive (hard or artificial) events the particle "flies" freely with a well-defined energy. The angle cut-off θ_S is automatically adjusted by the program in such a way that the average deflection in each hard elastic event is nearly independent of the electron (or positron) energy, whereas the energy loss cut-off W_S is directly set by the user. The practical advantage of mixed simulation is that the calculation of soft events is largely simplified. As the generation of these events takes up a considerable fraction of the computer time, mixed simulation is normally much faster than detailed simulation.

When an electron arrives at a surface separating two materials, it is stopped just after the interface, and simulation is continued using the scattering data of the new medium (Baró et al., 1995).

2.2.2 Photon transport

The considered photon interactions are coherent (Rayleigh) scattering, incoherent (Compton) scattering and photoelectric absorption. The DCSs implemented in PENELOPE are those described in section 1.3. All random variables are generated by using purely analytical expressions, so that the structure of the simulation code is very simple. The simulation of photon histories is performed by using the conventional detailed simulation method, irrespective of the photon energy.

2.3 Comparison of simulation with experimental data

In order to demonstrate the reliability of PENELOPE for electron transport studies in the kV range, simulated electron backscattering coefficients and 3D dose distributions are compared with experimental results. In the calculations, the absorption energy $E_{\rm abs}$ is set to 100 eV. In each case, the number of generated primary electron historys tracks was of the order of 100,000 for medium and high atomic number elements and 200,000 for light elements. The statistical uncertainties of the results (3σ) are normally less than 1%.

2.3.1 Backscattering coefficient

In Fig. 2.1, simulated backscattering fractions for monoenergetic electron beams impinging normally on homogeneous elemental samples of different atomic number are compared with values measured by different groups (Hunger 1979, Drescher et al. 1970, Neubert and Rogaschewski 1984, Massoumi et al. 1991, Cosslett and Thomas 1965). The continuous curves in Fig. 2.1 represent the function

$$\eta(Z,E) = a_1(Z) + a_2(Z)\, Z\, (E/eV)^{-1/4} \tag{2.31}$$

with the parameters determined by numerical fitting of the simulated backscattering coefficient of each element. It is worth pointing out that the backscattered fraction is the result of a delicate competition between elastic and inelastic scattering. Moreover, electrons are backscattered after travelling different path lengths inside the sample. Those with large paths experience multiple collisions and are thus well described by the theory.

However, a fraction of electrons leave the sample after travelling comparatively short path lengths and experience only single or plural scattering. Under these circumstances the validity of the approximate elastic cross sections and the simulation scheme is open to question. Therefore, the backscattering coefficient represents a stringent global test of the simulation algorithm. The spread of experimental data from different authors in Fig.

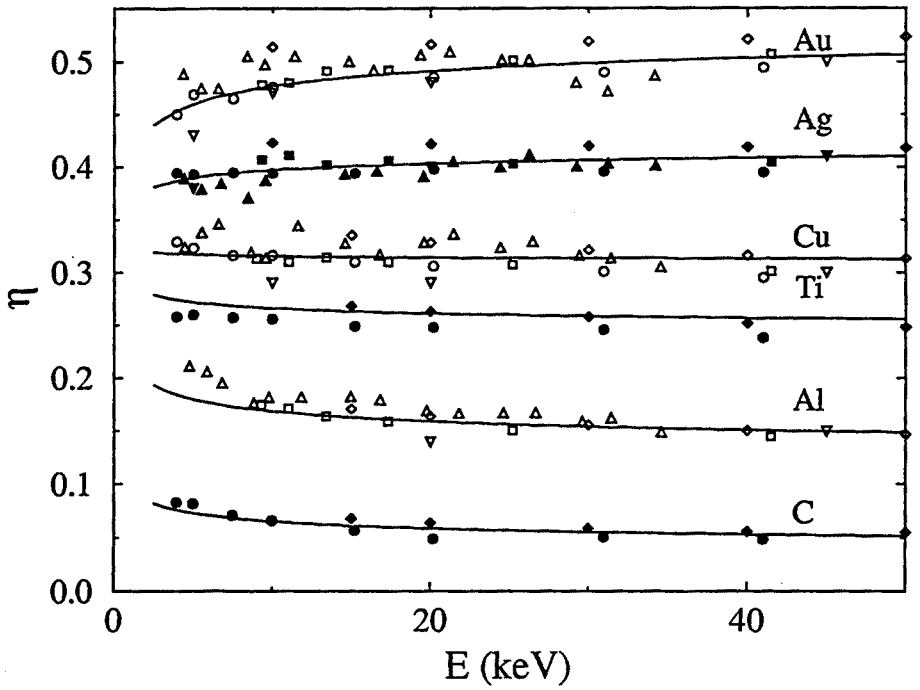

Figure 2.1: Backscattering coefficient as a function of incident energy. Experimental data are from Hunger (1979) (circles), Drescher et al. (1970) (squares), Neubert and Rogaschewski (1984) (diamonds), Massoumi et al. (1991) (triangles) and Cosslett and Thomas (1965) (inverted triangles). Solid lines represent Monte Carlo results.

2.1 indicates that these are affected by considerable instrumental uncertainties. Simulation results are seen to agree reasonably well with the "average" of the experiments. A systematic study of electron backscattering in the keV range using PENELOPE has been performed by Acosta et al. (1996).

2.3.2 Dose distributions

Simulated depth- and lateral-dose distributions for electrons with different energies in silicon (normal incidence) are compared with experimental data of Werner et al. (1988) in Fig. 2.2. These distributions were measured from the current induced by the electron beam in a p-n junction. The simulated depth-dose distributions practically coincide with the experimental results. In order to account for the finite width of the junction and the electron diffusion length, simulated lateral-dose distributions have been convoluted with a Gaussian profile (with a fixed width, independent of the beam energy). The resulting curves agree satisfactorily with the measured data; the differences are probably due to spatial inhomogeneities of the junction. Thus, it may be concluded that PENELOPE gives a realistic description of electron trajectories and spatial dose distributions.

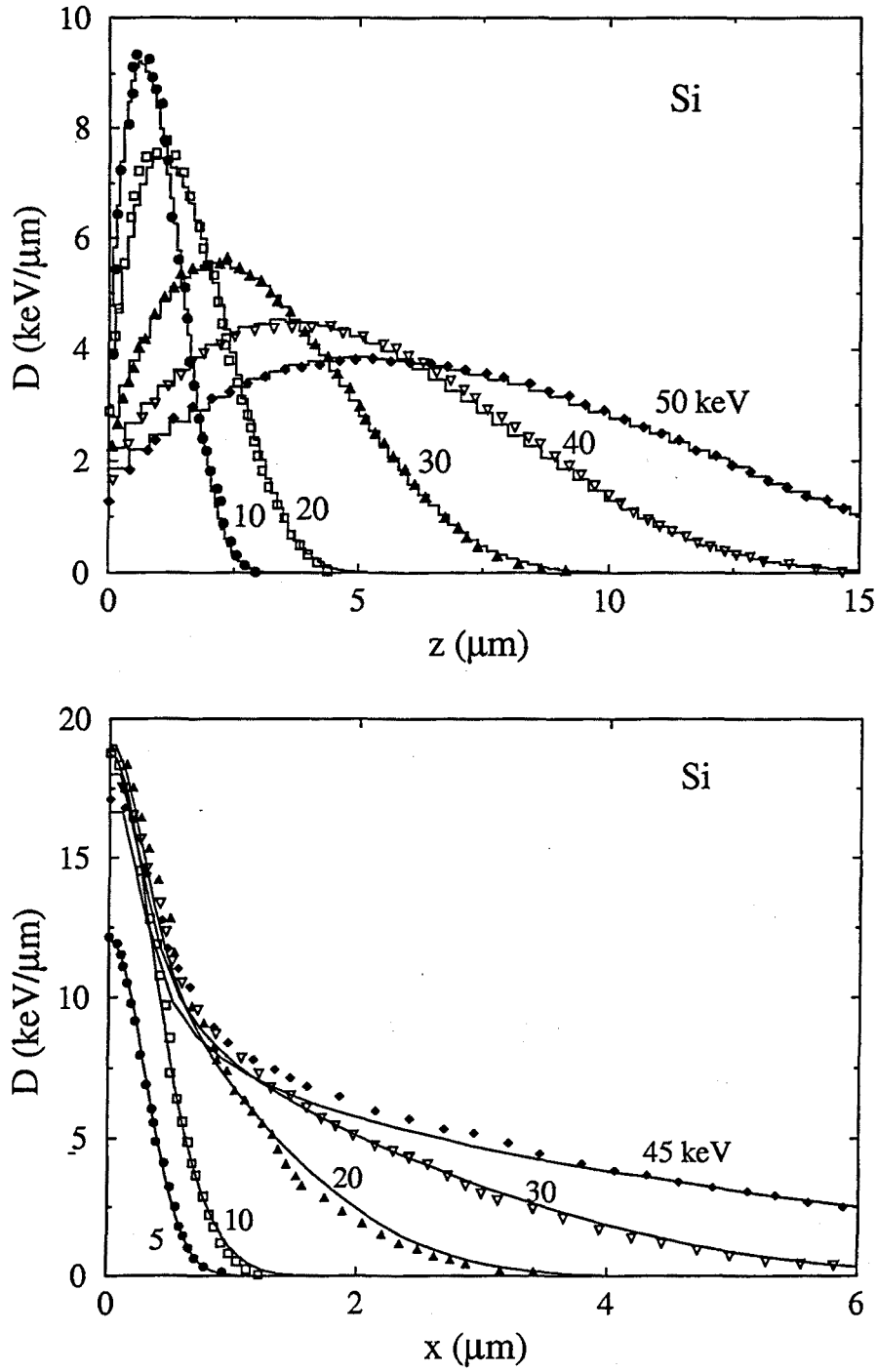

Figure 2.2: Depth-dose distributions (a) and lateral dose distributions (b) in silicon for electron beams of the indicated energies at normal incidence. Experimental data are from Werner et al. (1988). Histograms (a) and curves (b) are Monte Carlo results.

Chapter 3

X-ray measurement with the electron microprobe

The electron microprobe (also called x-ray microprobe) is an instrument which allows us to measure the x-ray emission in solids under electron irradiation. X-rays can be measured by an energy dispersive spectrometer (EDS), using a solid-state x-ray detector, and/or by a wavelength dispersive spectrometer (WDS), which uses a diffracting crystal monochromator. Normally, the electron microprobe is used to perform electron probe microanalysis (EPMA) of materials; the local composition of the studied sample is obtained from the energy (or wavelength) spectrum of x-rays generated by a focused kV electron beam. With appropriate targets, we can also use it to deduce basic quantities of interest, such as cross sections for ionization or bremsstrahlung production, and depth distribution of ionization.

The first electron microprobe was developed by Raimond Castaing in 1952 [1] by fitting a crystal spectrometer to a modified electron microscope. Using the developed instrument, Castaing established the basic principles for quantitative EPMA. A few years later, in 1958, the French company Cameca manufactured the first commercial electron microprobes. Since then, many technical improvements in both the probe-forming system and in the x-ray spectrometers have been performed. One of the important improvements for x-ray measurement has been the development of solid-state lithium-drifted silicon, Si(Li), detectors, which have been successfully incorporated into electron microprobes and electron microscopes.

Electron microscopes that have attached an x-ray spectrometer can be used as electron microprobes by keeping the focussed beam stationary on a sample point. Microprobes and microscopes have different performances of the probe-forming system and of the x-ray spectrometers. In principle, electron microprobes can supply electron cur-

[1] Professor Raimond Castaing passed away during the elaboration of the present thesis.

rents with higher stability than electron microscopes and are usually equipped with WDSs, which produce x-ray spectra with high peak-to-background ratios. Moreover, electron microprobes are normally computer controlled and therefore systematic x-ray measurement can be more easily performed.

In the present chapter we describe the features of the electron microprobe, particularly as regards the aspects of x-ray detection. We also describe the particular characteristics of the microprobe used in this work. It is worth pointing out that knowledge of the detection characteristics of the spectrometer is of great importance for a proper interpretation of measured x-ray spectra. Finally, the statistical uncertainties of x-ray measurements are briefly given.

3.1 The electron column

The electron column consists of the electron gun and the electromagnetic lens system. The electron gun acts as a source of electrons. It is commonly a tungsten filament, which is heated to liberate electrons by thermionic emission. The filament is held at a negative potential by a power supply, which accelerates the electrons escaping from the filament through an aperture. Typical accelerating voltages range from 1 kV up to 50 kV. The electromagnetic lenses are used to focus the electron beam onto the target, with a final diameter of about 0.1-1 μm. They are also used to control the electron current, i.e. the number of incoming electrons per unit time, with values typically of $\sim$1-300 nA, that is $\sim 10^9$-10^{12} electrons per second. The electron current can be measured with a Faraday cup and stabilized by means of a beam regulator device, to maintain a highly stable current during a long period of time. The sample is connected to ground to ensure electron conductivity.

Conventional high vacuum technology is generally used in order to prevent oxidation of the filament, breakdown of the accelerating voltage, and scattering of the electrons. The specimen chamber usually contains hydrocarbons which are originated mainly from diffusion pump and rotatory pump oil. Under the electron irradiation, these hydrocarbons may be "cracked" at the point of electron impact, producing carbon contamination. In order to minimise this contamination, the electron microprobe is equipped with a liquid nitrogen "cold finger", placed close to the specimen, and an air (oxygen) jet, directed towards the point of electron impact.

An optical microscope co-axial to the electron beam is commonly used to locate the areas of interest in the sample. For the same purpose, the beam can be scanned as in conventional scanning electron microscopes. Images can be generated by using the signal from an electron detector, which usually records secondary and/or backscattered electrons from the target.

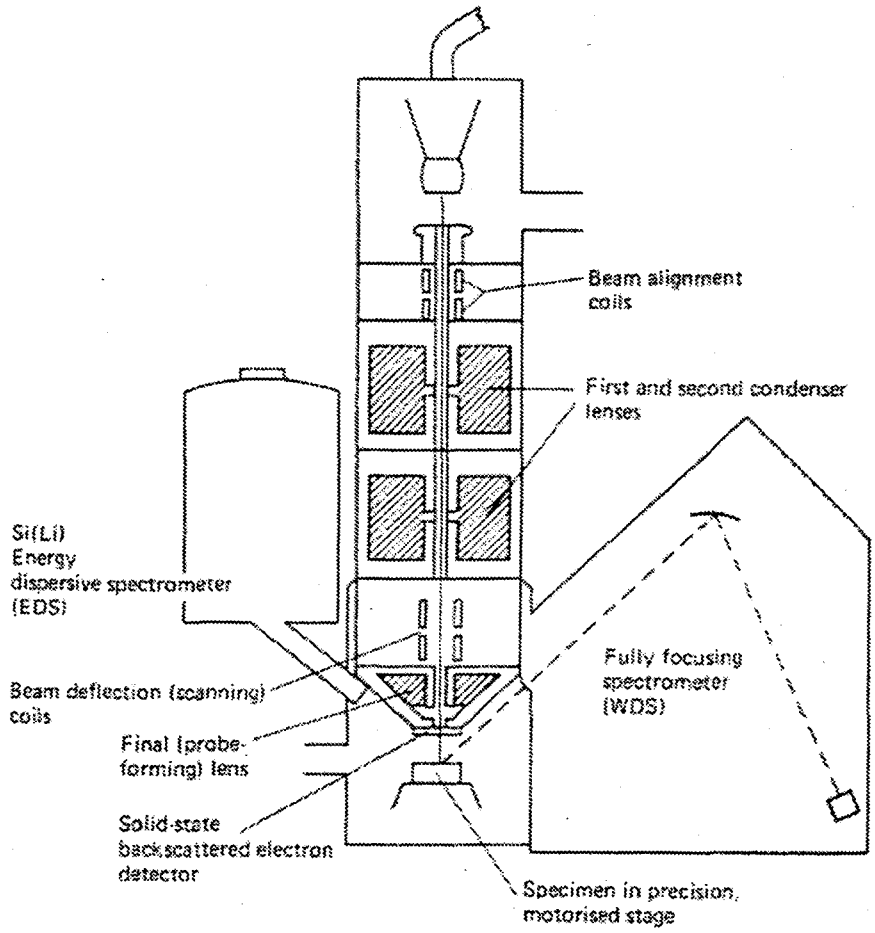

Figure 3.1: Cross section of a typical electron microprobe.

3.2 Energy dispersive spectrometer

The energy dispersive spectrometer uses a solid-state x-ray detector, usually a crystal semiconductor such as Si or Ge. In the first case, it is necessary to "drift" it by introducing lithium in order to compensate the impurities, present even in the most refined crystals. Lithium-drifted silicon crystals are usually referred to as Si(Li). X-rays are absorbed by the crystal atoms through photoelectric effect generating photoelectrons and Auger electrons, which in turn lose energy partly by raising valence electrons to the conduction band. The number of electron-hole pairs created is proportional to the x-ray energy; therefore, if a bias is applied across the crystal, a small current proportional to the energy of the absorbed x-ray is produced. The front surface of the crystal is covered by a thin metallic layer, usually gold, to apply the bias potential. In practice, a portion of the crystal close to the surface behaves as a "dead layer" (Statham, 1981).

The crystal is kept at low temperature in vacuum in order to avoid thermal fluctuations. This requires a separation window to protect the crystal when the chamber is

vented. Traditionally, the window is made of Beryllium, which allows almost a complete transmission of x-rays with energies greater than $\sim$ 1 keV. Pulses from the detector are amplified with the aid of a field emission transistor. To minimize the effect of the noise, the signal is averaged over a time interval, typically of a few tens of microseconds (time constant). For this reason, there is a dead time from the arrival of a pulse to the moment when the system is able to process another pulse, this time being related to the time constant. To avoid corrupted pulse measurements due to the simultaneous arrival of two pulses, a pulse pile-up rejector is used. Finally, amplified pulses are converted into an energy spectrum by a multichannel pulse-height analyzer.

Fluctuations of the number of electron-hole pairs generated by x-rays of a given energy, together with electronic noise, give rise to Gaussian broadening of the pulse-height distribution. The broadening is measured by the Full Width at Half Maximum (FWHM) of the peak, which can be written as

$$\mathrm{FWHM} = \sqrt{N^2 + (2.355)^2 F \varepsilon E} \tag{3.1}$$

where N is the electronic noise, F is the Fano factor, ϵ is the average energy necessary to create an electron-hole pair and E is the energy of x-rays. The Fano factor accounts for the fact that the events causing electron-hole pair creation are not statistically independent (Reimer, 1985).

EDS spectra are influenced by various detection artifacts, mainly of an electronic origin, such as pulse pile-up peaks and silicon escape peaks. Pulse pile-up peaks occur when two incoming x-rays reach the detector at the same time, and therefore they give a single pulse. This effect is greatly reduced by the pulse pile-up rejector, but it can never be completely eliminated. As the probability of such coincidences depends mainly on the count-rate, it can be reduced by decreasing the flux of incoming x-rays. Escape peaks are due to x-rays generated in the crystal that escape from it which give rise to a peak with a lower energy. For example, in Si(Li) detectors, the escape peak is found at 1.74 keV (the energy of the Si Kα line) below the proper peak. Peaks can also present tails on the low-energy side, due to incomplete charge collection (see e.g. Campbell and Wang, 1991). Interaction of x-rays in the crystal dead layer can result in fluorescent x-rays, i.e. Si Kα in Si(Li), which can also be detected. Finally, stray radiation coming from various parts of the microprobe chamber and energetic backscattered electrons may also be detected and contribute mainly to the spectral background.

In the EDS, the intrinsic efficiency ϵ is essentially equal to unity over a wide photon energy interval ($\sim$3-15 keV). It takes lower values at low photon energies, because of absorption in the different inactive layers in front of the intrinsic zone of the detector, and at high energies, due to partial transmission through the intrinsic zone. As a first approximation, ϵ can be computed by assuming exponential attenuation of the photon beam in the inactive layers and in the intrinsic zone (see e.g. Statham, 1981)

$$\epsilon(E) = \exp\left[-\left(\mu_{\mathrm{Be}}(E)\, t_{\mathrm{Be}} + \mu_{\mathrm{Au}}(E)\, t_{\mathrm{Au}} + \mu_{\mathrm{Si}}(E)\, t_{\mathrm{Si}}\right)\right] \times$$

$$\{1 - \exp[-\mu_{Si}(E)\ T_{Si}]\}\,, \tag{3.2}$$

where μ_{Be}, μ_{Au} and μ_{Si} are the corresponding MACs and t_{Be}, t_{Au}, t_{Si} and T_{Si} are the thicknesses of the Be window, Au contact layer, Si dead layer and Si(Li) active region, respectively. On the other hand, the solid angle subtended by the detector is almost constant and it can be approximated by the ratio A/d^2, where A is the area of the detector and d the detector-to-source distance, with typical values of 10^{-2}–10^{-3} srad. The parameters required to compute the efficiency are usually provided by the manufacturer.

A critical step in x-ray measurement with EDS is the accurate determination of the peak intensities, which require the description of the continuous component of the x-ray spectra. The formula of Kramers (1923), with parameters evaluated experimentally and additional correcting factors to take into account x-ray absorption in the target and the detector and electron backscattering, has been widely used (see e.g. Trincavelli et al., 1998). An alternative procedure is to remove background by mathematical filtering or by fitting a polynomial expression. The simplest method to measure peak intensities is to sum the contribution of the channels within a certain energy window. However, care must be exercised to avoid overlap effects between adjacent peaks. Alternatively, a Gaussian distribution can be fitted to each peak (suitably modified to account for the incomplete charge collection).

3.3 Wavelength dispersive spectrometer

The wavelength-dispersive spectrometer (WDS) consists of a crystal monochromator and an x-ray detector, usually a gas proportional counter, arranged in such a way that x-rays impinging on the crystal are diffracted according to Bragg's law and some of them reach the detector and are recorded. The Bragg law reads

$$n\,\lambda = 2\,d\,\sin\theta, \tag{3.3}$$

where λ is the x-ray wavelength, n is the diffraction order, d is the spacing between atomic planes of the monochromator crystal and θ is the angle of incidence of the x-rays.

With flat crystals and point x-ray sources, Bragg reflection occurs only on a small portion of the crystal surface. Improved reflection is obtained by placing the target, the crystal and the detector on a focal circle of radius R (the Rowland circle) and bent the atomic planes of the crystal to a radius $2R$. This focussing geometry is known as the "Johann" type. Much improved reflection is obtained if the crystal surface is bent to the radius R ("Johansson" type) as shown in Fig. 3.2. With this arrangement, the angle of incidence of x-rays is constant over the line defined by the intersection of the Rowland circle plane and the crystal surface. Coordinated mechanical rotation

of the crystal and the detector allows us to record the x-ray spectrum as a function of wavelength. In the focussing geometries, the source-crystal distance is proportional to $\sin\theta$ (see e.g. Reed, 1993) and thus proportional to the wavelength. Therefore, the crystal is simultaneously rotated and moved along a straight line by means of mechanical linkage. This allows calibration of the wavelength by just measuring the source-crystal distance and moreover, the take-off angle is kept constant for all wavelengths.

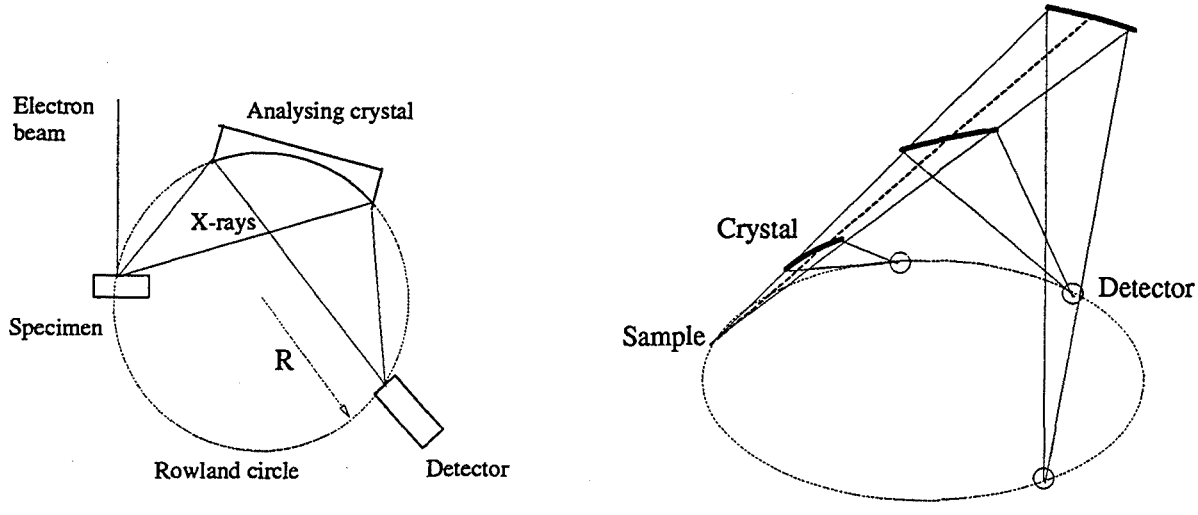

Figure 3.2: (a) Typical geometry of a "Johansson"-type WDS. The surface of the monochromator crystal is bent with curvature radius R equal to that of the Rowland circle. (b) Movement of the analyzing crystal and of the detector fulfilling the Rowland condition.

Besides mechanical limitations of the crystal driver, the range of reflected wavelengths is only limited by the crystal interatomic spacing d and, therefore, crystals with different spacings are required to cover a wide wavelength range. Crystals commonly used for microanalysis are Lithium Fluoride (LIF), Pentaerythritol (PET), and Thallium Acid Phthalate (TAP). The wavelength range covered by using these three crystals is $\sim$ 1-24 Å. For longer wavelengths, multilayer soap films consisting of layers of heavy metal atoms separated by CH_2 chains, such as lead stearate (Pb-STE) can be used. Layered synthetic multistructures (LSM) consisting of many alternating layers of high- and low-Z materials, such as W/Si, Ni/C and Mo/B_4C can also be employed. In these cases, d is equal to the sum of the thickness of one layer pair of the high-Z and low-Z materials. Table 3.1 shows the different crystals used typically for x-ray microanalysis, with the corresponding wavelength ranges.

The gas proportional counter consists of a gas-filled tube with a coaxial wire held at a potential of 1-2 kV with respect to the outer wall of the tube. X-rays enter the counter through a window; they are absorbed by the gas molecules through the photoelectric effect and generate free photoelectrons, which are accelerated by the electric field and produce a cascade of secondary electrons. As a result, each incoming x-ray produces a pulse whose height is proportional to the energy of the x-ray. The output pulses are

Table 3.1: Crystals used as a monochromator in wavelength dispersive spectrometers for x-ray microanalysis, with the corresponding interatomic spacings, wavelength ranges and elements that can be recorded using K, L and M lines.

Crystals (for EPMA)	$2d$ (Å)	λ (nm)	Z (K)	Z (L)	Z (M)
Lithium Fluoride (LIF)	4.027	0.097-0.365	20-36	50-89	
Pentaerythritol (PET)	8.742	0.212-0.792	14-24	36-63	71-92
Th. Acid Phthalate (TAP)	25.9	0.623-2.33	9-14	24-39	53-79
Lead stearate (Pb-STE)	100	2.42-9.06	5-7	17-23	
LSM W/Si	60	1.451-5.440	6-11	20-28	
LSM Ni/C	95	1.890-7.070	5-8	17-25	
LSM Mo/B_4C	200	4.765-17.85	4-5	17-20	

sent to a pulse-height analyzer (PHA) which counts pulses with selected heights –usually contained within a certain voltage window. Visualization of the PHA display helps us to properly select the values of the counter high-voltage, the gain and the discriminatory settings (baseline and window). Proportional counters can be of the flow-type, in which case the gas escapes through the window and therefore must be supplied continuously, or of the sealed-type. The lowest detectable energy is limited by the absorption of x-rays in the entrance window.

The absolute efficiency of the WDSs depends on the solid angle of collection, the crystal reflection efficiency and the efficiency of the proportional counter. The solid angle subtended by the crystal changes as the crystal moves, with typical values of $\Delta\Omega < 10^{-3}$ srad. The crystal reflection efficiency, i.e. the fraction of x-rays reflected on the crystal, depends on both the geometry and the properties of the crystal (dislocations, surface texture, stress, stability and thermal expansion). The efficiency of the proportional counter depends on the detector window and the fraction of the incident x-rays absorbed in the counter itself. Moreover, owing to the mechanical nature of the spectrometer and to fluctuations in the density of the counter gas, the efficiency of the WDS may change with time. These facts make it difficult to estimate the WDS efficiency by relatively simple calculations (Smith and Reed, 1981; Wernisch, 1985).

The standard procedure to obtain the net peak intensity is to record the counting rate at the channel corresponding to the maximum of the peak, and at two background positions at both sides of the peak. Background intensity is then obtained by simple linear interpolation and subtracted from the measured counting rate. To save time and to avoid spectrometer motion and possible inaccuracies due to the proximity of other peaks, it is usual to record the background at only one side of the peak and use a previously calculated factor to obtain the background, at the same distance, on the other side of the peak. These procedures give, in general, accurate results because of

the high peak-to-background ratio of wavelength dispersive x-ray spectra.

Higher order reflections, i.e. $n = 2, 3, 4, \cdots$ [see Eq. (3.3)] must not be ignored since they are a source of spectral interference. In general, it is possible to suppress the influence of high-order diffraction peaks by properly setting a narrow window in the PHA. Furthermore, for low-energy x-rays, the PHA settings should be carefully chosen in order to separate counter signals from electronic noise of the amplifier (see e.g. Schalkoord et al., 1990). As an example, Fig. 3.3 shows the 9th order of diffraction of Fe K$\alpha_{1,2}$, which appears close to Fe Lα. By using a very narrow window in the PHA, the interference is completely removed.

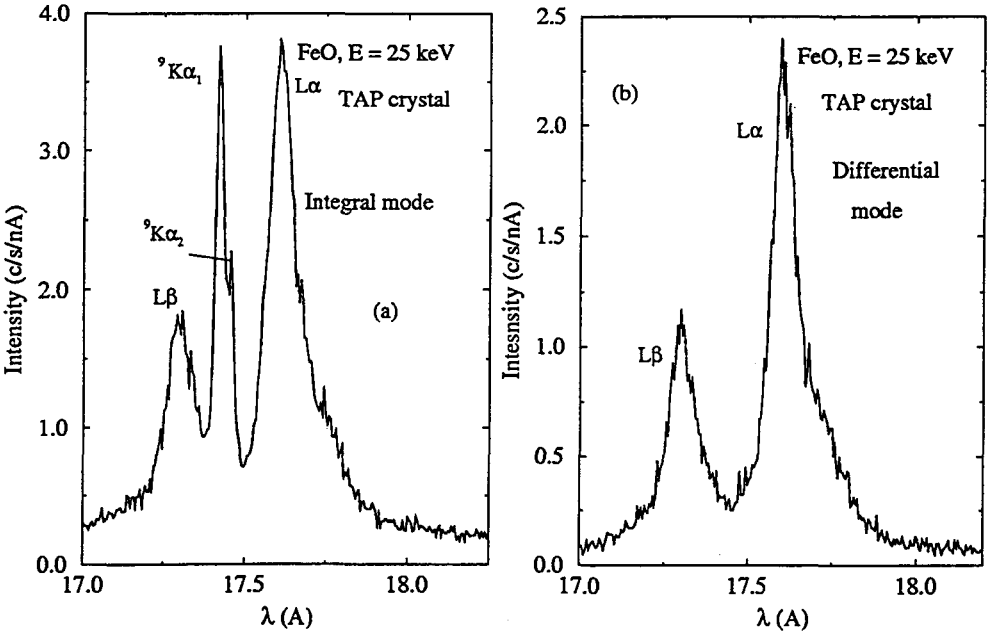

Figure 3.3: Experimental spectra of Fe Lα and Lβ peaks corresponding to FeO recorded with the following PHA settings: (a) integral mode (b) differential mode.

The most common experimental uncertainties, apart from statistical ones, associated with a WDS are related to performance and changes in the geometry of the arrangement. During the x-ray measurement, the spectrometer must be positioned many times at the top of the different peaks and at background regions, and thus backlash in the spectrometer mechanism is a source of uncertainty. It is thus recommended to approach the different Bragg angles always from the same direction. On the other hand, the focussing geometry of the WDS requires that the x-ray source, the crystal monochromator and the proportional counter must be on the Rowland circle. Usually, the geometry is adjusted in such a way that the x-ray source is at the intersection of the electron optical axis with the plane of the target surface. However, when the point of electron impact is not properly adjusted at the optical focus due, for example, to any topographic feature, a decrease in the measured intensity is produced. Therefore, careful vertical adjustment and good sample polishing of the targets are required.

3.4 The CAMECA SX-50 electron microprobe

In this work, measurements have been carried out on a CAMECA SX50 electron microprobe, equipped with four vertical WDS spectrometers and a Princeton Gamma-Tech, Inc. (PGT) energy dispersive x-ray analysis system. The equipment is available at the Serveis Cientifico-Tècnics of the University of Barcelona.

The SX50 is equipped with an electron absorber column liner tube, which minimizes the scattering of the parasitic electrons on the instrument inner walls. Beam current stability is achieved by means of a continuous beam current monitoring and feedback system. The specimen stage is positioned by means of an optical encoder; ruled glass plates are fixed along the X and Y axes of the specimen stage, and photo-cells fitted to the moving tables of the stage observe the X and Y positions continuously. The microprobe is equipped with two anti-contamination devices, namely, the jet of gas directed at the point of analysis and the cold finger. The accelerating voltage is capable of operating up to 50 kV (nominal), in 0.1 kV steps. The take-off angle is 40°, for both spectrometers. The specimen can be observed by using secondary, backscattered and absorbed electron detectors, as well as by means of an optical microscope with reflected or transmitted light. Microprobe automation is provided by a SUN workstation, running under UNIX, with 32-bit VME-bus hardware.

The WDSs contains the following crystals: LiF, PET, TAP and the LSM W/Si, with two different interatomic spacings, Ni/C and Mo/B_4C. Spectrometer precision is provided for by an optically encoded, totally linear, fully geared direct-drive mechanism, which ensures that the spectrometer moves precisely to the requested x-ray peaks avoiding the use of time wasting peak search routines. Proportional counters are of the gas-flow open type, with counter gas argon-methane (90:10) mixture.

The PGT energy dispersive x-ray system consists of a Si(Li) detector. It is mounted at the end of a cold finger inside a vacuum tube, which also contains the FET, located behind the crystal to ensure low noise and good resolution. The nominal resolution is 136 eV at 5.894 keV, with 1000 counts per second. A 7.5-litre liquid nitrogen dewar keeps the detector cooled. The detector system, shown schematically in Fig. 3.4, includes the electronic pulsed-optical preamplifier. The crystal is biased at -600V, and pulses from the detector are amplified and sent to a multichannel analyzer with 1024 channels. According to the manufacturer's specifications, the Si(Li) crystal is 3 mm thick and has an active area of approximately 12.5 mm^2. The detector has a 7-μm-thick beryllium window and a contact gold layer 0.02 μm thick. The thickness of the Si dead layer is 0.1 μm. With this specifications, the nominal efficiency, calculated using Eq. (3.2), is displayed in Fig. 3.5.

The incident photon beam can be collimated with two diaphragms (300 μm and 1 mm in diameter) placed in front of the detector at 53 mm from the target. The

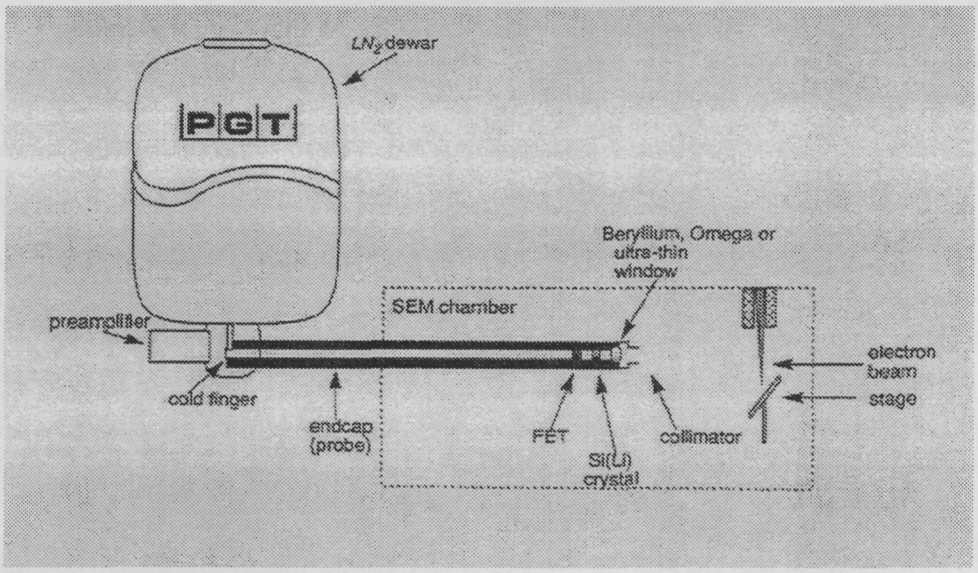

Figure 3.4: Schematic diagram of a basic PGT x-ray detector.

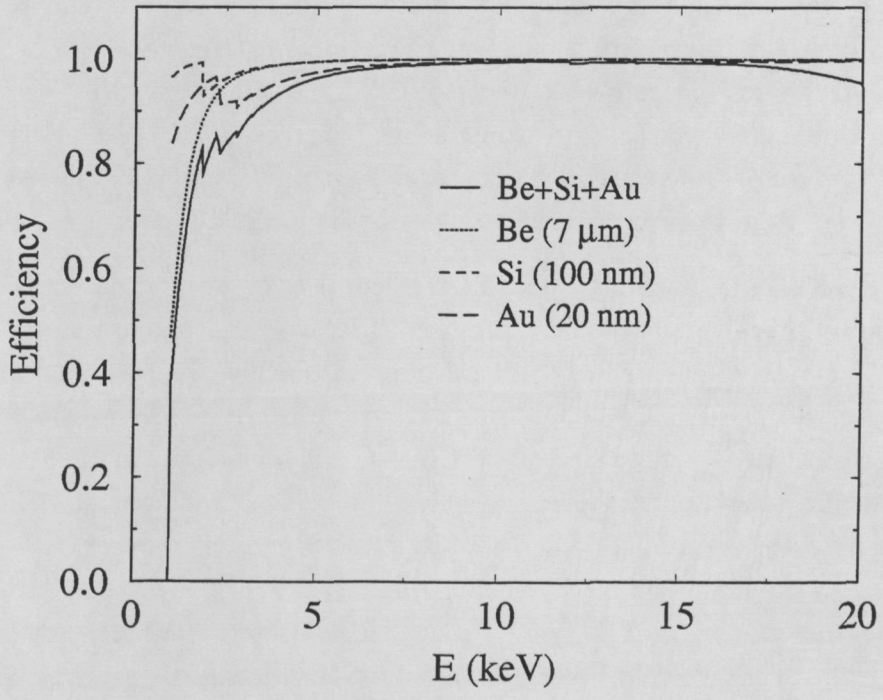

Figure 3.5: Nominal efficiency of the Si(Li) solid state detector, calculated by using Eq. (3.2). MACs have been taken from the PENELOPE data base.

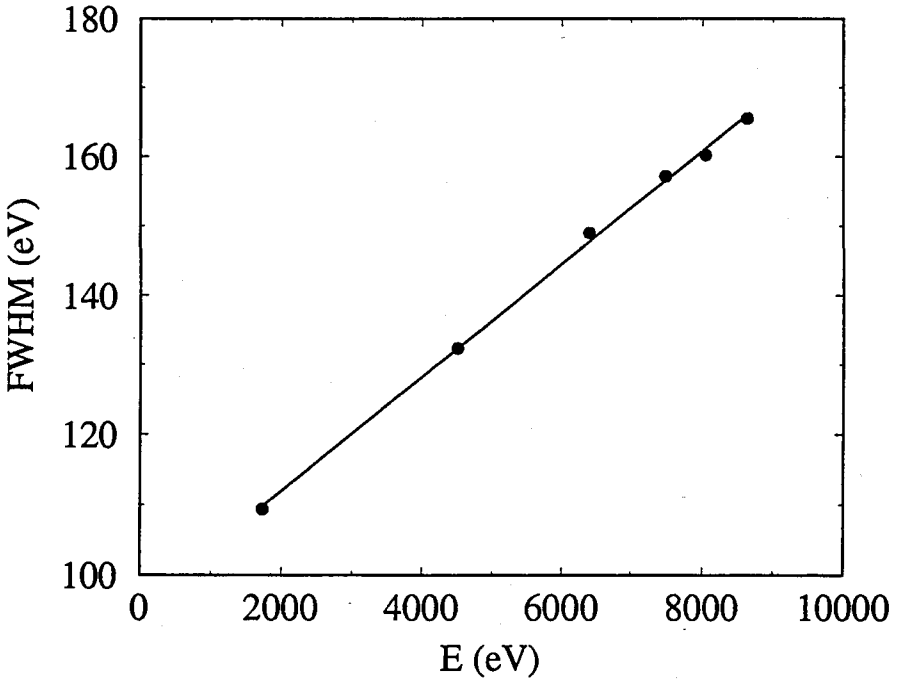

Figure 3.6: Experimental peak widths as functions of the incident x-ray energy for the Si(Li) detector.

detector-target distance is approximately 60 mm. The energy scale is calibrated by measuring, simultaneously well-separated x-ray lines. The resolution as a function of the energy of the incoming x-ray has been determinated by measuring the FWHM of different characteristic x-ray lines on different targets. Experimental values are displayed displayed in Fig. 3.6. Data have been fitted with the function

$$FWHM(E) = \sqrt{a + bE} \tag{3.4}$$

with $a = 7849.25$ eV^2 and $b = 2.23$ eV. These values yielded an electronic noise contribution to the FWHM of 88.5 eV and a Fano factor of 0.10 (see (3.1)), which agree with values reported in the literature (Reimer, 1980).

In Fig. 3.7 two x-ray spectra of InSb recorded with the EDS and the WDS (PET crystal) are compared. We see that in the EDS spectra, the overlap between adjacent lines makes it difficult to obtain the corresponding x-ray intensities. On the contrary, in the spectra recorded with the WDS, the majority of x-ray lines are clearly resolved. The spectral resolution also has an influence on the peak-to-background ratio. A poor resolution may completely hide x-ray lines of elements that are present in very low concentrations. Because of its better resolution, WDS has better (lower) detection limits than EDS (typically ten times).

In the measurements done in this work, the exactness of the accelerating voltage has been checked by inspection in the high-energy cut-off in the EDS spectrum. We have also systematically checked the beam current stability, at the beginning of each

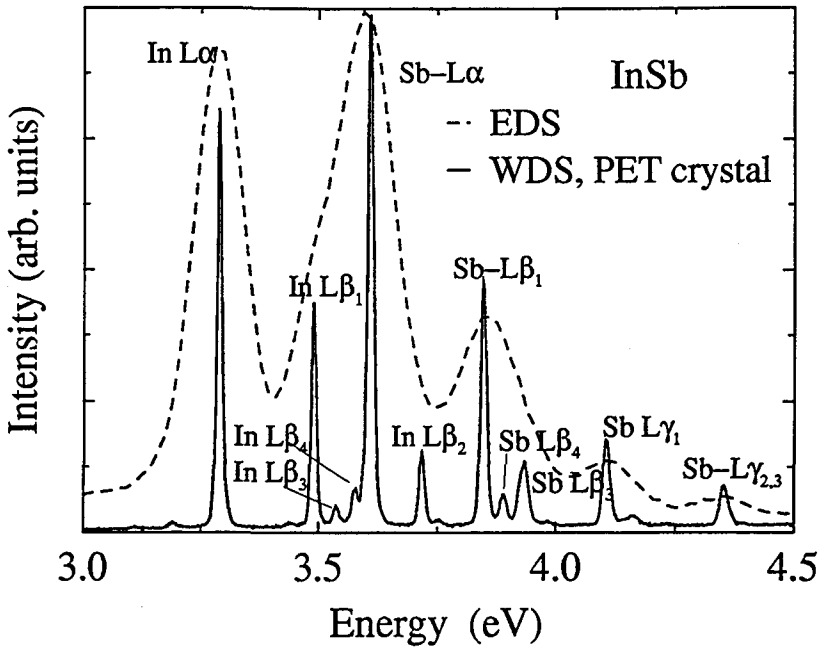

Figure 3.7: Experimental x-ray spectra of InSb obtained with an EDS and a WDS, using a PET crystal.

session, by reading its value during a time interval of the order of $\sim$ 30-45 minutes. We have found the stability was normally better than 0.3%. The current stability has also been checked after varying the accelerating voltage. In these cases, the electron current normally became stable very rapidly.

3.5 Statistical uncertainties of x-ray measurements

Results of x-ray detection obey Poisson statistics. This means that if the number of detected counts is N, the variance σ^2 is N and the standard deviation σ is $N^{1/2}$. The relative standard error ϵ, defined by σ/N is therefore $N^{-1/2}$. If the N counts are measured during time t, i.e. the counting rate is $I = N/t$, then the standard deviation of the count rate is $N^{1/2}/t$.

The measurement of x-ray intensities involves the measurement of the count rates of the peak (I_p) and background (I_b). The net count rate is simply obtained by $I_\mathrm{p} - I_\mathrm{b}$. The variance of the net count rate is given by the sum of the variances of the total peak and background count rates, namely $\sigma^2_{\mathrm{p-b}} = \sigma^2_\mathrm{p} + \sigma^2_\mathrm{b}$. Therefore, the standard deviation is

$$\sigma_{\mathrm{p-b}} = \sqrt{\frac{N_\mathrm{p}}{t^2_\mathrm{p}} + \frac{N_\mathrm{b}}{t^2_\mathrm{b}}}, \tag{3.5}$$

where N_p and N_b are the counts detected in the peak and background during the time intervals t_p and t_b respectively, and consequently the relative standard error will be

$$\epsilon_{p-b} = \sqrt{\frac{N_p}{t_p^2} + \frac{N_b}{t_b^2}} \left(\frac{N_p}{t_p} - \frac{N_b}{t_b} \right)^{-1} . \tag{3.6}$$

The variance of the ratio of two x-ray count rates, is also given by the sum of their corresponding variances.

Chapter 4

Measurement of K-shell ionization cross sections

The cross section for inner-shell ionization by electron impact is one of the basic parameters needed for quantitative procedures in EPMA and AES, as well as for a wide range of applications in other fields. Ionization cross sections can be measured either by counting the number of characteristic x-rays or Auger electrons which are emitted in the de-excitation of ionized atoms or by properly interpreting energy-loss spectra of electrons transmitted through thin films. A detailed review of the various measurement methods has been given by Powell (1985). Cross section values for K-shell ionization derived from experimental measurements have been recently compiled by Long et al. (1990). This compilation clearly reveals that experimental data are scarce and are affected by considerable uncertainties (see below). For outer shells, the situation is even worse: the available amount of data is much smaller and typical uncertainties are larger (because of the lack of knowledge of the corresponding fluorescence yields).

In the present chapter we describe new measurements of K-shell ionization cross sections for several elements, obtained by counting characteristic x-rays emitted from extremely thin, self-supported films bombarded by kilovolt electrons with our SX50 electron microprobe. Special emphasis has been laid on measuring, as accurately as possible, the energy dependence of σ_K as a function of the electron incident energy. The reason is that, for EPMA, quantification procedures are usually based on x-ray intensity ratios, and this means that what really matters is the shape of the $\sigma_K(E)$ curve (i.e. the relative variation of the ionization cross section with electron energy), rather than the absolute magnitude. To minimize statistical uncertainties in the x-ray measurement, especially near the ionization threshold, we have used the wavelength-dispersive spectrometer.

Our aim was twofold. Firstly, to establish and check the methodology for systematic measurement of ionization cross sections with the electron microprobe, and secondly,

to apply it to measurement of K-shell ionization cross sections of several elements in order to validate the theoretical approach (optical-data model) that we shall use in the simulations. The selected elements have intermediate atomic numbers, with x-ray energies in a region where uncertainties related with detection efficiency are minimal.

4.1 Experimental determination of K-shell ionization cross sections

K-shell ionization cross sections σ_K can be obtained by measuring the number of characteristic x-rays (N_{K_α}) emitted from a thin, self-supported material layer of thickness t, bombarded with N_e electrons of energy E (at normal incidence). The K-shell ionization cross section can be expressed as (see e.g. Shima et al., 1981)

$$\sigma_K(E) = \frac{1}{\omega_K} \frac{I(\alpha)+I(\beta)}{I(\alpha)} \frac{4\pi}{\mathcal{N}\, t\, N_e\, \epsilon\, \Delta\Omega} N_{K\alpha}(E), \tag{4.1}$$

where $I(\alpha)$ and $I(\beta)$ are the line fractions of the $K\alpha$ and $K\beta$ peaks, $N_{K\alpha}(E)$ is the number of detected characteristic Kα x-rays, $\mathcal{N}$ is the atomic target density (atoms per unit volume), ω_K is the fluorescent yield, $\Delta\Omega$ is the solid angle subtended by the spectrometer and ϵ is the spectrometer efficiency. Therefore,

$$\sigma_K(E) = C\, N_{K_\alpha}(E), \tag{4.2}$$

where

$$C = \frac{1}{\omega_K} \frac{I(\alpha)+I(\beta)}{I(\alpha)} \frac{4\pi}{\mathcal{N}\, t\, N_e\, \epsilon\, \Delta\Omega} \tag{4.3}$$

is an energy-independent scaling factor. For a given electron kinetic energy E, σ_K is proportional to the measured x-ray intensity N_{K_α} and thus the energy dependence of the ionization cross section is simply given by $N_{K_\alpha}(E)$.

4.1.1 Sample preparation

Irradiated targets must be homogeneous and thin enough to ensure that 1) the energy loss ΔE of incident electrons must be relatively small, i.e. $\Delta E \ll E$ and, 2) electron scattering within the sample does not alter the direction of movement appreciably, i.e. incident electrons penetrate straight through the film.

To obtain a rough estimate of the error induced by the energy loss of electrons, we can consider that it reduces the mean incident energy to $E - \Delta E/2$ (see e.g. Shima et al., 1981). The overvoltage $U = E/E_i$ is therefore affected by an uncertainty of $\pm(\Delta E/2)/E_i$. For example, if we consider electrons with 10 keV of incident energy

impinging on 5 μg/cm^2-thick Ni target, and assume that the energy loss can be taken to be equal to $-(\mathrm{d}E/\mathrm{d}s)\Delta s$, where $\mathrm{d}E/\mathrm{d}s$ is the stopping power and Δs is the layer thickness, then $(\Delta E/2) \sim 38$ eV, since in this case $\mathrm{d}E/\mathrm{d}s \sim 15$ eV cm^2/μg. This means that the uncertainty in E is about 0.4%. However, if the film is 50 μg/cm^2 thick, then $(\Delta E/2) \sim 375$ eV, which represents an error of about 4%.

The preparation of such "ideal" films is difficult in practice and requires great experimental ingenuity. For this reason, other kind of samples have been used, e.g. by Luo et al. (1996). These authors employed thin films deposited on thick subtrates, which are easier to prepare, and substracted the x-ray contribution from electrons that are reflected from the substrate. However, this contribution must be calculated by solving the transport equation or by Monte Carlo simulation, and the resulting ionization cross sections can be strongly influenced by the accuracy of these calculations. Related to this, we may indicate that, during a period of one year, the same group of authors have published experimental results for the same element differing in more than 30% (Luo et al., 1996; He et al., 1997).

The samples were prepared at the microprobe laboratory of the University of Montpellier II (France). Self-supported films of chromium, nickel and copper were produced by thermal evaporation as follows. Firstly, carbon films of approximately 30 nm were thermally evaporated on films of mica; because of its low atomic number and large tensile strength, carbon films are adequate to hold the Cr, Ni and Cu films. The mica films were separated from the carbon ones in distilled water; carbon films floating on the water surface were picked up with a grid of the kind used in transmission electron microscopy; in some cases we also used synthetic organic grids. The grids, covered with the carbon film were placed on the holes (of a slightly lower diameter than the grids) of a 1-inch diameter disk, which fits into the specimen holder.

Cr, Ni and Cu films were deposited by thermal evaporation on the previously prepared self-supported carbon films. For Ni and Cu, equivalent films were deposited on polished thick ultra-pure GaAs targets, during the same evaporation runs. The latter samples were used for thickness determination by electron microprobe measurements (see below). The substrates of GaAs were chosen owing to the similar mean atomic number to the evaporated films, which is useful to obtain accurate thickness measurements (see below) and also due to their high purity. Figs. 4.1 shows a photograph of one of the targets used, containing the self-supported films, and fig 4.2 shows electron micrographs of two different Ni self-supported layers, respectively. We can see that the grids are squares of approximately 200 μm.

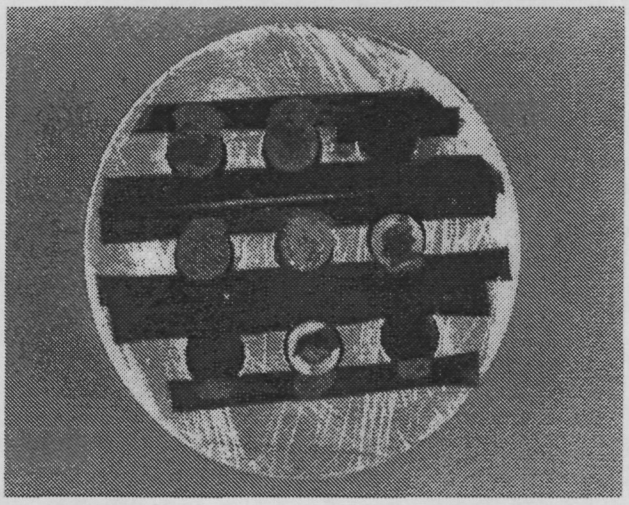

Figure 4.1: Photograph of one of the targets containing the self-supported films.

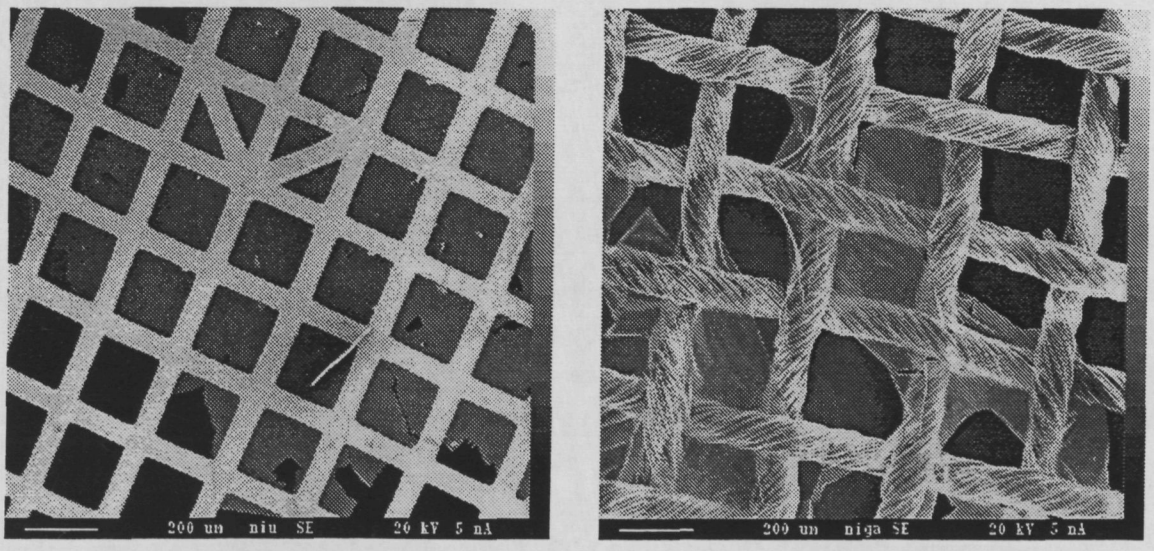

Figure 4.2: Scanning electron micrographs of Ni films deposited on different grids, namely, one typically used for TEM studies (a) and one made of a synthetic weave (b). The deposited layer areas are the medium grey areas. In the black regions, the film was not attached.

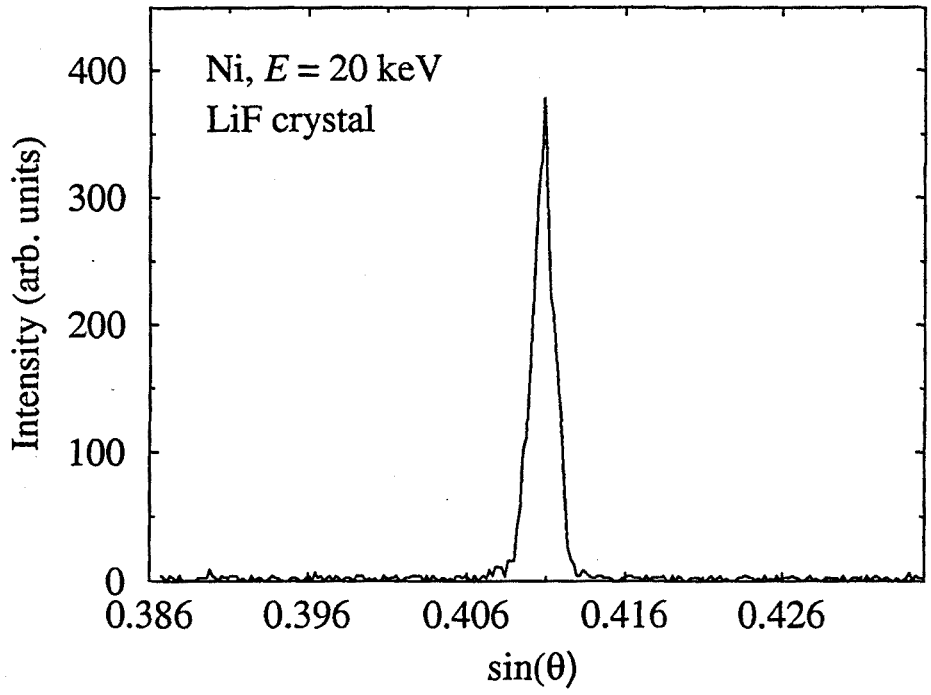

Figure 4.3: Experimental wavelength dispersive x-ray spectrum of the Ni self-supported film.

4.1.2 Relative measurements

To obtain the shape of the ionization cross section, x-ray measurements were carried out using the WDSs on the electron microprobe, from the excitation energy up to 40 keV. Measurements were performed at the wavelength channel corresponding to the maximum of the peak, using the LiF (for Ni, Cu and Cr), PET (for Cr) crystals. For each beam energy and sample, at least 10 measurements at different target positions were performed. Therefore, the standard deviation of these measurements not only includes the statistical errors, but also the errors due to the possible variations in thickness of the sample. Counting times were about 100 seconds for each peak and 50 seconds for the background. Electron currents were selected to give a certain compromise between x-ray counting rate and film damage, with typical values from 40-80 nA. Bremsstrahlung background was subtracted by linear interpolation of the spectral background at both sides of the characteristic peak. A typical WDS spectrum of the Ni unsupported film, irradiated with 20 kV electrons is shown in Fig. 4.3.

Relative uncertainties due to counting statistics, sample non-uniformity and background subtraction, for an incident energy near the maximum of the ionization cross section curve are estimated to be ~3%.

4.1.3 Absolute measurements

Conversion from measured x-ray intensities to absolute ionization cross section requires knowledge of the parameters involved in Eq. (4.1), i.e. film thicknesses, fluorescence yields, line fractions, number of incoming electrons, detector efficiency and detection solid angle. In the following we describe the procedures used to determine these parameters. Only the ionization cross sections for Ni and Cu were considered.

Film thicknesses were obtained by measuring the ratio of intensities (k-ratio) of the Ni/GaAs and Cu/GaAs targets to the intensity measured on pure Ni and Cu standards. Because of the very small layer thicknesses, and to minimize secondary fluorescence contribution, Lα lines were used. k-ratios were measured from 2 keV up to 25 keV, for the Cu Lα and Ni Lα lines, and for Ga Lα and As Lα. It is worth noticing that measurement of the substrate is not strictly necessary (see chapter 5), but it helps to check the consistency of the results. For each sample and each energy, at least five measurements were performed. Acquisition times and beam currents were choosen so as to ensure that the statistical uncertainty (2σ) for the overlayer element is less than 3%. Background was estimated by simple linear interpolation between measurements at both sides of the corresponding peak. Pure standards, freshly polished, for Ni and Cu were used. For Ga and As, the standard was a piece of the same block used as substrate. To avoid carbon contamination, the oxygen jet was operating during measurements of both targets and standards.

Measured k-ratios were analyzed with the help of the commercial program X-FILM (Merlet, 1995). This program calculates the thickness and concentration of a multilayer target by least squares fitting of an analytical x-ray emission model to the experimental data. Results with the corresponding errors are reported in Table 4.1. The agreement between the analytical model and the experimental k-ratios is graphically shown in Fig. 4.4. For the Cu/GaAs target, the agreement is found to be very good, whilst for Ni/GaAs, differences of about 5% are found at very low energy for Ni. These differences could be attributed, on the one hand, to sample contamination (oxide or carbon layers, both in the standard and in the sample) and, on the other hand, to the uncertainty of the MACs and other parameters adopted in Merlet's model. Notice that, although the layer is very thin, auto-absorption in the (bulk) standard is high and the uncertainty in the MACs largely affects the result, especially in the case of Ni Lα lines (see e.g. Pouchou, 1996). The accuracy of the MACs used was carefully checked by comparison of the emerging x-ray intensity from pure bulk Ni to the theoretical model, giving satisfactory results within the experimental error as shown in Fig. 4.5. Therefore, it seems that the obtained differences can be mainly attributed to sample contamination.

It should be stressed that when the atomic numbers of the layer and substrate are close, the depth distribution of ionizations in the film material is accurately described by using the corresponding part of the ionization-distribution in the bulk material, which

Table 4.1: Results of film mass thickness (ρt) estimation for the systems Ni/GaAs and Cu/GaAs, using the Merlet's program X-FILM. The actual concentration of GaAs is 0.482%wt of Ga and 0.518 %wt and As.

System	ρt (μg/cm^2)	Ga (% wt)	As (% wt)
Cu/GaAs	3.50 $\pm$ 0.07	0.483 $\pm$ 0.007	0.516 $\pm$ 0.007
Ni/GaAs	6.6 $\pm$ 0.4	0.48 $\pm$ 0.01	0.5150 $\pm$ 0.007

seems to be relatively well known. Therefore, the accuracy of the thickness estimation by using the above-mentioned program is expected to be less than 5%. The estimated film thicknesses were found to range from 3.5-6.6 μg/cm^2, which ensures that electrons will lose a negligible fraction of their energy inside the sample.

In order to verify that incident electrons traverse the film following essentially straight trajectories, we have used PENELOPE to evaluate their mean track length. In the simulations, the absorption energy E_{abs} was set equal to the ionization energy of the considered shell. It has been found that differences between the real film thickness and the mean track length of transmitted electrons are less than 3% for the films of interest. Another problem regarding thickness estimation is that the unsupported films are not completely flat due to some wrinkling. This means that actually the film thickness is $t/\cos\theta$, where θ is the wrinkle angle and t is the theoretical thickness. Moreover, the wrinkling varies as the beam strikes the film, i.e. the film is bent by the impact of electrons, therefore the associated error, which is random at the beginning of the measurement, becomes more and more systematic as the measurement progresses. Bearing this in mind, uncertainties in the thickness evaluation are estimated to be of the order of 10%. This was found to be the largest contribution to the error in the absolute cross section measurement. Further work to improve the thickness estimation is in progress.

The number of incident electrons N_e was evaluated by multiplying the target current I_0 by the acquisition time t. Probe currents were measured with a Faraday cup placed on the sample holder. The calculated number of incident electrons is estimated to have less than 2% uncertainty. Fluorescence yields were taken from the tabulation of Fink and Rao (1974) and Khan and Karimi (1980), which are reported in Table 4.2. The uncertainty is estimated to be less than 2%.

Table 4.2: Values of the fluorescence yield ω_K and line fraction used in this work.

Element	ω_K	$[I(\alpha)+I(\beta)]/I(\alpha)$
Ni	0.406	1.136
Cu	0.445	1.137

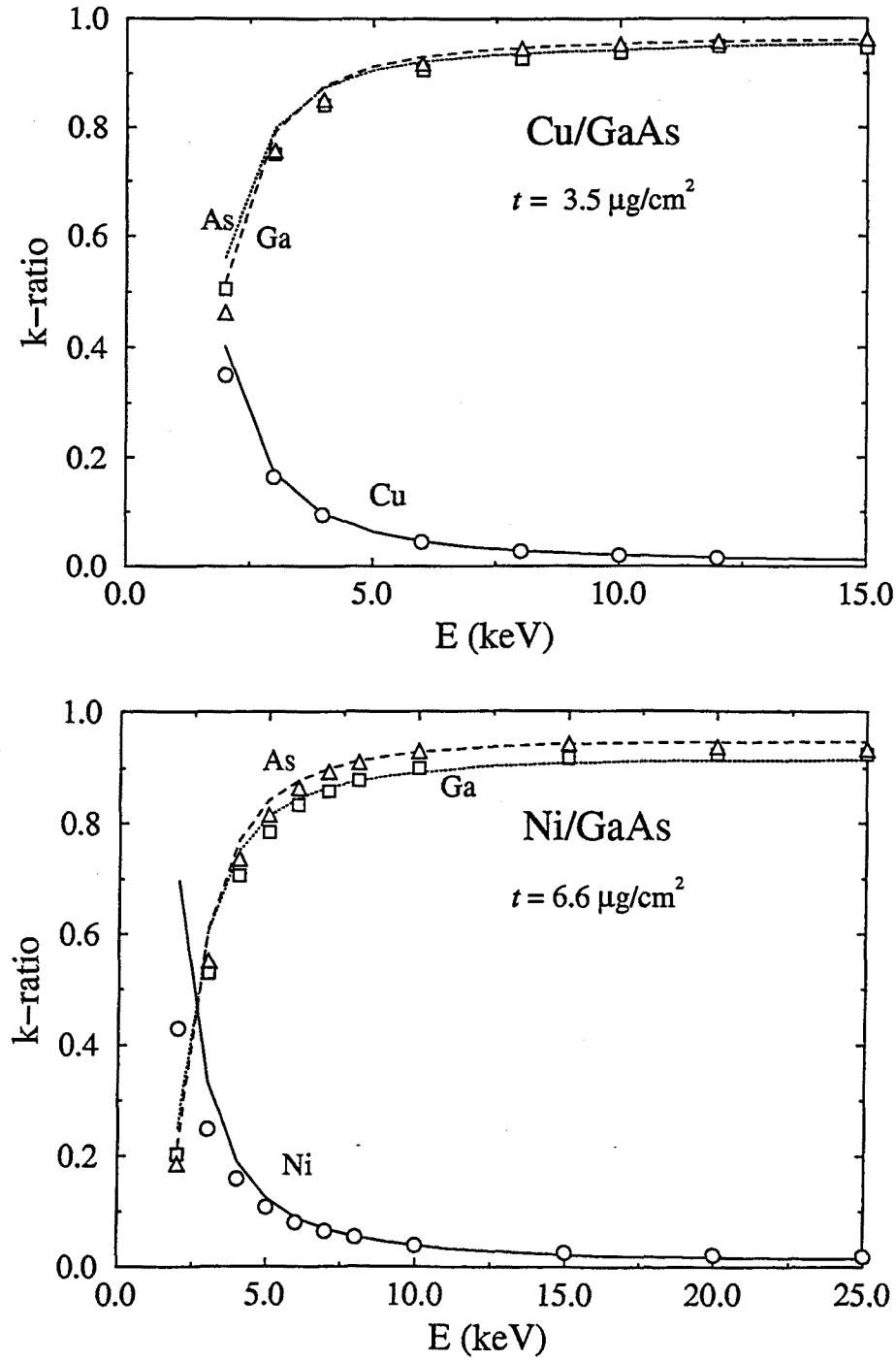

Figure 4.4: K-ratio versus electron incident energy for Cu/GaAs and Ni/GaAs systems. Lines correspond to the analytical results of Merlet's program X-FILM. Symbols represent experimental data.

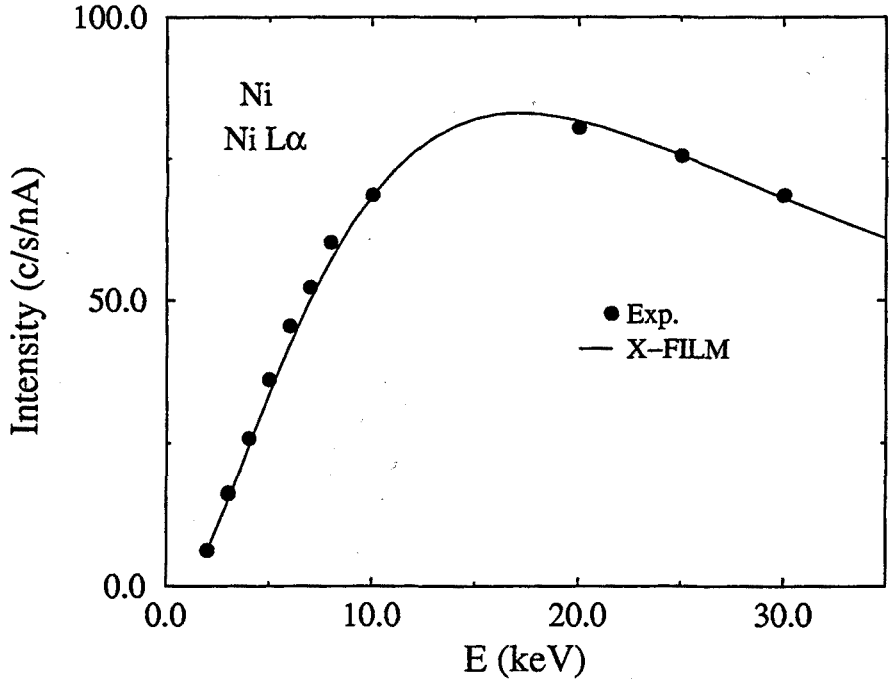

Figure 4.5: Energy dependence of the emerging x-ray intensity for the Ni Lα line in pure Ni. Circles are experimental measurements. The continuous line is the theoretical prediction of X-FILM (Merlet, 1995).

As mentioned previously, it is difficult to determine the efficiency of a WDS. On the other hand, the efficiency of the EDS in the energy range of interest, say 6-8 keV, and the solid angle of collection can be obtained by relatively simple methods (see section 3.2). For the present purpose, this efficiency was considered to be unity at the photon energies of interest and the detection solid angle was calculated by geometrical considerations. Uncertainties in the determination of both the efficiency and detection solid angle are about 5%.

Using the EDS, x-ray intensities emitted by the thin self-supporting films were measured and converted to ionization cross section values by means of Eq. (4.1), using the previously determined parameters. The values of the ionization cross section calculated were used to re-scale the relative x-ray intensity curves obtained with the WDS and to obtain the ionization cross section curves in absolute units. In principle, to re-scale each relative curve, only one value of $\sigma_K(E)$ must be known. However, to reduce errors in the scaling procedure, we have determined the mean scaling factor for different electron energies, all of which are above the maximum of the curve (see Fig. 4.8-4.9). Values of the obtained scaling factors, x-ray intensities and calculated cross sections, for Ni and Cu, are shown in Tables 4.3 and 4.4.

Long measurement times were used (about 4000 seconds per spectra), which ensured that the statistical uncertainty of the x-ray intensities is less than 2%, with beam cur-

Table 4.3: Absolute cross sections, x-ray yield I_{WDS}, and scaling factor, $C = \sigma_K / I_{WDS}$, for Cu. The mean value of the scaling factor is 191.1, with an accuracy of ± 2.6 %

Cu			
Energy (keV)	σ_K (barns)	I_{WDS} (counts/sec/nA)	C (barns sec nA/counts)
15	306	1.55	196.7
20	364	1.96	185.2
25	397	2.10	189.2
30	408	2.11	193.2

Table 4.4: Absolute cross sections, x-ray yield and scaling factor, $C = \sigma_K / I_{WDS}$, for Ni. The mean value of the scaling factor is 164.1, with an accuracy of ±3.0 %

Ni			
Energy (keV)	σ_K (barns)	I_{WDS} (counts/sec/nA)	C (barns sec nA/counts)
15	284	1.80	156.8
20	367	2.16	169.6
25	384	2.29	166.6
30	385	2.31	165.9

rents chosen to yield dead times lower than 1%-2%. X-ray intensities were obtained by measuring the area of the corresponding peak. Background was substracted by using a polynomial fit.

Unfortunately, x-ray spectra recorded from self-supported films using the EDS showed spurious peaks. The origin of these peaks can be mainly attributed to the interaction of electrons with the specimen chamber and the supporting grid, as it usually happens in the TEM (see e.g. Nicholson and McKenzie, 1998). The latter possibility is not very likely in the electron microprobe, owing to the existence of an electron absorber tube in the column (see chapter 3). It is worth stressing that stray radiation is not normally recorded with the WDS, owing to the small solid angle of collection and focussing geometry.

Several strategies were followed to overcome this difficulty. To disregard radiation coming from the metallic grid, we have used grids made of synthetic weaves to support the films (see Fig. 4.2). Initiallly, runs were made masking the target with a carbon coated plastic sheet with a small hole at the point of electron impact. Afterwards, it was seen that by placing a small carbon Faraday cup (1 mm-diameter) below the target, aligned to the impact point of incident electrons, most of transmitted electrons were absorbed in the cup. Therefore, this Faraday cup was used every time an x-ray

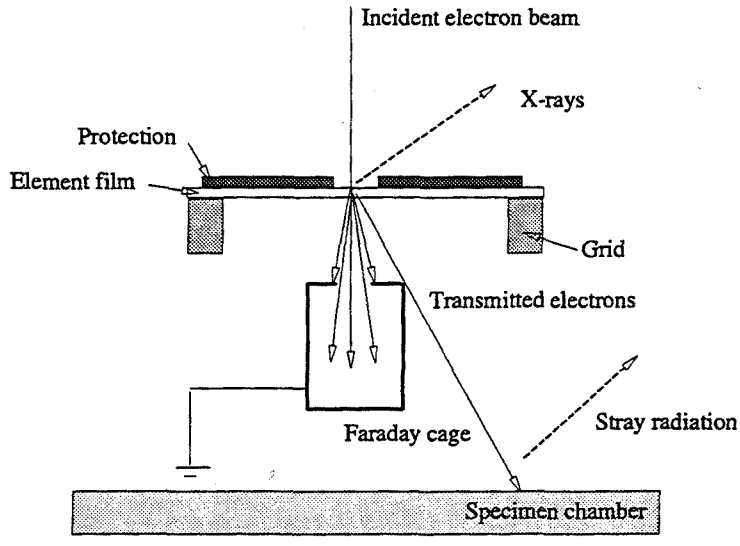

Figure 4.6: Experimental arrangement for measurement of ionization cross sections with the EDS.

spectra was recorded with the EDS. Care was also exercised to focus the electron beam at the point of impact as much as possible. Finally, a 1-mm–thick–tungsten diaphragm was used in front of the detector to minimize the solid angle of collection. Fig 4.6 shows the schematics of the experimental arrangement used for measurement of ionization cross sections with the EDS. In spite of all these efforts, spurious peaks could not be completely suppressed. Fig. 4.7 shows an experimental x-ray spectra of the unsupported Ni film recorded under these conditions.

To make sure that stray radiation does not affect the peaks of interest, x-ray spectra were collected within a "blank" target, i.e. unsupported carbon film with no film attached, at different electron incident energies. These spectra showed no significant peaks at the energies of Ni Kα and Cu Kα. We also tried to determine the bremsstrahlung cross sections from the spectra of self-supported films. However, it seems that the overall background is strongly affected by the spurious contribution, which includes the contribution of the self-supported carbon layer. Indeed, the bremsstrahlung cross section derived from the measured spectra was found to be systematically higher than the theoretical cross section given by Kissel et al. (1983).

4.1.4 Experimental errors

Experimental measurements are affected by two different kinds of errors. The fist kind of errors is due to counting statistics, background subtraction, sample non-uniformity and instrumental drift during x-ray measurement. These errors affect the relative shape

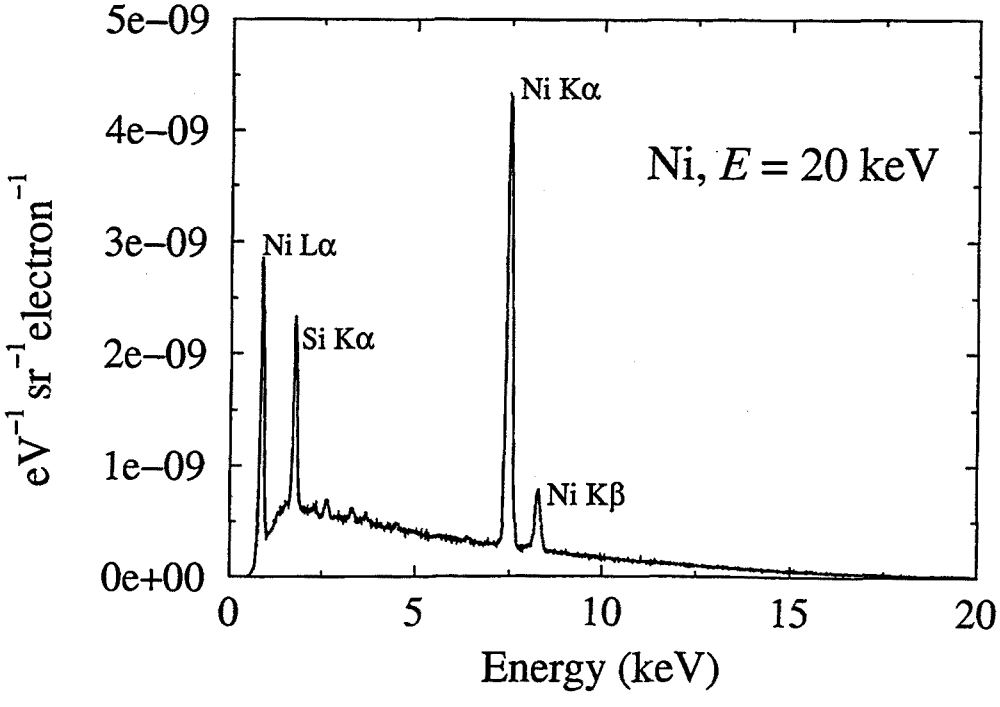

Figure 4.7: Experimental energy dispersive x-ray spectrum of Ni self-supported film, at 20 keV incident electron energy. The small peaks which appear on the right side of Si, are, Cl, K and Ca, respectively.

Table 4.5: Absolute uncertainties of the ionization cross section measurements.

Source	Uncertainty (%)
Counting statistics	± 3
Target thickness	± 10
Detection efficiency	± 5
Beam integration	± 2
Fluorescence yield	± 2
Scaling process	± 3
Quadrature sum	± 12

of the cross section curve, and they are different for each electron incident energy. Relative uncertainties were estimated to be 2%, for a typical point near the maximum of the curve. In the data presented below, the relative uncertainties are plotted at the equivalent of one standard deviation (1σ) for a purely statistical uncertainty.

The second kind of errors, which are systematic, correspond to the conversion to absolute magnitude, namely, the determination of the film thickness, number of incoming electrons, fluorescence yield, line fraction, solid angle of collection and detection efficiency. Furthermore, the error in taking the mean value of the scaling factors evaluated, which unfortunately include again counting statistics from x-ray measurements. These errors were estimated at 10% for target thickness, 5% for detection efficiency and solid angle, 2% for beam integration, 2% for fluorescent yield and line fraction, and 3% for the scaling process. These errors affects in the same way all the points in the curve.

The absolute uncertainty of the measurements is a combination of the relative uncertainties with the systematic errors, combined in quadrature. The vertical scale of the cross section curve varies within the limits given by the absolute uncertainty. This absolute uncertainty will be given as a percentage of the cross section measurement for a typical point near the maximum of the curve. Combining systematic uncertainties in quadrature with the relative uncertainties, gives an absolute uncertainty of approximately 12%. The components of the absolute uncertainty are summarized in Table 4.5.

4.2 Results and discussion

We have compared the energy dependence of the measured cross section with the optical-data model of Mayol-Salvat (1990), and the analytical formulae of Gryzinsky (1966),

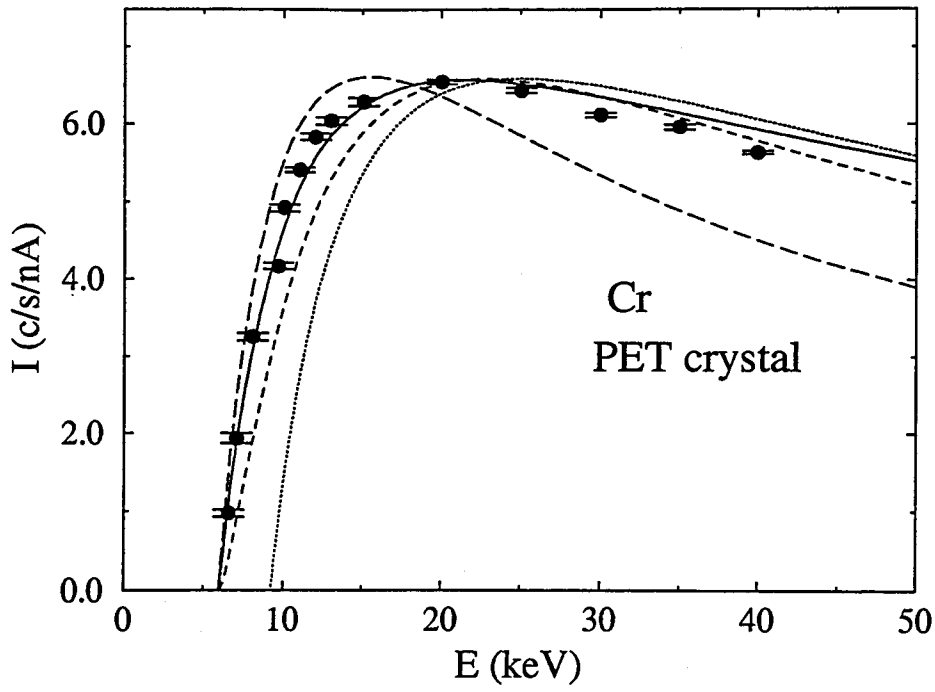

Figure 4.8: Relative comparison of calculated ionization cross sections and experimental x-ray intensities for Cr. The continuous line is the optical-data model of Mayol and Salvat; dotted line, the formula of Bethe-Powell; dashed line, the formula of Gryzinski; long-dashed line, the formula of Worthington-Tomlin. Circles are our experimental measurements.

Bethe-Powell (1976) and Worthington-Tomlin (1956). To this end, first we have re-scaled each calculation curve to its relative maximum and afterwards we have rescaled all the calculations so as to match the maximum in the experimental curve of x-ray intensity vs. electron incident energy. Figs. 4.8-4.9 show the relative comparison of calculation with experiment for Cr, Ni and Cu. We can see that for the three elements measured, the optical-data model is in very good agreement with experiment and provides a better description of the energy dependence of σ_K than the analytical formulas tested. In this respect, it is worth noticing that these analytical formulas depend on the atomic number only through the ionization energy E_K (apart from a change in the scales, the corresponding curves are identical for all elements). Good agreement was also found for other elements using experimental data taken from the compilation of Long et al. (1990).

Figs. 4.10-4.11 compare our measured K-shell ionization cross-sections, in absolute value, for copper and nickel with the optical-data model of Mayol-Salvat (1990), the formulas of Gryzinski (1966), Bethe-Powell (1976) and Worthington-Tomlin (1956), as well as with experimental measurements of other authors.

In Fig. 4.10, measured data for copper are compared with the experimental results given by Shima (1980), Shima et al. (1981), Davis et al. (1972) and He et al. (1997). It seems that our results are in good agreement with measurements of Shima (1980), Shima et al. (1981) and He et al. (1997). Results of Davis et al. (1972) are shown to

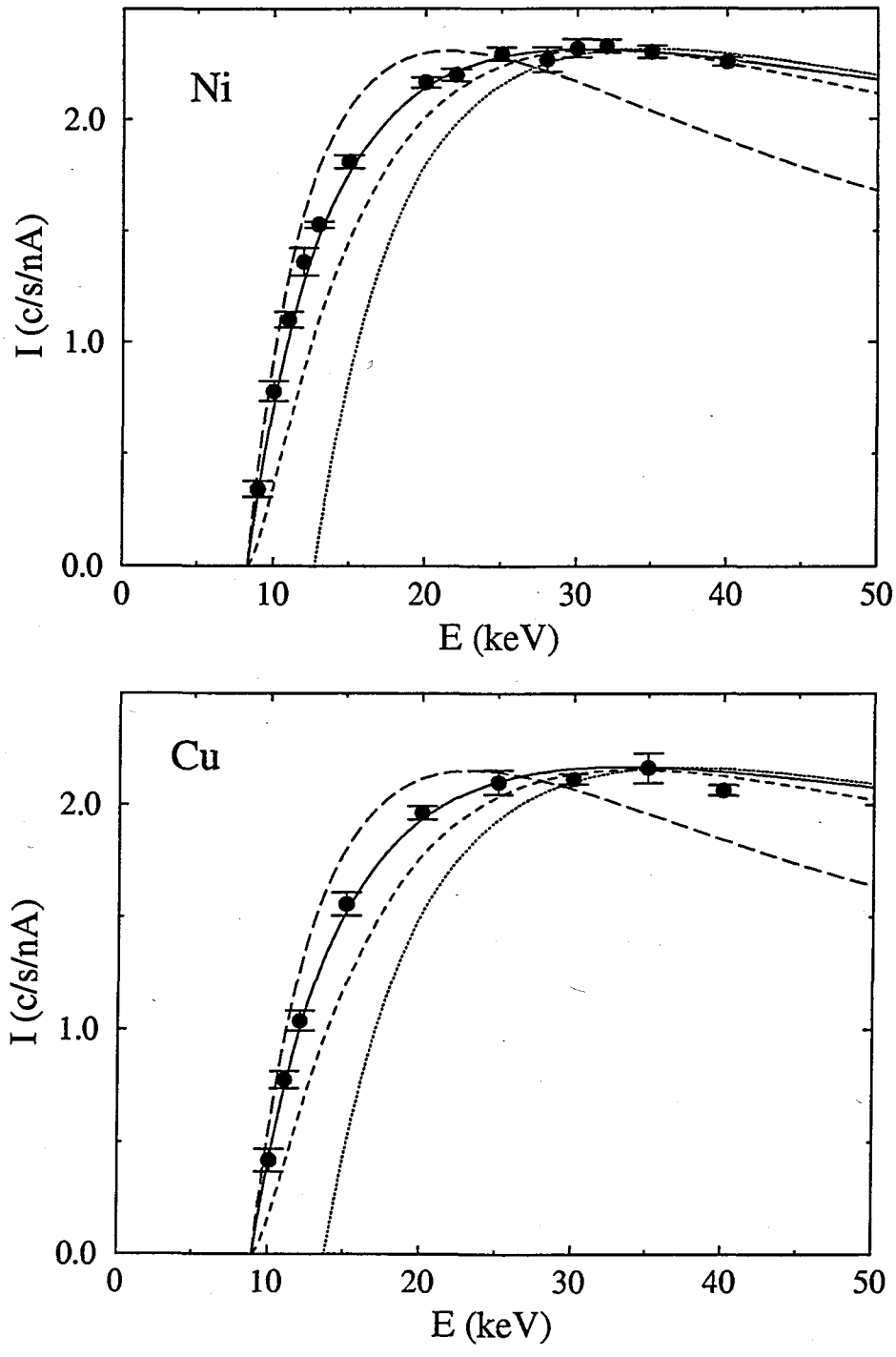

Figure 4.9: Relative comparison of calculated ionization cross-sections and experimental x-ray intensities for Ni (a) and Cu (b). The continuous line is the optical-data model of Mayol and Salvat; dotted line, the formula of Bethe-Powell; dashed line, the formula of Gryzinski; long-dashed line, the formula of Worthington-Tomlin. Circles are our experimental measurements

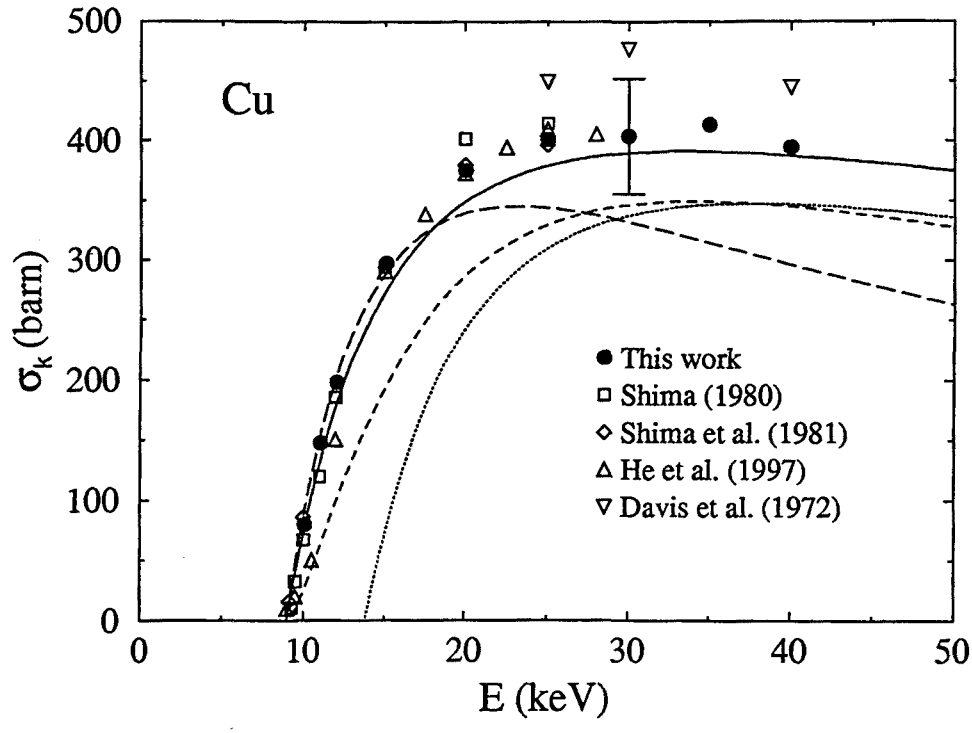

Figure 4.10: K-shell ionization cross section versus electron energy for copper. Continuous line is the optical-data model of Mayol and Salvat; dotted line, the formula of Bethe-Powell; dashed line, formula of Gryzinsky; long dashed line, formula of Worthington–Tomlin; filled circles are experimental measurements in the present work; squares, measurement by Shima (1980); diamonds, measurements by Shima (1981); upright triangles, measurements by He et al. (1997); inverted triangles, measurements by Davis et al. (1972).

be slighty higher than the rest of experimental data. In Fig. 4.11, measured data for nickel are compared with experimental results of Pockman et al. (1947), Jessenberg and Hink (1975), Luo et al. (1996) and He et al. (1997). Our results seem to agree with the experiments of Pockman et al. (1947) and He et al. (1997). On the contrary, results of Jessenberg and Hink (1975) and Luo et al. (1996) are systematically higher than the rest of measurements.

Owing to the uncertainties of measured data, mainly due to the estimation of the film thicknesses, it is difficult to draw a definite conclusion about the accuracy of the various cross sections in absolute terms. In spite of this, the good agrement of our measurements with the predictions of the optical-data model, as regards the energy dependence of σ_K, is very encouraging. As the physical contents of the optical-data model is sound, we shall assume that it yields the best estimates for σ_K. Consequently, in the simulations described in the next chapters, we shall mostly use this theoretical cross section.

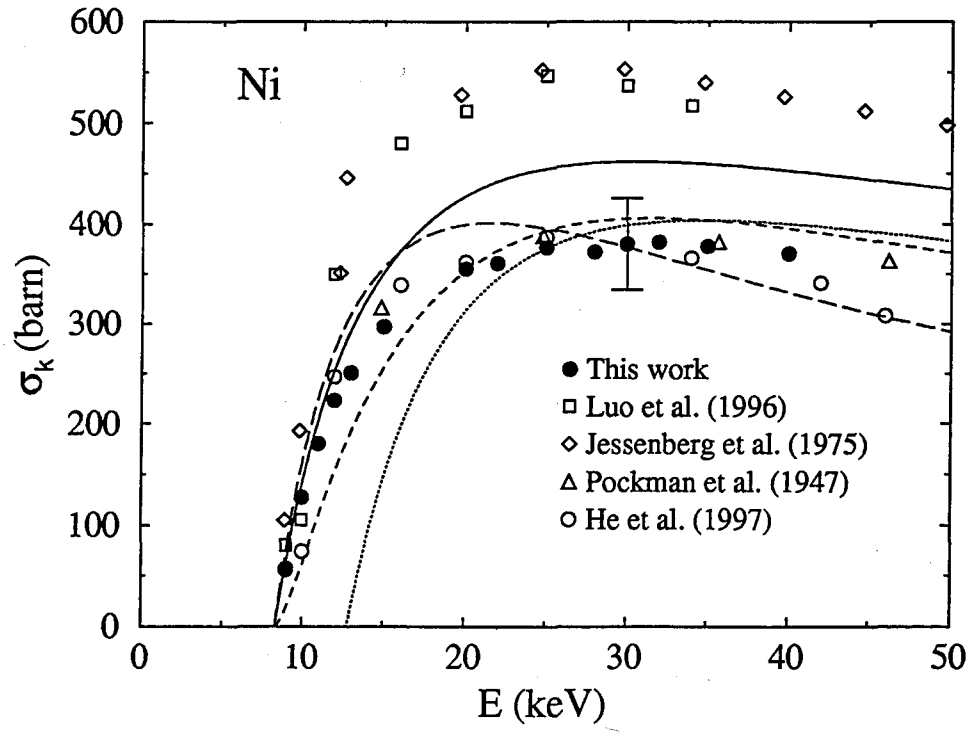

Figure 4.11: K-shell ionization cross section versus electron energy for nickel. Continuous line is the optical-data model of Mayol and Salvat; dotted line, formula of Bethe-Powell; dashed line, formula of Gryzinsky; long dashed line, formula of Worthington–Tomlin; filled circles are experimental measurements of the present work; squares, measurements by Luo (1996); diamonds, measurements by Jessenberg and Hink (1975); upright triangles, measurements by Pockman et al. (1947); open circles, measurements by He et al. (1997).

Chapter 5

Depth distribution of ionizations

The spatial distribution of ionizations caused by electrons impinging on the specimen is the primary quantity for quantitative EPMA. For homogeneous samples and electron beams at normal incidence, this distribution is conventionally described by means of the $\Phi(\rho z)$ function, which is proportional to the density of ionizations per unit mass depth ρz.

The first measurements of the $\Phi(\rho z)$ function were performed by Castaing and Descamps (1955), using the so-called tracer method. The procedure consists of measuring the x-ray intensity from a very thin layer of a pure element (tracer), immersed at different depths in a homogeneous material (matrix). After Castaing's work, measurements of the $\Phi(\rho z)$ for different tracers, matrices and beam energies have been reported (see e.g. Karduck and Rehbach, 1991). From the practical point of view, these measurements are useful to derive simple empirical analytical formulas for $\Phi(\rho z)$, usually defined by a few parameters, which are employed in practical quantification algorithms (see e.g. Merlet, 1998a and references therein).

As experimental data are available only for a limited range of materials and experimental conditions, theoretical calculations, particularly MC simulations, are of great help to determine ionization distributions. MC simulations have been occasionally used for the systematic calculation of the $\Phi(\rho z)$ function and related quantities (see e.g. Ichimura and Shimizu, 1981). Earlier simulations, based on simple scattering models, were found to differ too much from experimental data (see e.g. Love et al. 1977). Reimer and Krefting (1976) were the first to realize that $\Phi(\rho z)$ distributions obtained from MC simulation were strongly dependent on the adopted scattering model. More recent MC simulation work using a variety of scattering models (Murata et al. 1983; Karduck and Rehbach, 1988; Hénoc and Maurice, 1991; Kotera et al. 1992; Ding and Wu, 1993; Bakaleinikov and Tretyakov, 1995; Murata et al. 1995) has led to improved agreement with experiments. In some cases, simulations and experiments do not agree satisfactorily, although it is known that experimental data may be in error because of

the use of tracer layers that are too thick (Karduck and Rehbach, 1988). The situation is more confusing in the case of inhomogeneous samples (e.g. thin layers on substrates or multilayered structures) or special geometries (e.g. oblique incidence), where experimental measurements are very rare. Here, there is a real need for experimental data to check the reliability of simulations and/or alternative approximate formulations.

Measurement of the surface ionization $\Phi(0)$ is the first step in any attempt to obtain the complete depth distribution of ionizations. The single quantitty $\Phi(0)$ is an excellent global test for any calculation method, because it is sensitive to elastic and inelastic scattering and to the adopted inner-shell ionization cross section. From the practical point of view, the surface ionization is of great importance because it appears explicitly in all established parameterizations of $\Phi(\rho z)$ for EPMA quantification. On the other hand, this same quantity, usually referred to as R factor, describes the reinforcement of the Auger signal by backscattered electrons, and it is required in quantitative AES (see e.g. Cazaux, 1992).

In this chapter, we consider the simulation and measurement of ionization distributions. For homogeneous targets we compare our simulation results with experimental data taken from the literature. In order to assess the reliability of the simulation for non-homogeneous samples, we have performed systematic measurements of the surface ionization for thin films deposited on different substrates. On the basis of these measurements we study the variation of the surface ionization with the atomic number of the substrate and the energy. The purpose of the present chapter is twofold: 1) to provide convincing evidence of the fact that PENELOPE, combined with realistic ionization cross sections, yields results that are sufficiently accurate for practical purposes, and 2) to report new experimental data of the surface ionization for thin films on substrates.

The chapter is structured as follows. After introducing the concept of the $\Phi(\rho z)$ function, we describe the simulation procedure that we have developed to calculate this function. In section 5.3, we present benchmark comparisons of simulation results with experimental data taken from the literature. In section 5.4, we describe the experimental procedure used to measure the surface ionization and we offer a comparison between simulation results and experimental data. Finally, the simulation program is used to investigate ionization distributions for thin films on substrates.

5.1 Theoretical background

Let us consider a homogeneous target of a given composition. In the general case of compounds, the molecular weight is given by $A_{\mathrm{M}} = \sum a_i A_i$, where a_i is the number of atoms per molecule of element i with atomic number Z_i and atomic weight A_i. The

concentration of element i can be given in terms of the mass fraction

$$c_i = \frac{a_i A_i}{\sum_j a_j A_j}. \tag{5.1}$$

The number of atoms i per unit volume is $\mathcal{N}_i = (N_A \rho / A_i) c_i$, where ρ is the mass density of the material. In the following, we assume that the target is irradiated with electrons of a given energy, that impinge normally on the surface.

The depth distribution of ionization for the considered element, denoted by $\phi_i(z)$, can be expressed as (see Eq. 2.26)

$$\phi_i(z) = J_0^{-1} \int \mathrm{d}E \, \mathcal{N}_i \sigma_i(E) \int_{-1}^{1} \mathrm{d}\mu \, \psi(z, E, \mu), \tag{5.2}$$

where $\sigma_i(E)$ is the ionization cross section for the considered shell. The quantities μ, $\psi(z, E, \mu)$ and J_0 are described in section 2.1. $\phi_i(z)\,\mathrm{d}z$ represents the number of ionizations produced between z and $z + \mathrm{d}z$ and

$$\int_{-\infty}^{\infty} \mathrm{d}z \, \phi_i(z) \tag{5.3}$$

is the total number of ionizations produced in the sample, per incident electron. The characteristic x-ray intensity measured with an x-ray spectrometer placed at a takeoff angle χ, can then be written as

$$I_i = \epsilon \frac{\Omega}{4\pi} \omega_i \, p_i \int_0^{\infty} \phi_i(z) \exp\left[-\frac{\mu_i z}{\sin\chi}\right] \mathrm{d}z, \tag{5.4}$$

where ϵ is the spectrometer efficiency, $\Omega/4\pi$ is the solid angle of collection, μ_i/ρ the mass absorption coefficient for the characteristic x-ray in the material, ω_i is the fluorescence yield and p_i is the line fraction. Notice that the dependence of the line intensity on the concentration is through the $\phi_i(z)$ function.

In order to measure the ionization distribution, a thin layer of tracer element of thickness t is immersed at different depths in a homogeneous material (matrix), preferably of atomic number similar to that of the tracer. The number of x-rays emitted from the tracer layer at depth z per incident electron is given by

$$I(z) = \left(\epsilon \frac{\Omega}{4\pi} \omega_i \, p_i \, t\right) \phi_i(z) \exp\left[-\frac{\mu_i z}{\sin\chi}\right]. \tag{5.5}$$

In principle, this equation can be used to infer the value of $\phi(z)$ from the measured $I(z)$. However, this requires accurate knowledge of factors within the parenthesis (namely, layer thickness, spectrometer efficiency, solid angle of detection, fluorescent yield and line fraction). To eliminate the effect of these parameters Castaing "normalized" the depth distribution of ionization to the number of ionizations produced in an isolated

layer of the tracer element (with the same thickness as the embedded layer) under the same irradiation conditions. This number of ionizations is

$$N_i = \mathcal{N}_i\, t\, \sigma_i(E_0). \tag{5.6}$$

Therefore, the normalized distribution, denoted as $\Phi_i(z)$, reads,

$$\Phi_i(z) \equiv \frac{\phi_i(z)t}{N_i} = \frac{J_0^{-1}\int_{E_0}^{E_i} \mathrm{d}E\, \sigma_i(E) \int_{-1}^{1} \mathrm{d}\mu\, \psi(z,E,\mu)}{\sigma_i(E_0)}. \tag{5.7}$$

Thus, the intensity in Eq. (5.5) normalized to the intensity emitted by the unsupported layer reads,

$$I'(z) = \Phi_i(z) \exp\left[-\frac{\mu_i z}{\sin\chi}\right]. \tag{5.8}$$

With this, the determination of $\Phi(z)$ from $I'(z)$ is straightforward. Unfortunately, the $\Phi(z)$ function is not a proper distribution; firstly, it is dimensionless, and secondly, its integral does not give the total number of ionizations. The number of ionizations per electron produced at depths between z and $z + \mathrm{d}z$ is given by $\mathcal{N}_i\, \sigma_i(E_0)\, \Phi(z)\, \mathrm{d}z$. The x-ray intensity emerging from the sample surface is

$$I_i = \mathcal{N}_i\, \epsilon\, \frac{\Omega}{4\pi}\, \omega_i\, p_i\, \sigma_i(E_0) \int_0^{\infty} \Phi_i(z)\, \exp\left[-\frac{\mu_i z}{\sin\chi}\right] \mathrm{d}z. \tag{5.9}$$

Usually the ionization depth distribution is given as a function of mass depth, ρz.

The value of the depth distribution of ionization for $z = 0$ is usually referred to as the surface ionization. From Eq. (5.7), we have

$$\Phi_i(0) = \frac{J_0^{-1}\int_{E_0}^{E_i} \mathrm{d}E\, \sigma_i(E) \int_{-1}^{1} \mathrm{d}\mu\, \psi(0,E,\mu)}{\sigma_i(E_0)}. \tag{5.10}$$

If the flux is divided into forward and backward components, $\Phi(0)$ can be written as

$$\begin{aligned} \Phi_i(0) &= 1 + \frac{J_0^{-1}\int_{E_0}^{E_i} \mathrm{d}E\, \sigma_i(E) \int_{-1}^{0} \mathrm{d}\mu\, \psi_{\mathrm{B}}(0,E,\mu)}{\sigma_i(E_0)} \\ &= 1 + \frac{\int_{E_0}^{E_i} \mathrm{d}E\, \sigma_i(E) \int_{-1}^{0} \mathrm{d}\mu\, P_{\mathrm{B}}(E,\mu)\mu^{-1}}{\sigma_i(E_0)}, \end{aligned} \tag{5.11}$$

where $P_{\mathrm{B}}(E,\mu)$ represents the energy and angular distribution of backscattered electrons. The first term in Eq. (5.11) corresponds to the ionization by the incident electron beam, whereas the second term corresponds to the ionization of backscattered electrons that reach the target surface.

In the case of a film of finite thickness t deposited on a substrate, the x-ray intensity from an element in the film, is given by

$$I_{fi} = \mathcal{N}_i \epsilon \frac{\Omega}{4\pi} \omega_i p_i \sigma_i(E_0) \int_0^t \Phi_{fi}(z) \exp\left(-\frac{\mu_{fi} z}{\sin\chi}\right) \mathrm{d}z, \tag{5.12}$$

where μ_{fi} and $\Phi_{fi}(z)$ are the absorption coefficient and the ionization distribution in the film, respectively. Notice that the integration is now performed from 0 to t. The x-ray intensity emitted by the substrate material is

$$\begin{aligned} I_{si} &= \mathcal{N}_i \epsilon \frac{\Omega}{4\pi} \omega_i p_i \sigma_i(E_0) \exp\left(-\frac{\mu_{fi} t}{\sin\chi}\right) \int_t^\infty \Phi_{si}(z) \exp\left[-\frac{\mu_{si}(z-t)}{\sin\chi}\right] \mathrm{d}z \\ &= \mathcal{N}_i \epsilon \frac{\Omega}{4\pi} \omega_i p_i \sigma_i(E_0) \exp\left[-\frac{t(\mu_{fi}-\mu_{si})}{\sin\chi}\right] \int_t^\infty \Phi_{si}(z) \exp\left[-\frac{\mu_{si} z}{\sin\chi}\right] \mathrm{d}z \end{aligned} \tag{5.13}$$

where μ_{si} and $\Phi_{si}(z)$ are the absorption coefficient and the depth distribution of ionizations for the considered element in the substrate, respectively. Notice that the integration is performed from t to infinity. The exponential outside the integral describes absorption of emitted x-rays in the overlayer.

5.2 Simulation of ionization distributions

As mentioned previously, PENELOPE accounts for the average effect of inelastic collisions on the primary electron through an *approximate* DCS. The simulation algorithm adopted in PENELOPE was devised to provide an accurate description of the penetration and slowing down of electrons and, for the sake of simplicity, the description of certain interactions that occur with exceedingly small probability was oversimplified. Thus, the production of inner–shell ionization by electron impact was disregarded, since the overwhelming majority of inelastic collisions involve electrons in the outer, weakly bound shells of the target atoms. In order to obtain reliable inner-shell ionization distributions, a more realistic cross section model for this process should be considered. On the other hand, K-shell ionization is a very unlikely event and, therefore, direct scoring of actual ionizations along the generated electron trajectories is very inefficient. The practical solution consists of generating electron trajectories, and scoring the *expected* number of ionizations n in each free flight. To obtain n, only knowledge of the total ionization cross section as a function of the electron energy, $\sigma_K(E)$, is required. Indeed, in a free flight of length s, the expected number of ionizations caused by an electron of energy E is

$$n = \mathcal{N} s \sigma_K(E), \tag{5.14}$$

where $\mathcal{N}$ is the density of atoms of the considered (ionized) element per unit volume. This number of ionizations is "deposited" at a random point along the free flight. The depth distribution of ionizations is finally normalized accordingly to Castaing's definition.

5.3 Comparison of simulation with experiment

In the simulations reported here, 200,000 electron tracks were generated in each run, which is a number large enough to make sure that the statistical uncertainty (3σ) of the calculated surface ionization is less than 2%. The cut-off energy was set to 100 eV.

5.3.1 The surface ionization

In a first set of simulations, $\Phi(0)$ was determined for different combinations of bulk targets (matrices) and tracer elements, for K-shell ionization. In Table 5.1, the simulation results are compared with experimental data corresponding to the measurements by Castaing and Descamps (1955), Castaing and Hénoc (1965), Shimizu et al. (1965), Vignes and Dez (1968), Sewell et al. (1985), Merlet (1992). Values of $\Phi(0)$ measured in the present work (see section 5.4) are also included. From this comparison, we see that agreement between simulation results and experiment is reasonable in some cases (within 1-2%), but in other cases the differences are as large as 10%. However, even the largest differences are less than the uncertainties quoted by the authors (5-10%), so that agreement may be considered as globally satisfactory.

Table 5.1: Comparison of experimental and simulated $\Phi(0)$ values.

Matrix	E (keV)	Tracer	Monte Carlo	Experiment	Exp. Reference
C	5.0	Al	1.11	1.12	Sewell et al. (1985)
C	10.0	Al	1.13	1.12	Sewell et al. (1985)
C	15.0	Al	1.11	1.13	Sewell et al. (1985)
Al	10.0	Si	1.30	1.20	Sewell et al. (1985)
Al	15.0	Mg	1.36	1.38	Castaing and Hénoc (1965)
Al	15.0	Si	1.32	1.32	Sewell et al. (1985)
Al	20.0	Mg	1.36	1.37	Castaing and Hénoc (1965)
Al	25.0	Mg	1.37	1.38	Castaing and Hénoc (1965)
Al	29.0	Mg	1.38	1.39	Castaing and Hénoc (1965)
Mg	10.0	Al	1.29	1.22	Merlet (1992)
Mg	15.0	Al	1.32	1.36	Merlet (1992)
Mg	20.0	Al	1.32	1.37	Merlet (1992)
Mg	25.0	Al	1.33	1.37	Merlet (1992)
Mg	30.0	Al	1.34	1.34	Merlet (1992)
Mg	35.0	Al	1.34	1.33	Merlet (1992)

Matrix	E (keV)	Tracer	Monte Carlo	Experiment	Exp. Reference
Ti	17.0	V	1.37	1.41	Vignes and Dez (1968)
Ti	20.0	V	1.40	1.45	Vignes and Dez (1968)
Ti	25.0	V	1.43	1.50	Vignes and Dez (1968)
Ti	29.0	V	1.44	1.55	Vignes and Dez (1968)
Ti	35.0	V	1.46	1.57	Vignes and Dez (1968)
Ni	17.0	Cu	1.33	1.31	Vignes and Dez (1968)
Ni	20.0	Cu	1.38	1.39	Vignes and Dez (1968)
Ni	24.0	Cu	1.42	1.46	Vignes and Dez (1968)
Ni	29.0	Cu	1.46	1.57	Vignes and Dez (1968)
Ni	35.0	Cu	1.50	1.58	Vignes and Dez (1968)
Ni	10.0	Cu	1.07	1.04	Merlet (1992)
Ni	15.0	Cu	1.28	1.38	Merlet (1992)
Ni	20.0	Cu	1.38	1.31	Merlet (1992)
Ni	25.0	Cu	1.43	1.52	Merlet (1992)
Ni	30.0	Cu	1.46	1.53	Merlet (1992)
Ni	35.0	Cu	1.50	1.59	Merlet (1992)
Ni	40.0	Cu	1.51	1.62	Merlet (1992)
Ni	45.0	Cu	1.52	1.67	Merlet (1992)
Co	10.0	Cu	1.07	1.01	Merlet (1992)
Co	15.0	Cu	1.27	1.33	Merlet (1992)
Co	20.0	Cu	1.36	1.30	Merlet (1992)
Co	25.0	Cu	1.42	1.49	Merlet (1992)
Co	30.0	Cu	1.46	1.50	Merlet (1992)
Co	35.0	Cu	1.49	1.54	Merlet (1992)
Co	40.0	Cu	1.57	1.49	Merlet (1992)
Co	45.0	Cu	1.59	1.61	Merlet (1992)
Cu	13.4	Zn	1.32	1.27	Brown (1966)
Cu	18.4	Zn	1.48	1.43	Brown (1966)
Cu	23.1	Zn	1.53	1.54	Brown (1966)
Cu	23.8	Zn	1.54	1.34	Shimizu et al. (1965)
Cu	26.5	Zn	1.56	1.38	Shimizu et al. (1965)
Cu	27.6	Zn	1.56	1.57	Brown (1966)
Cu	28.5	Zn	1.57	1.42	Shimizu et al. (1965)
Cu	29.0	Zn	1.57	1.50	Castaing and Descamps (1955)
Cu	10	Ni	1.10	1.12	This work
Cu	15	Ni	1.29	1.30	This work
Cu	20	Ni	1.40	1.38	This work
Cu	25	Ni	1.43	1.44	This work
Cu	30	Ni	1.47	1.47	This work

5.3.2 Depth distribution of ionizations

Comparison of simulated ionization-depth distributions with experiment can provide a valuable guide to select the most adequate ionization cross section. We have performed simulations of the $\Phi(\rho z)$ function using the various ionization cross sections described in section 1.1.3, namely the analytical formulas of Bethe–Powell (1985), Worthington and Tomlin (1956), Gryzinski (1965) and the optical-data model of Mayol and Salvat (1990).

Simulated depth distributions of ionization for copper and magnesium tracers in an aluminium matrix, obtained with the aforesaid total ionization cross sections, are compared with experimental data (Castaing and Descamps 1955, Castaing and Hénoc 1966) in Fig. 5.1. The interesting feature here is the clear influence of the adopted ionization cross section on the shape of the $\Phi(\rho z)$ function. This influence could give rise to large errors in the calculated x-ray intensity especially in thin films or layered samples. This is particularly evident for the Bethe-Powell formula, which is in marked error for incident electron energies close to the ionization threshold. As indicated above, in the following, we shall exclusively use the ionization cross section obtained from Mayol and Salvat's optical data model, which is physically more sound.

Fig. 5.2a shows $\Phi(\rho z)$ functions for K-shell ionization of carbon atoms embedded in a silver matrix for different beam energies. The simulation reveals that the value of $\Phi(0)$ is practically independent of the electron energy. This is at variance with measured data of Rehbach (1988). Very likely, the variation of the measured $\Phi(0)$ with energy can be attributed to the finite thickness of the tracer layer used in the experiments. Depth distribution of ionizations for Si tracer on an Au matrix are compared with those measured by Brown and Parobek (1976) in Fig. 5.2b, at incident electron energies of 10, 20 and 29 keV.

Fig. 5.3a shows the depth distribution functions for Cu tracer in Al matrix at electron incident energies of 12 and 15 keV. The experimental data is from Brown and Parobek (1976). In this case, the agreement is found to be satisfactory. Simulated depth distributions of K-shell ionization of Zn atoms in a copper matrix for 20 kV and 30 kV electron beams are compared with experimental data of Brown and Parobek (1972) in Fig. 5.3b. Apart from a slight difference in the positions of the maxima, the agreement between simulation and experiment is also satisfactory.

It is worth recalling that experimental measurements are affected by large uncertainties which make it difficult to assess the accuracy of the simulation. These uncertainties mainly arise from the finite thickness of the tracer, which can strongly influence the shape of the measured $\Phi(\rho z)$ curve, as pointed out by several authors (Castaing and Descamps, 1955; Karduck and Rehbach, 1991). Fluorescence due to excitation by x-rays and bremsstrahlung may also influence the $\Phi(\rho z)$ function at relatively large depths.

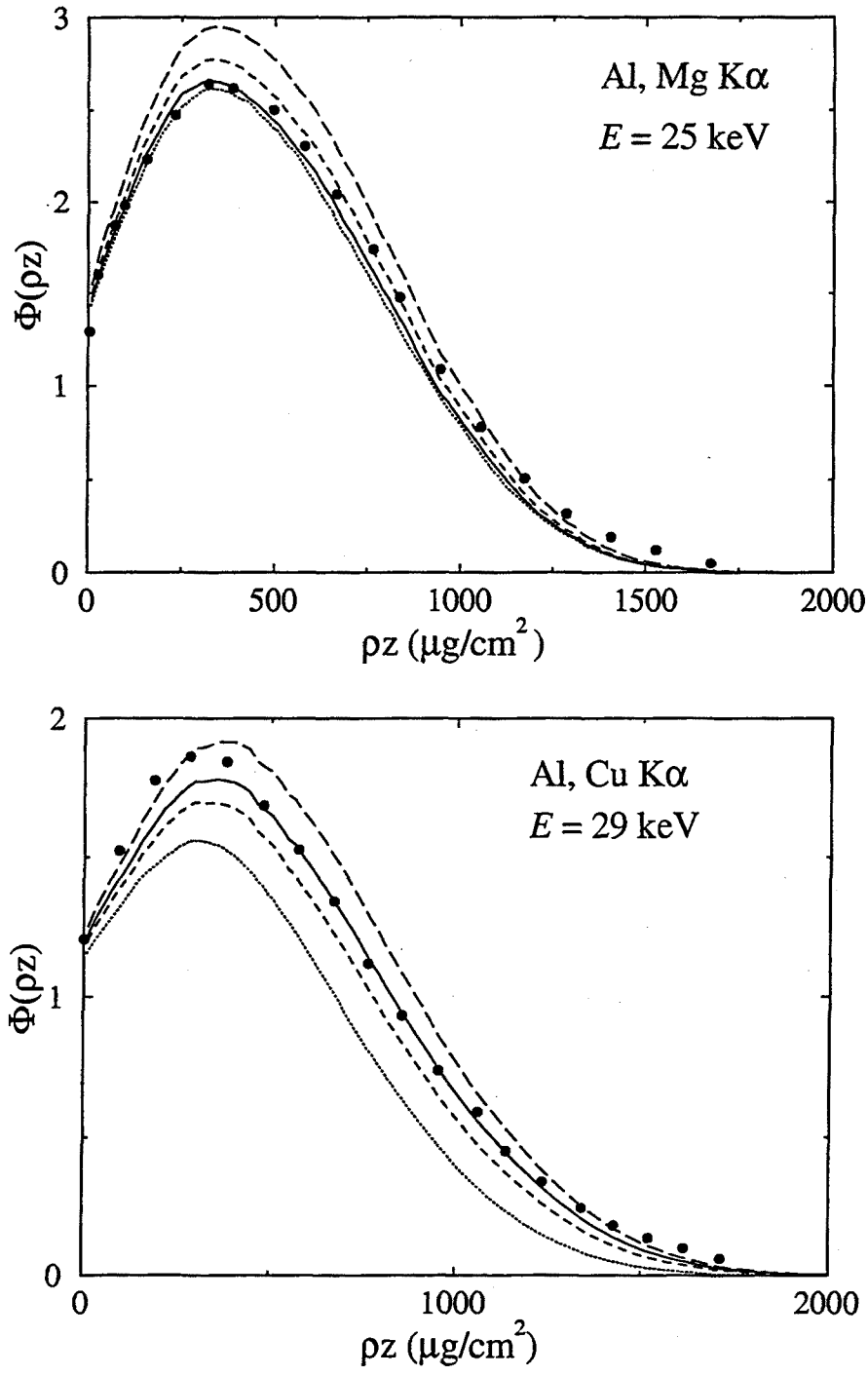

Figure 5.1: Depth distributions of K-shell ionizations of Mg (a) and Cu (b) in an Al matrix for 25 and 29 kV electrons, respectively. Experimental data are from Castaing and Descamps (1955) and Castaing and Hénoc (1966). Lines represent Monte Carlo results using different total ionization cross sections: Mayol-Salvat (solid), Powell (dotted), Gryzinsky (dashed) and Worthington-Tomlin (long-dashed). Ionization energies of the K-shells of Mg and Cu are 1.74 keV and 9.8 keV, respectively.

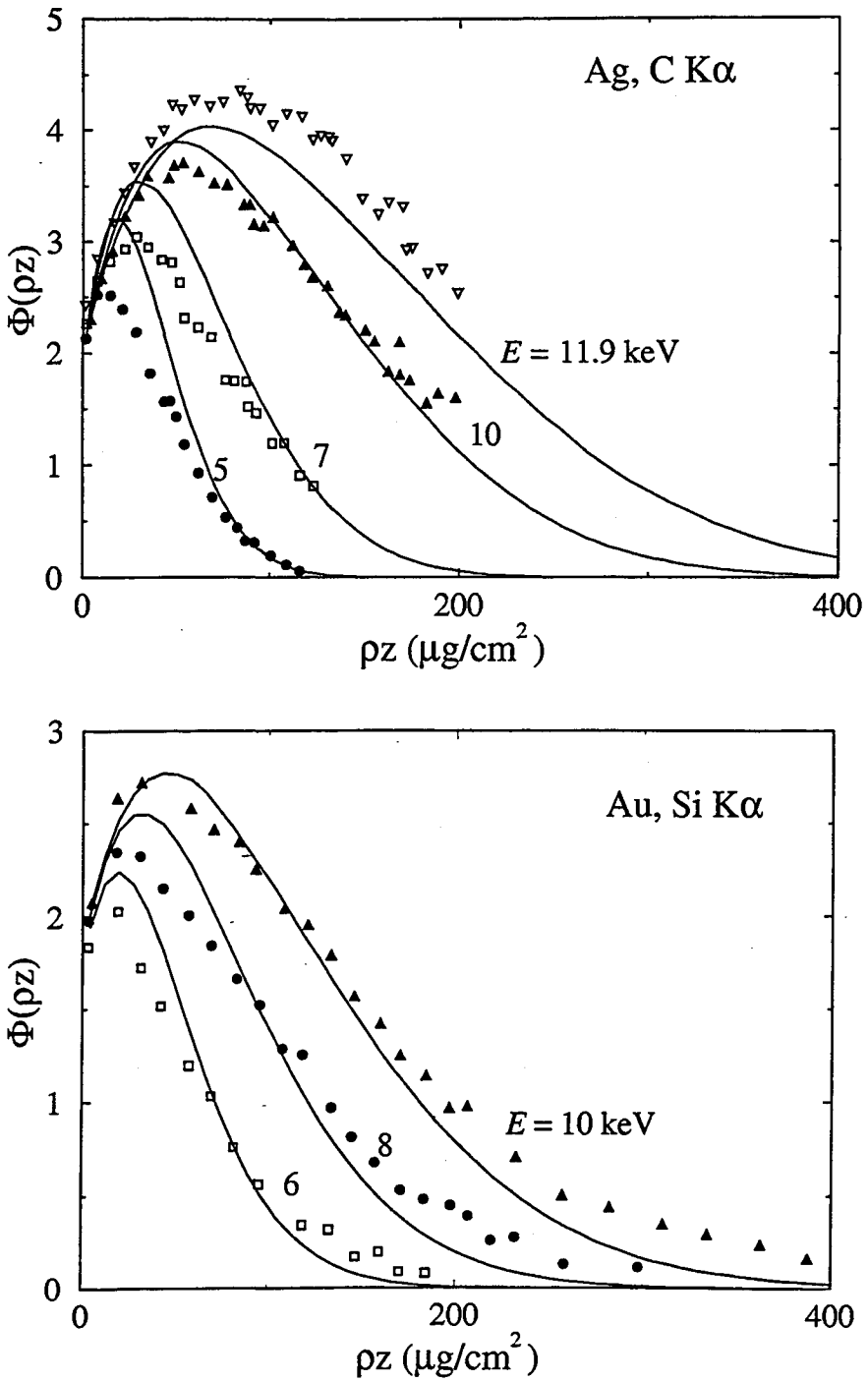

Figure 5.2: Depth distribution of K-shell ionizations for a C tracer in an Ag matrix (a) and Si tracer in Au (b). Experimental data in part (a) are from Rehbach (1988); those in part (b) are from Brown and Parobek (1976). Solid lines represent results from our Monte Carlo calculations.

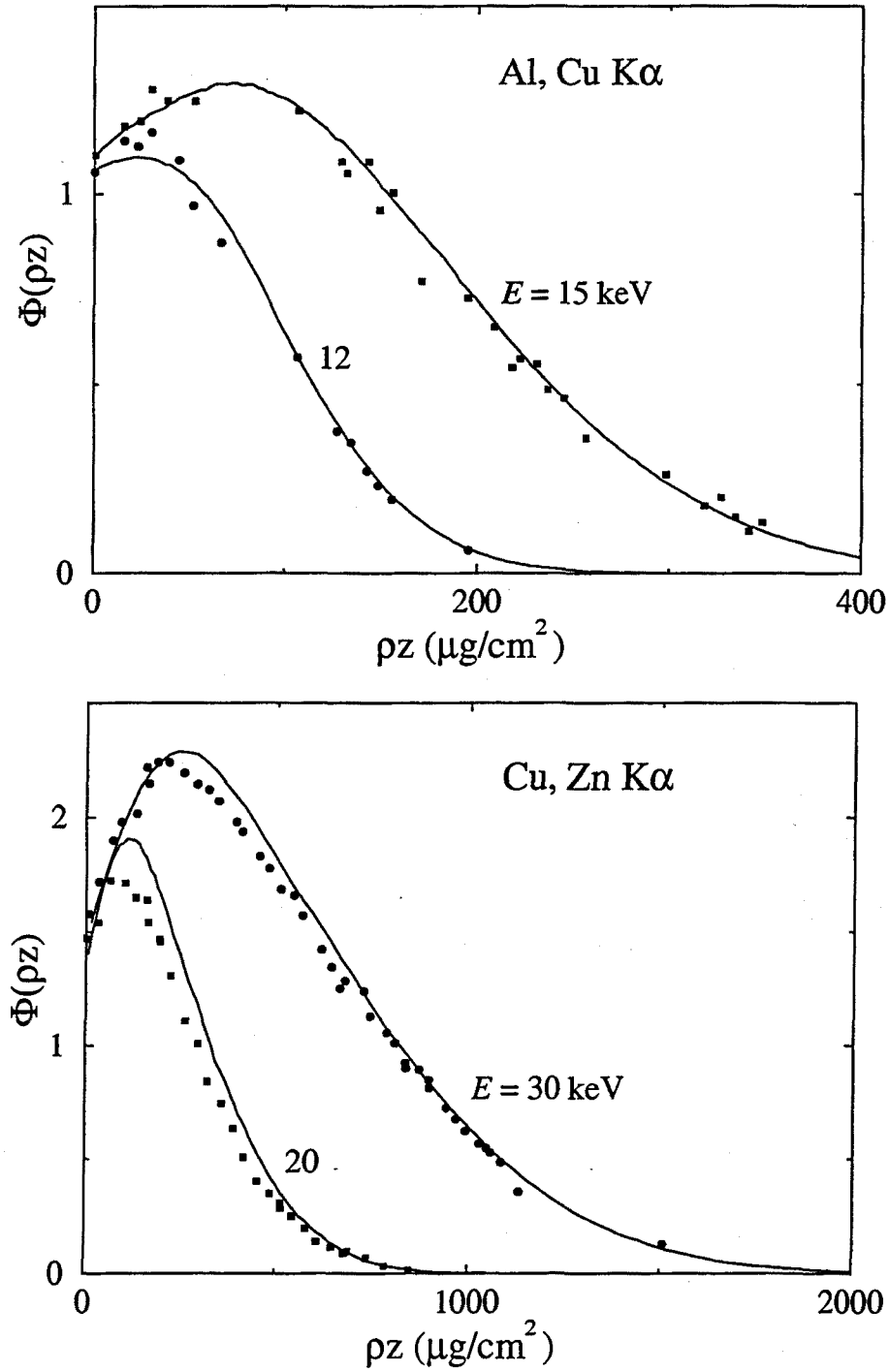

Figure 5.3: Depth distribution of K-shell ionizations for a Cu tracer in an Al matrix (a) and Zn tracer in Cu (b). Experimental data in part (a) are from Brown and Parobek (1976); those in part (b) are from Brown and Parobek (1972). Solid lines represent results from our Monte Carlo calculations.

5.3.3 Emerging intensity from thin films

The reliability of the calculation of x-ray emission from thin films on substrates can be assessed by studying the energy dependence of the emitted x-ray intensities from both the film and the substrate, or the corresponding k-ratios. A large number of k-ratio measurements in thin films on substrates is available from the literature (e.g. Kyser and Murata, 1974; Reuter et al, 1978; Pouchou and Pichoir, 1984; Packwood et al. 1989; Murata and Sugiyama, 1989). Recently, Bastin et al. (1996) have started to produce a large, systematic data base with measured k-ratios of a wide variety of film-on-substrate samples, including pairs with high differences in atomic number. This kind of information is essential to validate analytical procedures that have been proposed for EPMA of multilayered samples.

Experimental k-ratios from Al films deposited on Si and W substrates, as functions of the incident electron beam energy are displayed in Fig. 5.4, for both the elements of the film and the substrate (Bastin, 1998). Our simulations of these quantities are in excellent agreement with experimental data. It should be pointed out that the k-ratio relates two quantities given by integrals of the ionization depth distribution, which include a correction accounting for x-ray absorption [see Eq. (5.9)]. As a consequence, from the mere agreement between simulation and experiment we cannot conclude that our simulated $\Phi(\rho z)$ functions are correct to the same extent as the k-ratios. It should be noted that a common tendency in practical EPMA is to use empirical models based on a given parameterization of the $\Phi(\rho z)$ function and empirically modify its parameters and also the MAC to reproduce the observed k-ratios. Obviously, this kind of procedure should not be followed, in spite of the fact that it may work quite well for a given class of samples and conditions (those that were effectively fitted).

5.4 Experimental measurement of $\Phi(0)$ in thin films on substrates

In this section we present experimental measurements and Monte Carlo simulations of the Ni K-shell surface ionization for specimens consisting of thin copper films of various thicknesses deposited onto a variety of substrates, and for varying accelerating voltages.

5.4.1 Sample preparation

Cu films were deposited by thermal evaporation on 1-inch-diameter samples which contained different polished pure substrates (Fig. 5.5). Simultaneously, for mass thickness determination, the Cu films were deposited on four thin aluminium sheets of known area

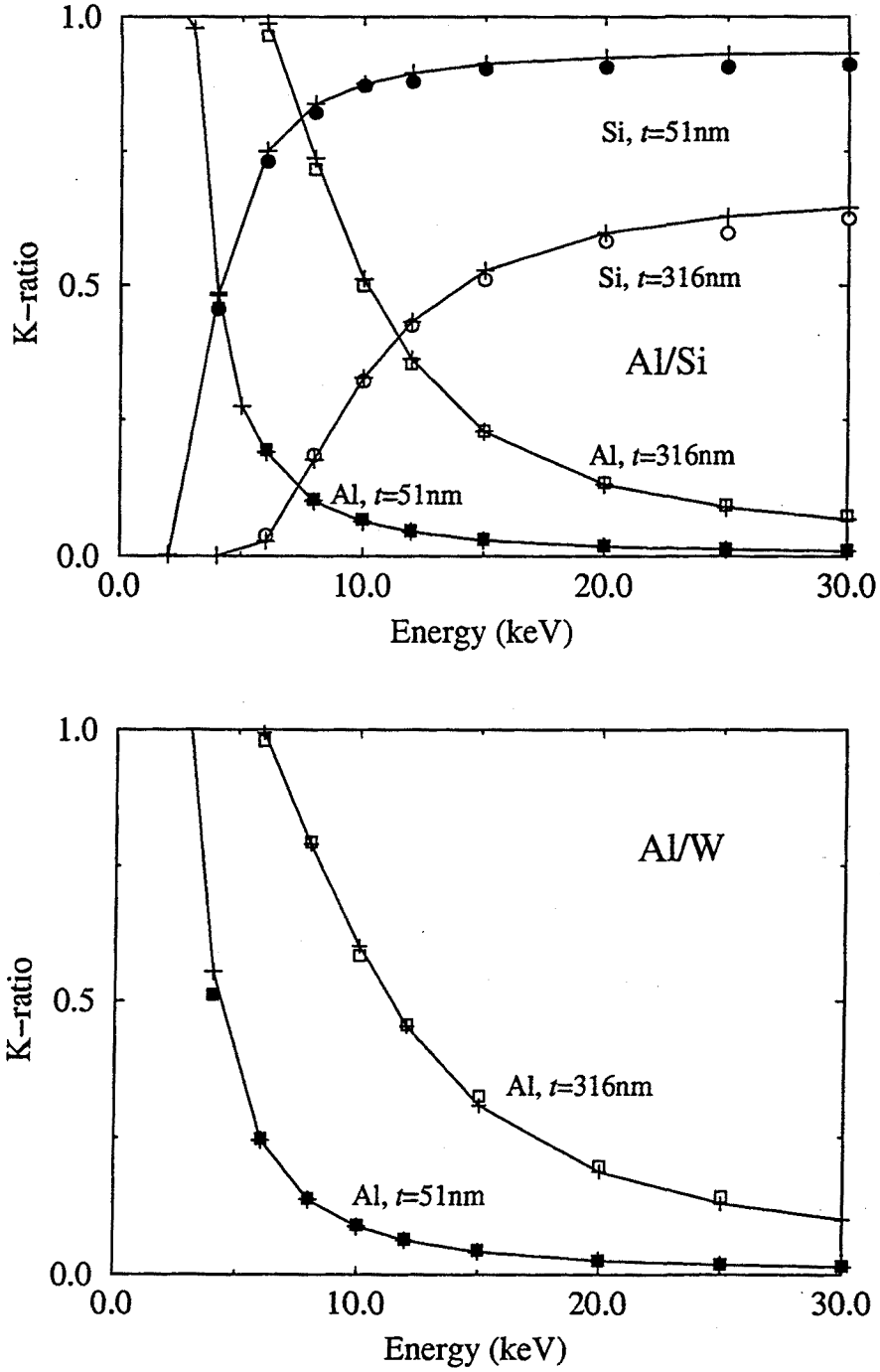

Figure 5.4: Variation of k-ratio with electron incident energy for Al films with thicknesses of 51 nm and 316 nm deposited on (a) silicon and (b) tungsten. In the first case, the Si Kα k-ratio is also plotted. Circles and squares represent experimental measurements of Bastin (1998). Crosses, joined with lines, are our simulation results.

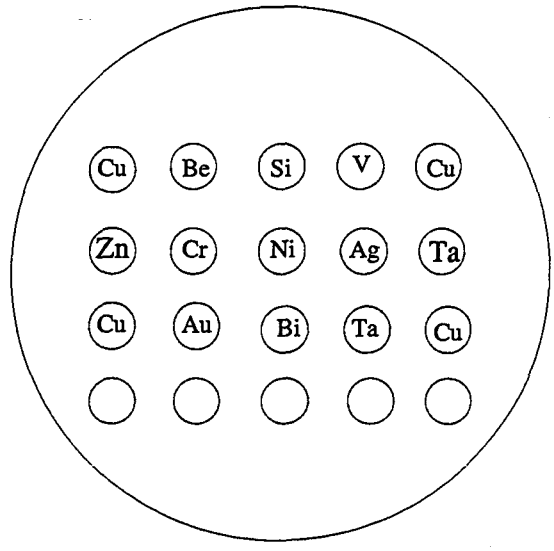

Figure 5.5: Schematics of the sample containing the different substrates. On this sample subsequent layers of Cu and Ni were evaporated.

and weight, situated at the same distance from the evaporation source. Afterwards, Ni tracer films were deposited on the previously prepared samples and, in the same runs, the tracer films have been deposited on self-supporting carbon films of approximately 30 nm, previously prepared as described in chapter 4. The particular choice of tracer element (Ni) and film composition (Cu) was motivated by the need to minimize experimental uncertainties. Elements Ni and Cu which have atomic number 28 and 29 respectively, have similar scattering effects, moreover Cu cannot enhance Ni peaks by characteristic fluorescence, and finally the Cu film reduces the characteristic and continuum fluorescence of the tracer from the substrate. The homogeneity of the Ni tracer film deposited on the 1-inch-diameter target was carefully checked by comparing the Ni Kα signal measured at the four exterior substrates (see Fig. 5.5), which contained the same substrate (Cu). One of the most important factors in preparing the samples is to ensure that the self-supported film and those deposited on the substrates have the same thickness. This is crucial to obtain realistic values of the surface ionization. Mass thicknesses of Cu films were measured by direct weighing of the evaporated material on the aluminium sheets on a microbalance. With this method, the film mass thickness ρt is obtained by the simple relation (see e.g Ohring, 1990)

$$\rho t = \frac{M}{A}, \tag{5.15}$$

where M and A are the mass and area of the film. The accuracy of the weighing method is estimated to be about 5% for a mass thickness of 100 $\mu g/cm^2$, which is mainly limited by the precision of the microbalance. This accuracy could not be improved by using a larger area aluminium sheet owing to the inhomogeneity produced by geometrical effects in the evaporation process (Ohring, 1990). Mass thicknesses have also been obtained by electron microprobe measurements using the procedure described in chapter 4. In this case, measurements were performed on the targets Cu/Zn and Cu/Ni, at various accelerating voltages (10, 15, 20, 25 kV), and results were processed with the help of the program X-FILM (Merlet, 1995). As the selected substrates have similar atomic number to the films, the electron microprobe should give an accuracy better than 2% in the thickness determination of the Cu films.

The different methods for mass thickness determination gave results that agree to within 6%. It was found that the agreement was better for thinner films. As an example, Table 5.2 shows the values of thicknesses obtained by the two methods, for two of the evaporated samples. In summary, the accuracy of the mass-thickness determination was estimated to be $\pm$ 6%.

Table 5.2: Comparison of results as regards the thickness of the Cu layers obtained by the weighing method and by electron probe microanalysis using the X-FILM program (Merlet, 1995).

Mass thickness ($\mu g/cm^2$)	
Weighing	EPMA
60.7 $\pm$ 1.2	64.0 $\pm$ 3.2
36.0 $\pm$ 0.7	36.4 $\pm$ 1.8

To minimize the bias in the determination of the surface ionization due to the thickness of the tracer film, the Ni layer must be as thin as possible. However, it must not be too thin, since a small peak-to-background ratio would imply unacceptably large statistical uncertainties in the peak intensity. The thicknesses of the Ni layers, estimated by EPMA, were in the range 2-4 $\mu g/cm^2$, which seems to represent a good compromise between the thickness bias and the statistical requirements. In the following, where the thicknesses are given as lengths, the density of bulk material is assumed.

5.4.2 Measurement procedures

The surface ionization was obtained by comparing the number I_S of characteristic x-rays that the tracer layer yields, to the number I_0 emitted by the same, self-supporting, layer.

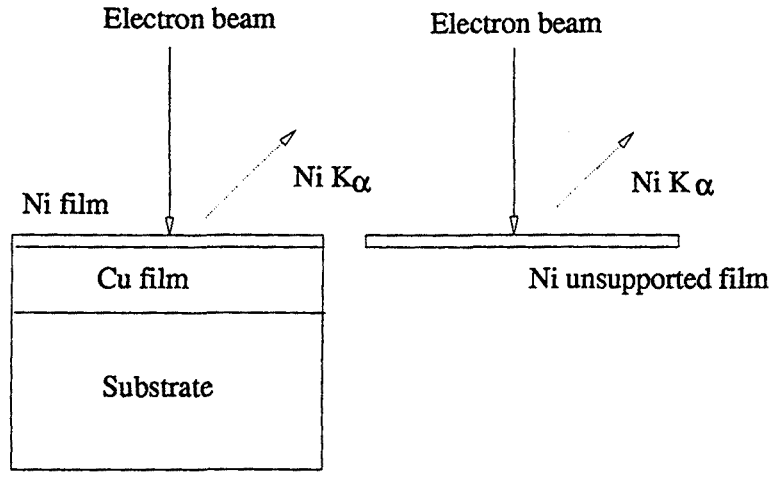

Figure 5.6: Experimental arrangement to measure the surface ionization of thin films on substrates.

Explicitly,

$$\Phi(0) = \frac{I_S}{I_0}. \tag{5.16}$$

The schematics of the experimental measurement is shown in Fig. 5.6.

Measurements were carried out at 10, 15, 20, 25 and 30 kV on the CAMECA SX-50 electron microprobe using the wavelength dispersive spectrometer, with a LiF crystal. Peak intensities were measured using the standard procedure, i.e by setting the crystal spectrometer at the wavelength where the peak is maximum. Background intensity was estimated by linear interpolation of measurements at both sides of the characteristic peak. In order to decide the best positions for background measurements, x-ray spectra, centred at the position of the Ni Kα peak, were recorded for all the targets. The spectra corresponding to 40.5-nm-thick Cu films deposited on Be, Cr, Nb and Bi are displayed in Fig. 5.7. We can see that peak-to-background ratios are relatively small and that there is an increase of bremsstrahlung background for increasing atomic number substrates. Owing to the relatively small peak-to-background ratios, careful background subtraction is required. Substrates that produce interferences for the Ni Kα peak, such as Co and W, were avoided. Care was also exercised in selecting the pulse-height analyzer discriminator settings in order to minimize high-order Bragg reflections coming from the substrate. These can be important for high atomic number substrates and high electron incident energies, since they produce interferences that may affect both the peak and background.

For each target and each voltage, at least five measurements at different positions

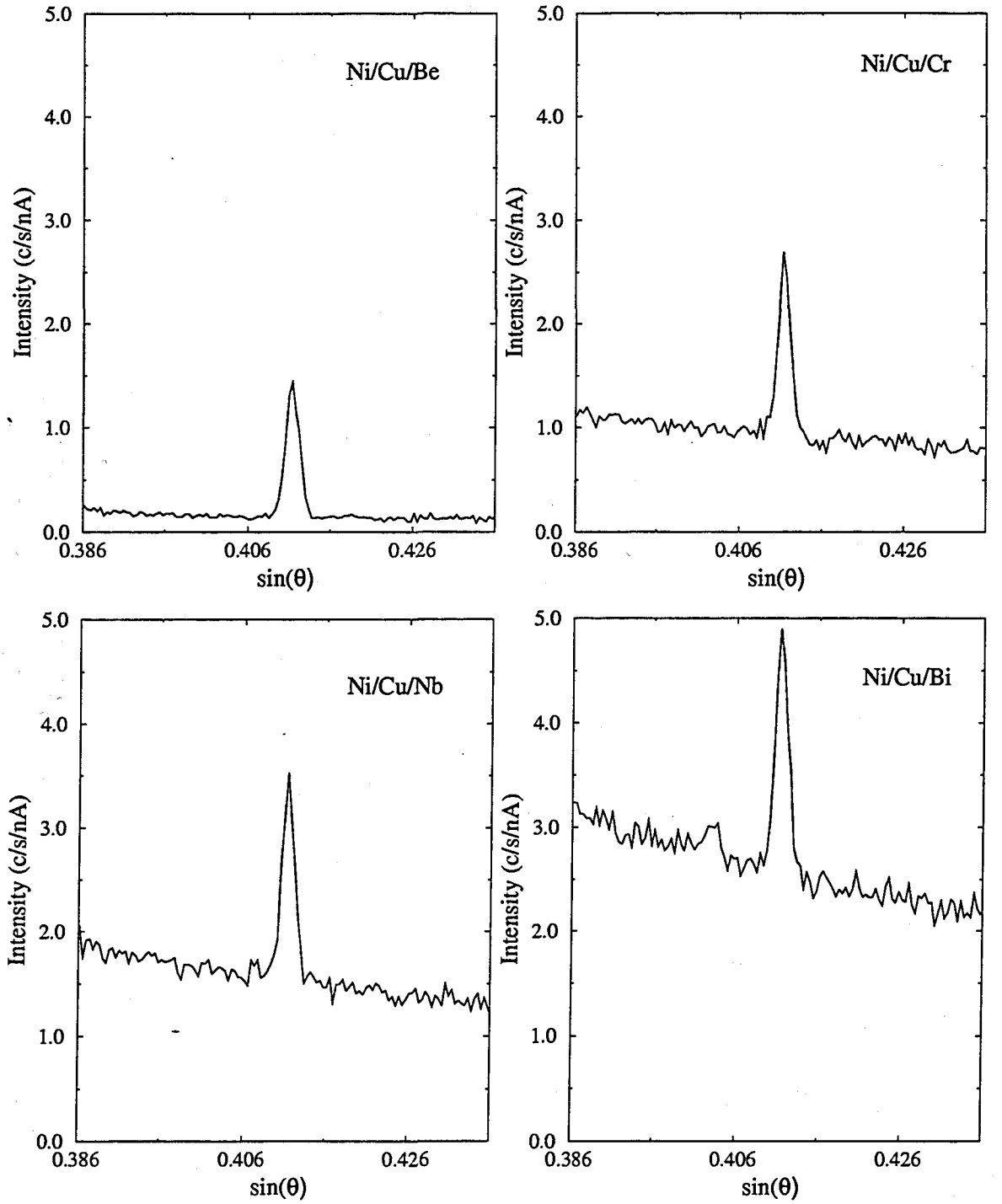

Figure 5.7: Experimental wavelength dispersive x-ray spectra of Ni tracer film deposited on 40.5 nm-thick Cu film deposited on Be (a), Cr (b), Nb (d) and Bi (d). Experimental conditions: 25 keV, 40 nA. LiF crystal. Oxygen-jet used. Counting time 5 sec/channel.

Table 5.3: Measured counting-rates for the Ni K_α peak, I_p, and background, I_b, corresponding to different substrates for the 40.5-nm-thick Cu film, at 20 keV electron incident energy and 40 nA beam current, with the relative error of $\Phi(0)$ (see chapter 3). Counting-rates for the unsupported Ni film were, in this case, 69.5 cps and 1.8 cps for the peak and background, respectively. Measuring times were 80 s and 60 s for the peak and background respectively.

Target	$I_p(c/s)$	I_b (c/s)	$\Phi(0)$	Error (%)
Ni/Cu/Be	80.6	5.5	1.10	± 4.4
Ni/Cu/Si	101.5	20.8	1.18	± 3.9
Ni/Cu/Cu	135.5	45.9	1.31	± 4.1
Ni/Cu/Ag	167.9	63.9	1.52	± 4.4
Ni/Cu/Au	181.3	78.3	1.68	± 4.5

on the specimen were made. Acquisition times and beam currents were adjusted in such a way that the statistical uncertainties were less than ± 5% (2σ). Table 5.3 gives typical values of measured counting-rates at different incident energies and the associated statistical uncertainties. To minimize carbon contamination in the sample during measurements, the oxygen-jet device and the liquid nitrogen cold finger was used. The use of the oxygen-jet was shown not to increase significantly the oxygen signal coming from the unavoidable oxide skin.

5.4.3 Results and discussion

Values of the surface ionization for Ni Kα tracer produced by electron beams with energies of 10, 15, 20, 25 and 30 keV at normal incidence, for Cu films of four different thicknesses (40.5, 67, 100 and 196 nm) on substrates of 9 elements, which span the periodic table, were measured and simulated.

The results of measurements and simulations, as functions of the atomic number of the substrate for the different bombarding energies, are compared in Figs. 5.8 and 5.9. We can see that in spite of the uncertainties arising from sample preparation and from the smallness of the peak-to-background ratio, experimental results and Monte Carlo simulations are found to agree, in general, to within about 5%.

From Figs. 5.8 and 5.9, it is seen that the surface film ionization increases with the atomic number of the substrate. This is because the heavier the substrate the larger the number of electrons backscattered from the substrate, which produce more ionizations in the film and at the surface. Accordingly, the dependence of $\Phi(0)$ on the atomic number of the substrate reduces when the thickness of the overlayer increases and/or when the electron beam energy decreases (i.e. when the number of electrons that reach

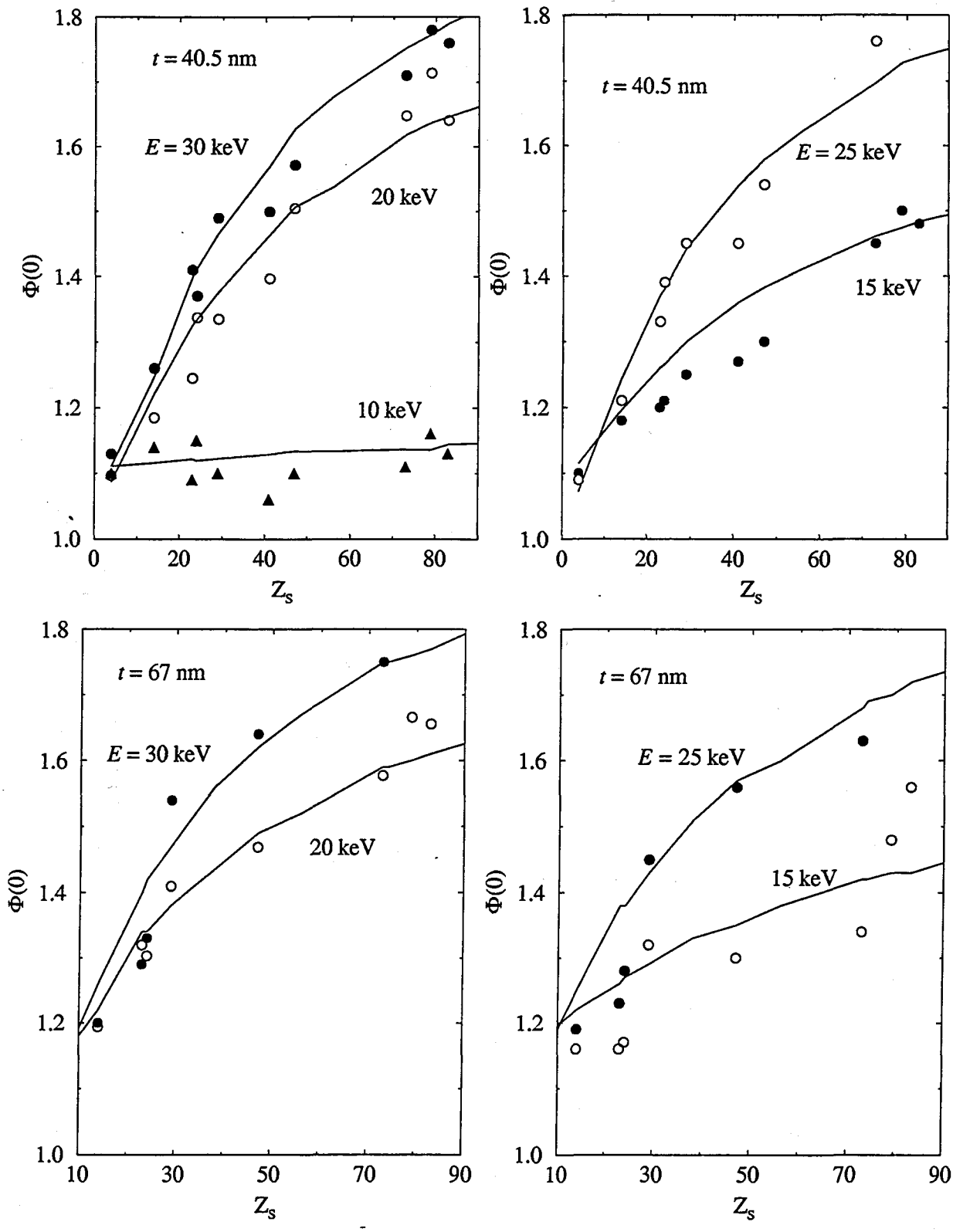

Figure 5.8: Surface ionization for a 40.5-nm-thick Cu film deposited onto different substrates as a function of the atomic number of the substrate, at 10 keV, 20 keV and 30 keV (a) and at 15 keV and 25 keV (b). The same for a 67-nm-thick Cu film at 20 keV and 30 keV (c), and at 15 keV and 25 keV (d). Continuous lines represent simulation results; open circles (15 keV and 20 keV), filled circles (25 keV and 30 keV) and filled triangles (10 keV) are experimental measurements at the indicated incident electron energies.

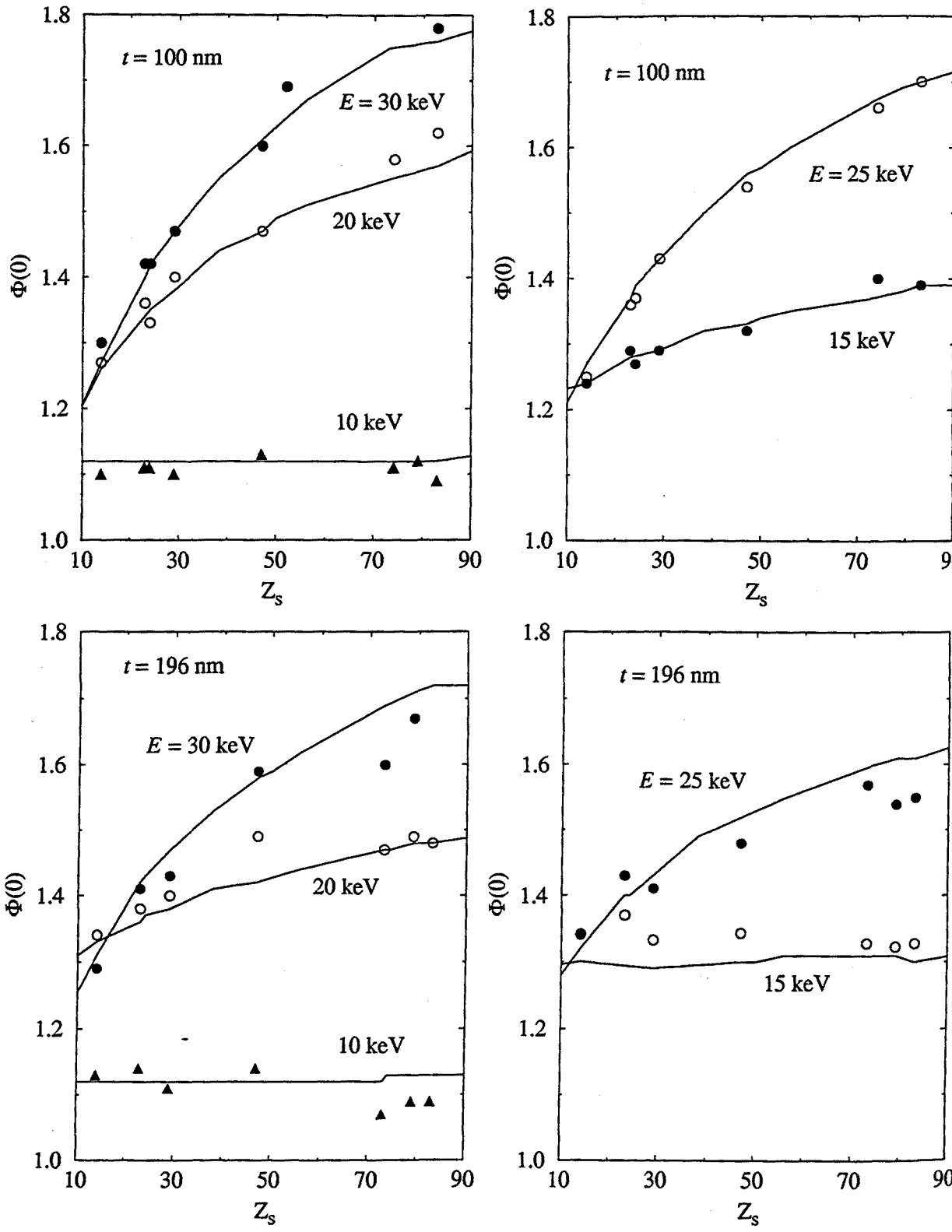

Figure 5.9: Surface ionization for a 100-nm-thick Cu film deposited onto different substrates as a function of the atomic number of the substrate, at 10 keV, 20 keV and 30 keV (a) and at 15 keV and 25 keV (b). The same for a 196-nm-thick Cu film at 10 keV, 20 keV and 30 keV (c), and at 15 keV and 25 keV (d). Continuous lines represent simulation results; circles (15 keV and 20 keV), filled circles (25 keV and 30 keV) and filled triangles (10 keV) are experimental measurements at the indicated electron incident energies.

the substrate with enough energy to return to the surface diminishes).

In Fig. 5.10, $\Phi(0)$ is plotted as a function of the film thickness for the samples of Cu/Be, Cu/Si, Cu/Ag and Cu/Au, at 25 keV electron incident energy. The behaviour of the surface ionization of the film-on-substrate composites is seen. For films of atomic number lower than the substrate, the effective value of $\Phi(0)$ increases with increasing film thickness, while for films of atomic number higher than the substrate, it decreases. In both cases, a saturation value corresponding to the bulk film material is reached. This behaviour is qualitatively similar to that of the backscattering coefficient, which is studied by Sogard (1980) and Hunger and Rogaschewski (1986).

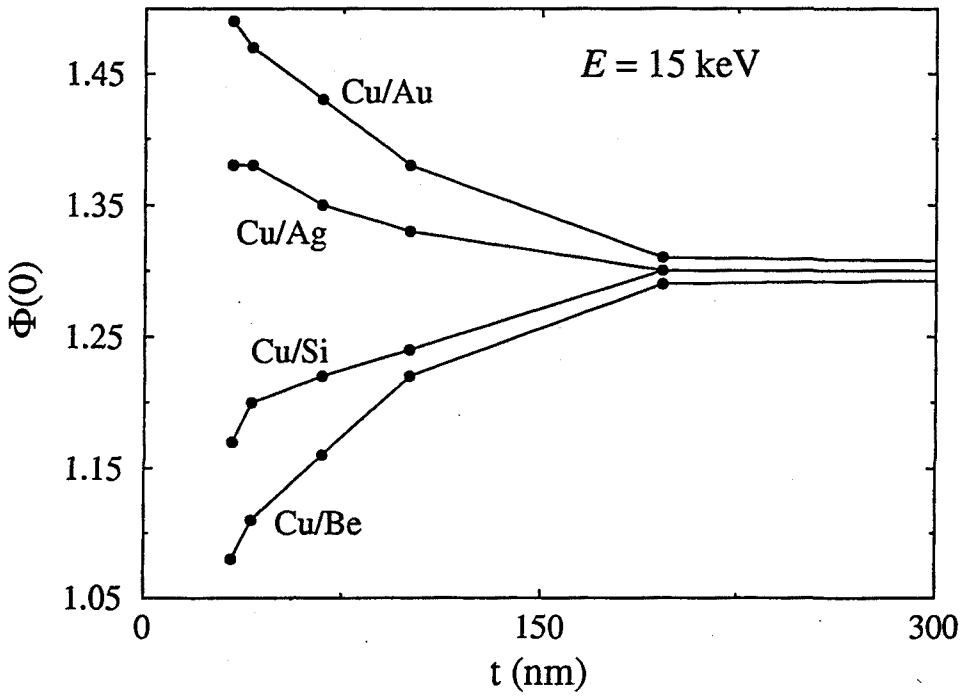

Figure 5.10: Surface ionization for Cu films deposited onto Be, Si, Ag and Au substrates as a function of the Cu film thickness.

5.4.4 Analytical formulas

Several authors have proposed analytical formulas to describe the surface ionization in thin films on substrates, which are of great interest for practical purposes (Hunger, 1988; Pouchou and Pichoir, 1984; Packwood and Milliken, 1986; Bastin et al. 1992; Merlet, 1995; Lee et al. 1996). As simulation results are free from experimental uncertainties, they provide a convenient basis to derive and/or investigate the validity of analytical empirical formulas. In the following, we shall derive an analytical expression to describe the data simulated in the preceding section.

A convenient starting point to establish analytical formulas is to use a normalized

$\Phi^N(0)$ value, defined as follows:

$$\Phi^N(0) = \left[\frac{\Phi_{FS}(0) - \Phi_S(0)}{\Phi_F(0) - \Phi_S(0)}\right], \tag{5.17}$$

where $\Phi_F(0)$ and $\Phi_S(0)$ are the surface ionizations for bulk samples of the film and substrate materials, respectively, and $\Phi_{FS}(0)$ is the value for the film-substrate system. This normalized value was adopted previously by Sogard (1980) and Hunger and Rogaschewski (1986) to obtain an universal effective backscattering coefficient η^N for film-substrate systems. The same authors proposed relating the $\eta^N(0)$ value to the film thickness $\rho d_{0.5}$, for which $\eta^N = 0.5\eta(0)$; therefore the dependence of $\eta^N(0)$ on the incident electron beam energy E_0 is largely reduced. Subsequently, Merlet (1995) and Lee et al. (1996) used similar approaches in describing the normalized surface ionization.

The common disadvantage of these approaches is that they require knowledge of the parameter $\rho d_{0.5}$ as a function of E_0. Alternatively, we may express the film thickness t in units of the effective ionization range R_x of electrons in the film material. R_x is defined as the average path length that electrons travel before slowing down to an energy equal to the ionization energy E_i of the considered atomic shell, i.e. R_x is the difference between the Bethe ranges of electrons with energies E_0 and E_i in the film material:

$$R_x = \int_{E_0}^{E_i} \frac{dE}{dE/ds}. \tag{5.18}$$

The advantage of using such a normalization length is that R_x can be easily calculated. In this work, the computation of R_x was performed by numerical integration of the stopping power given by the program MATERIAL of the PENELOPE code system (Salvat et al. 1996). The behaviour of the effective range as a function of the electron incident energy for bulk Cu and Ni Kα tracer is displayed in Fig. 5.11.

Fig. 5.12 shows the simulated normalized surface ionization as a function of reduced film thickness, $s = t/R_x$, calculated for different film thicknesses and electron energies, for Cu/Au, Cu/Ag and Cu/Si.

Table 5.4: Parameters of the empirical formula, (5.19), for the normalized surface ionization

Target	A	B
Cu/Au	4.90	3.41
Cu/Ag	4.49	10.49
Cu/Si	5.40	1.08
mean	5.15	2.25

The continuous curve in these figures represent the function

$$\Phi^N(0) = \tanh(A(Z, E_0)s + B(Z, E_0)s^2), \tag{5.19}$$

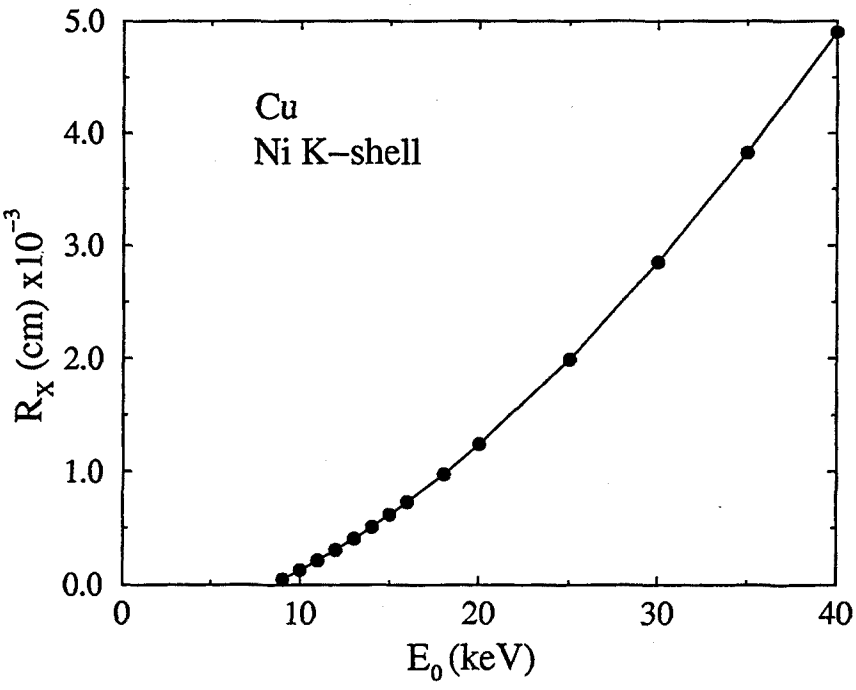

Figure 5.11: Effective range of electrons in Cu for Ni K-shell ionization, calculated as indicated in Eq. (5.18).

with the parameters determined by least-squares fitting of the simulated data, indicated in Table 5.4. The tanh function has been previously used by Sogard (1980) to describe the behaviour of η^N, and subsequently used by Hunger and Rogaschewski (1986). Recently, Merlet (1995) and Lee et al. (1996) used it to describe the surface ionization, with a different scaling law. A simpler approximation can be adopted by using the mean value of parameters A and B from the two extreme cases. With this approach, the normalized surface ionization $\Phi^N(0)$ scales with R_x. Therefore, for Cu films deposited on substrates, we can write

$$\Phi_{FS}(0) = \Phi_S(0) + [\Phi_F(0) - \Phi_S(0)] \tanh(5.15s + 2.25s^2). \qquad (5.20)$$

Our results thus confirm the validity of the assumed scaling properties, which provide a convenient basis to derive more general empirical formulas. Work along these lines is now in progress.

In conclusion, comparison between experimental and Monte Carlo simulation results demostrates the applicability of the simulation code system PENELOPE for EPMA studies of layered structures. The results presented here clearly indicate that, with the aid of this simulation tool, the uncertainties of existing analytical quantitative procedures for layered systems can be significantly reduced (Merlet, 1998b).

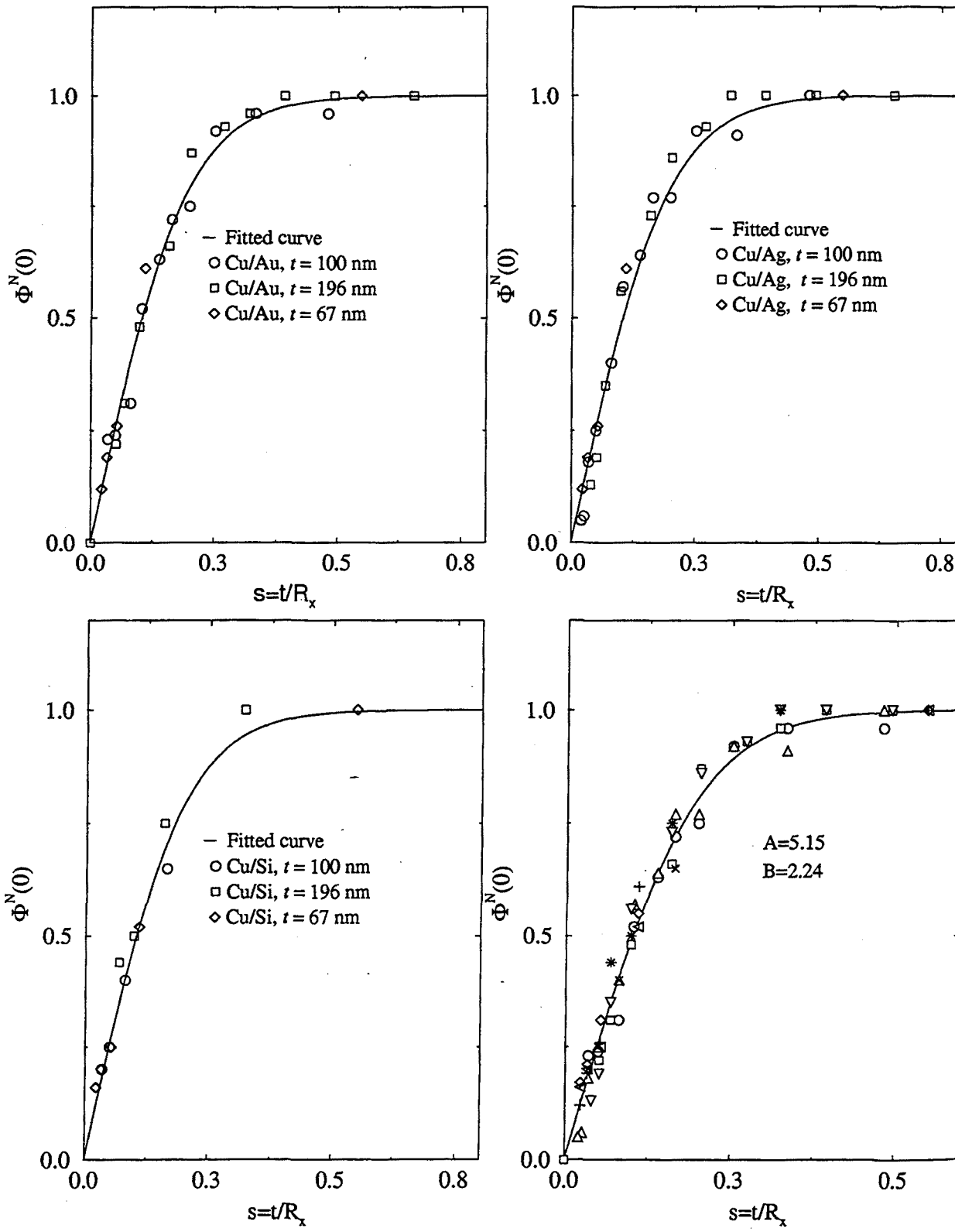

Figure 5.12: Scaled surface ionization as a function of the reduced depth for different film thicknesses and bombarding energies, for Cu/Au (a); Cu/Ag (b) and Cu/Si (c). Symbols are simulation results, as indicated in the figures. The continuous curves represents the function (5.19) with the parameter values indicated in Table 5.4. All simulation results are plotted together in (d), as well as the fitted curve using the mean values for the parameters A and B (see also Table 5.4).

5.5 Simulation of ionization distributions for layered targets

In this section we consider the simulation of ionization distributions in films-on-substrate targets, in order to clarify the influence of the substrate on the ionization in the film and viceversa.

Fig. 5.13 displays simulated $\Phi(\rho z)$ functions for Al K-shell in 100, 300, 500 and 800-nm-thick Al films deposited on B, Cu, Ag and W thick targets, at 10 keV electron incident energy. We can see that there is a marked influence of the substrate composition on the film ionization distribution. In general, the average number of ionizations per electron increases with the atomic number of the substrate. Evidently, this fact is direct consequence of the stronger backscattering in heavy elements. We can also see that the differences between the ionization distribution for the film and bulk material is maximum at the interface, where the influence of the substrate is higher, and it decreases as we move in the direction of the sample surface. For relatively thin films, the influence of the substrate also reaches the surface and thus the surface ionization will also increase for increasing substrate atomic numbers, as shown in the preceding section. For films of intermediate thickness, the point of maximum ionization gradually shifts to larger depths. Finally, for relatively thick films, backscattered electrons from the substrate are absorbed in the film before reaching the surface; in these cases, the surface ionization does not vary with the substrate atomic number. From the simulations of Fig. 5.13 we can see that ionization distributions in surface layers deviate markedly from those in homogeneous samples, especially when the atomic number of the film an substrates differ considerably. Thus, it seems rather difficult to reproduce realistically their shape and amplitude by using simple analytical functions, such as the ones used for homogeneous samples (see e.g. Merlet, 1998). Similar results have been reported by Amman and Karduck (1990) by using a completely different MC simulation algorithm.

Fig. 5.14 displays simulations of K-shell ionization in Al substrates covered by overlayers of B, Cu, Ag, and W, with different thicknesses (50, 100, 150 and 300 nm). The influence of the overlayer in the ionization of the substrate can be summarized as follows. For films with atomic number lower than of the substrate, the ionization distribution is quite similar to the corresponding part of the uncovered substrate. For increasing film thickness, a global shift of the distribution to greater depths is observed. When the film has an atomic number greater than the substrate a similar shift is observed in the opposite direction, i.e. towards the surface. This fact is a direct consequence of the increase of the transport mean free path in the film, i.e. the average angular deflection per unit path length, which increases with the target atomic number (see Fig. 1.2). The modification in the ionization distribution of the substrate due to the presence of the overlayer could be reproduced if we consider that the overlayer has the same atomic

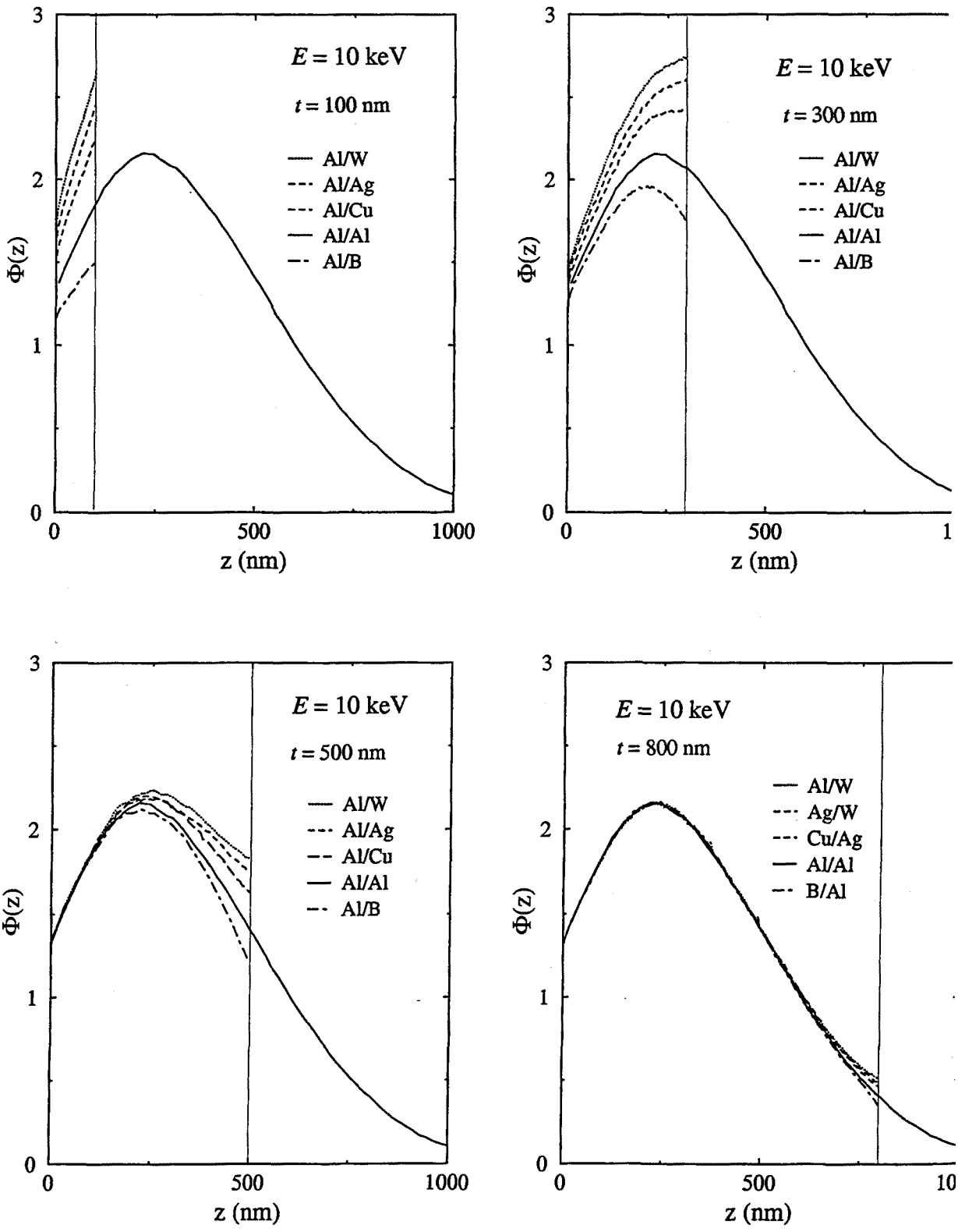

Figure 5.13: Simulated depth distribution of ionizations for 10 keV electrons in a Al films on semi-infinite B, Al, Cu, Ag and W substrates.

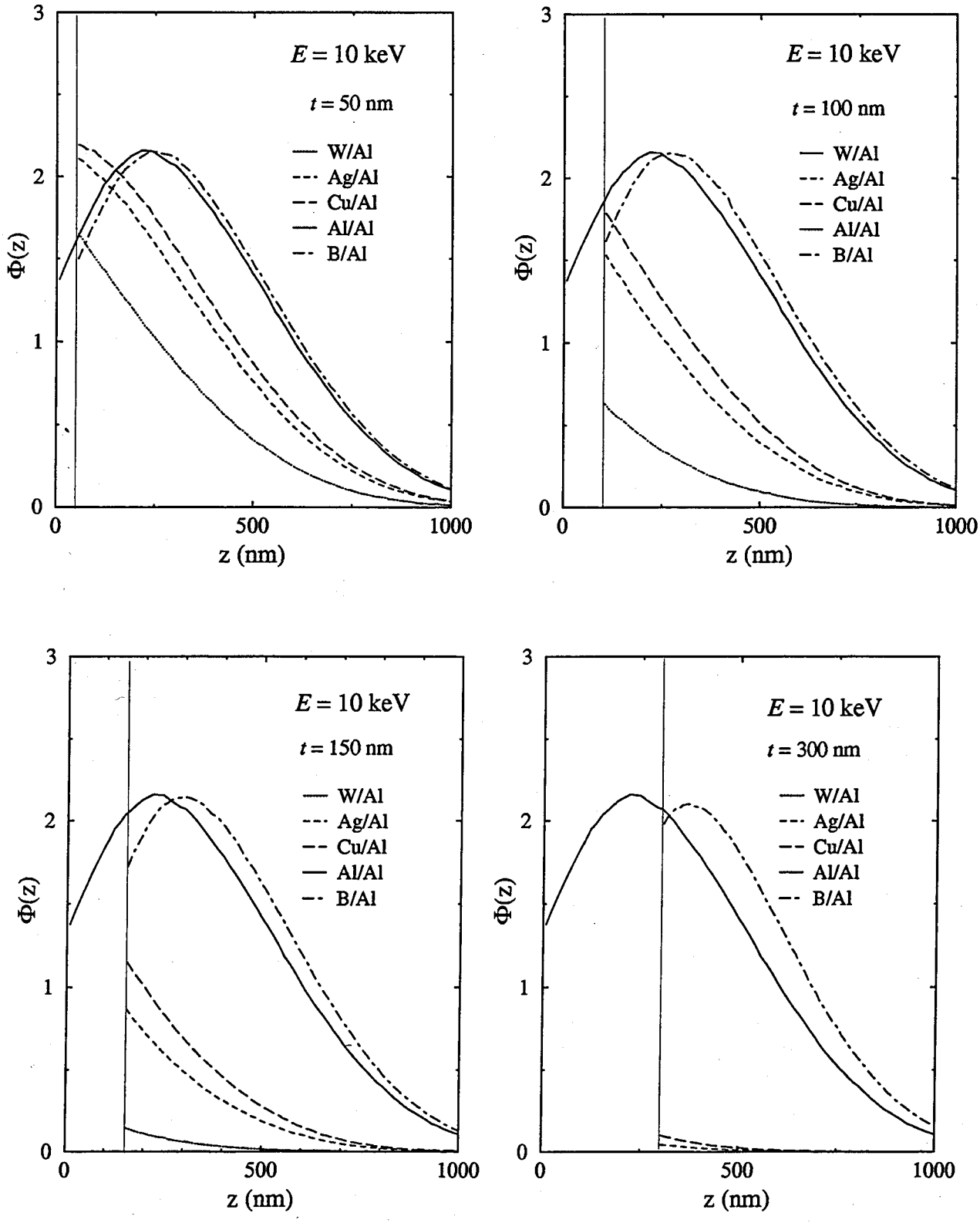

Figure 5.14: Simulated depth distribution of ionizations for 10 keV electrons in Al substrates covered with overlayers of B, Al, Cu, Ag and W.

number as the substrate, with an "effective" thickness. This effective thickness must be greater than the real one, for films with atomic number greater than the substrate. An study of the relationship between the effective thickness and the transport mean free path of the film material is in progress.

Fig. 5.15 shows simulated depth distributions of ionizations for a 200 nm thick Al film deposited on different substrates and covered with 50–nm–thick films of different materials. Obviously, the modifications of the ionization distribution for the immersed layer are a combination of both the influence of the overlayer and the substrate, described above. For such complex structures, MC calculation seems to be a unique tool to obtain the ionization distribution and to derive the composition and thicknesses (see e.g. Murata and Sugiyama, 1989).

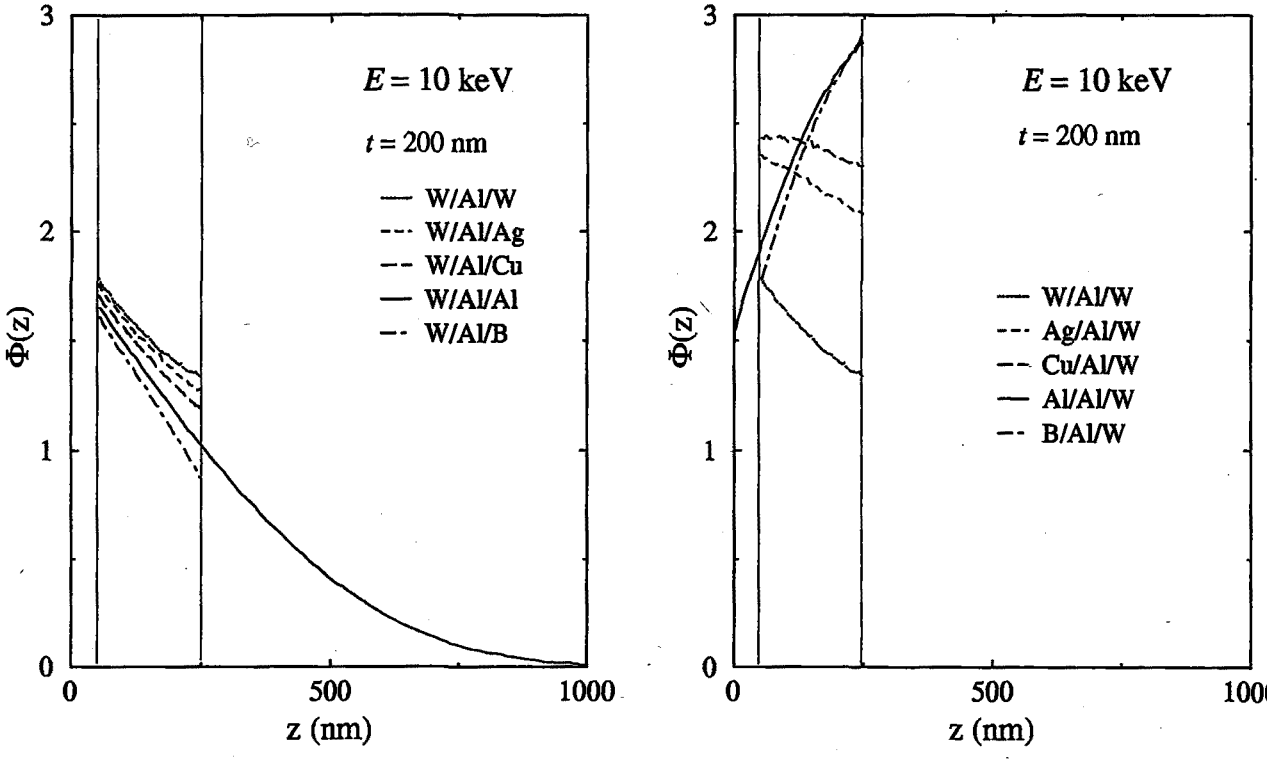

Figure 5.15: Simulated depth distribution of ionizations for 10 keV electrons in Al films on different substrates and covered by different films.

Chapter 6

X-ray emission spectra

Theoretical methods to compute accurate x-ray spectra emitted from thick targets bombarded with kV electrons are required for quantification in electron probe microanalysis (EPMA), x-ray fluorescence (XRF) and total reflection x-ray fluorescence (TRXRF). In EPMA, these computation methods are useful for spectral background subtraction, especially in the low-energy region, and for the development of procedures for quantitative analysis of small particles and rough surfaces. Calculated spectra are also useful in establishing the minimum detection limits for a specific sample (Fiori and Swyt, 1989) and to determine the efficiency of the x-ray detector. Last, but not least, reliable theoretical calculations help us to obtain a comprehensive understanding of the x-ray generation in the target, which is essential for the proper interpretation of measured data.

Many attempts to calculate bremsstrahlung spectra are based on the classical formula of Kramers (1923), e.g. the Kramers-Kulenkampff-Dyson (KKD) model (e.g. Storm, 1972). Ambrose et al. (1991) and, more recently, Goel and Shanker (1996) have measured x-ray spectra and have shown that the KKD does not accurately describes their experimental data. Ambrose et al. (1991) have proposed the use of the bremsstrahlung cross sections of Kissel et al. (1983), integrated over the target thickness assuming the CSDA and correcting for electron backscattering and photon attenuation, to compute bremsstrahlung spectra. Although this approach provides a substantially better prediction of the photon-energy dependence of the bremsstrahlung spectra than the KKD model, results are not satisfactory. Semi-empirical approaches, based on x-ray spectra measurements, have also been proposed which are generally successful within their range of interest (Pella et al., 1985; Small et al., 1987; Trincavelli et al., 1998).

X-ray spectra have been computed from the numerical solution of the transport equation by Brown and Gilfrich (1975). However, this kind of solution is only possible for relatively simple interaction models and planar geometries. Simulations of the continuous component of x-ray spectra have been carried out by Statham (1976) and Heckel and Jugelt (1983), and more recently by Ding et al. (1994). Similar Monte

Carlo simulations have been reported by Araki et al. (1993), who included charact istic lines. Gauvin et al. (1992) have used Monte Carlo simulation results to deri calibration curves for quantitative analysis of particulate matter. In these cases, on the electron transport was considered. X-ray absorption and secondary x-ray fluor cence were taken into account by simply assuming exponential attenuation inside t sample. This procedure is only approximate and, moreover, it is difficult to generali to complex geometries, e.g. particulate materials or embedded inclusions (Gauvin al., 1992). This difficulty is overcome here by simulating the transport of both electro and photons; complex geometries can thus be handled easily, and accurately, with t aid of available geometry packages.

In this chapter we describe a Monte Carlo simulation code to compute x-ray spectr The DCSs for inner-shell ionization and bremsstrahlung emission have been described detail in chapter 1. In section 6.2, we describe the simulation algorithm regarding inne shell ionization and bremsstrahlung emission processes. In section 6.3, we describe tl experimental setup and the reduction of measured x-ray spectra to an absolute scale. section 6.4, simulation results are compared with measured spectra. Section 6.5 contai a discussion of the reliability and limitations of the present physical models for practic application in EPMA. Finally, the code is applied to the calculation of the detect efficiency for wavelength-dispersive spectra.

6.1 Generation of x-ray spectra

We have previously shown that PENELOPE describes the transport of kV electron well and, therefore, the generated electron trajectories can be considered as numerica replicas of actual tracks. Therefore, we can evaluate the spatial distribution of emitte characteristic x-rays without altering the simulation routines. The only information w need is the total ionization cross section of the shell of interest as a function of th electron energy, which determines the probability of ionization along each segment o an electron track generated by PENELOPE.

A computer code has been written that performs Monte Carlo simulation of electron photon showers by using the PENELOPE code system and provides the x-ray spectra at a given direction. The code incorporates the improved angular bremsstrahlung dis tribution (see chapter 1). Changing to this improved angular distribution required th modification of the original PENELOPE package.

6.1.1 Simulation of characteristic x-ray emission

PENELOPE generates electron tracks as a series of "free flights" between consecutive (soft and hard) interactions. Along each free flight, the energy E of the electron is assumed to stay constant. To simulate the generation of characteristic x-rays, which result from vacancies produced in a K-shell, we proceed as follows. For each free flight, we calculate the probability that an ionization has been produced in the considered shell, which is given by

$$P_{\rm ion} = s\,\mathcal{N}\,\sigma_{\rm i}(E), \tag{6.1}$$

where s is the length of the free flight and $\mathcal{N}$ is the density of atoms of the considered (ionized) element per unit volume. After computing the ionization probability, we sample a random value ξ uniformly in (0,1) and consider that the interaction is effective only when $\xi < P_{\rm ion}$. When an ionization occurs, its position is sampled uniformly along the free flight. As the probability of ionization in a free flight is much less than unity, this procedure gives the correct average number of ionizations per unit path length.

Excited ions relax to their ground state by migration of the initial vacancy to outer electron shells, which proceeds through emission of fluorescent x-rays or Auger electrons with characteristic energies. Our code, as well as PENELOPE, simulates the emission of characteristic x-rays that result from vacancies produced in a K-shell. We consider only characteristic photons emitted in the first stage of the de-excitation cascade, i.e. when the initial vacancy in the K-shell is filled by an electron from an outer shell. The probability that a radiative de-excitation occurs is obtained from the fluorescence yields tabulated by Fink and Rao (1974). The considered characteristic photons are Kα and Kβ, with relative probabilities obtained from the line fractions given by Khan and Karimi (1980). Characteristic x-rays are assumed to be emitted isotropically.

To improve the efficiency of the simulation, we apply interaction forcing (see e.g. Bielajew and Rogers, 1985) This consists of artificially increasing the probability of ionization along a free flight, say to a value $P_{\rm for}$. To compensate for this increase of probability, characteristic x-rays emitted in the forced interaction are given a weight $\omega = P_{\rm ion}/P_{\rm for}$ less than unity. This manipulation does not alter the computed spectra, but the statistical uncertainties (for a given calculation time) are substantially reduced. In the calculations, we adopt a value of $P_{\rm for}$ such that, on average, 0.1 forced ionizations occur in each free flight.

6.1.2 Simulation of bremsstrahlung emission

Since bremsstrahlung emission by keV electrons is a low probability process, we again apply interaction forcing to reduce the statistical uncertainties. In this case, we multiply the bremsstrahlung inverse mean free path by a factor $\mathcal{F} > 1$ and, to compensate for

this, bremsstrahlung photons, and all their descendent radiations, are assigned a weight $\omega = 1/\mathcal{F}$. The factor $\mathcal{F}$ is chosen in such a way that the reduced inverse mean free path is of the order of 1/5 of the electron range. This ensures that a mean number of 5 bremsstrahlung photons per primary electron are produced.

6.2 Experimental method. Absolute spectra

Thick targets, pure elements and compounds, have been irradiated with 20 and 30 kV electron beams at normal incidence using the electron microprobe CAMECA SX-50. Spectra of emerging x-rays have been obtained by using the PGT IMIX energy dispersive spectrometer, which is located in a direction forming an angle of 40° with the sample surface. The emerging photon beam has been collimated with a diaphragm (300 μm in diameter) placed in front of the beryllium window, at 53 mm from the target. This avoids spurious x-ray peaks caused by electrons backscattered onto the pole-piece of the final lens of the microscope column and other objects near the specimen. Probe currents have been measured with a Faraday cup placed on the sample holder, and have been chosen so as to yield a counting rate below 500 counts per second, thus minimizing pulse pile-up effects. Typical acquisition times were 3000-4000 s.

Acquired x-ray spectra have been converted to absolute intensity units, i.e. number of photons emitted per unit energy interval and unit solid angle per incident (bombarding) electron. It is worth pointing out that measurements in absolute units serve as the most stringent test of the physical parameters used in the simulation algorithm, although they may contain systematic uncertainties. The conversion of the acquired spectra to absolute intensity is made by using the equation

$$N(E) = \frac{N_{\mathrm{ch}}}{N_{\mathrm{e}}\, \epsilon(E)\, \Delta\Omega\, \Delta E}, \tag{6.2}$$

where N_{ch} is the number of counts in a particular photon energy channel, N_{e} is the total number of incident electrons, $\Delta\Omega$ is the solid angle subtended by the x-ray detector, ΔE is the width of the energy channel and $\epsilon(E)$ is the detector efficiency, which is a function of the photon energy.

The number of incident electrons N_{e} has been evaluated by multiplying the target current I_0 by the acquisition time t. We recall that the electron microprobe has a built-in continuous beam current monitoring and feedback system, which stabilizes the beam current to 0.3 %. The calculated number of incident electrons is estimated to have less than 2% uncertainty. The width of the photon energy channel ΔE of the spectra is given by the computer of the PGT IMIX system. The high energy part of the x-ray spectrum (bremsstrahlung tip) has been used to verify the accelerating potential values. The solid angle $\Delta\Omega$ has been computed as A/d^2, where A is the area of the entrance aperture of

the collimator, and d is the distance between the sample and the collimator. Using the values for A and d given by the manufacturer, the uncertainty in $\Delta\Omega$ is estimated to be less than 2%.

As we have seen in chapter 3, the efficiency of a typical Si(Li) x-ray detector is essentially unity over a wide photon energy interval (~3-15 keV). It takes lower values at low photon energies, due to absorption in the different inactive layers in front of the intrinsic zone, and at high energies, due to partial transmission through the intrinsic zone. In general, the efficiency can be evaluated by using radioactive sources of known activity (Shima, 1979), well-calibrated fluorescence sources or synchrotron radiation (Krumrey et al., 1989), and/or theoretical methods (Weathers et al., 1991). As a first approximation, $\epsilon(E)$ can be computed by assuming exponential attenuation of the photon beam in the inactive layers and in the intrinsic zone. However, this approach may be seriously erroneous due to the following reasons. Firstly, the different layers are generally non-uniform (see e.g. Reed, 1993) and their average thicknesses are poorly known. Secondly, absorption of photons with moderately high energy in the inactive layers produces secondary radiation (photoelectrons and x-rays) that may yet reach the active zone. Recently, Lépy et al. (1997) have shown that the so-called silicon "dead layer" acts as a partially active layer, the corresponding events being recorded in the peak tail. Finally, uncertainties of adopted attenuation coefficients also affect the estimated efficiency.

Assuming, for a moment, that simulated spectra are reliable (see below), one can use them to analyze the consistency of calculated efficiencies. We have tentatively evaluated the efficiency $\epsilon(E)$ by considering purely exponential attenuation and using the detector layer thicknesses given by the manufacturer. Fig. 6.1 shows the comparison between raw experimental spectra, i.e. without detector efficiency correction, and simulated x-ray spectra. We can see that the agreement between simulation and experiment is satisfactory from ~3 keV up to the displayed energy, 8 keV, and also from ~10 keV up to ~15 keV. The energy region between ~8-10 keV has not been displayed because it contains the characteristic Cu peaks. This direct comparison of simulated spectra with experiment confirms that the efficiency is close to unity for photons with energy in the interval from ~3 keV up to ~15 keV, as predicted by the simple calculation (see chapter 3). However, this calculation underestimates $\epsilon(E)$ at lower energies, and overestimates it at higher energies, justifying the presence of the aforesaid sources of error. To get at least a rough estimate of $\epsilon(E)$ for the complete energy range of interest, we have computed it by considering absorption only in the most significant passive layer, i.e. the Be window, and using an effective value for the crystal thickness (1.5 mm), as suggested by the work of Paterson et al., 1989). With this method one gets efficiencies that are accurate to within ~5% for energies between 3 and 15 keV and "plausible" outside this range. Therefore, comparison of simulated and measured spectra is meaningful for $E = 3 - 15$ keV and only indicative for lower and higher energies. Notice that, if we

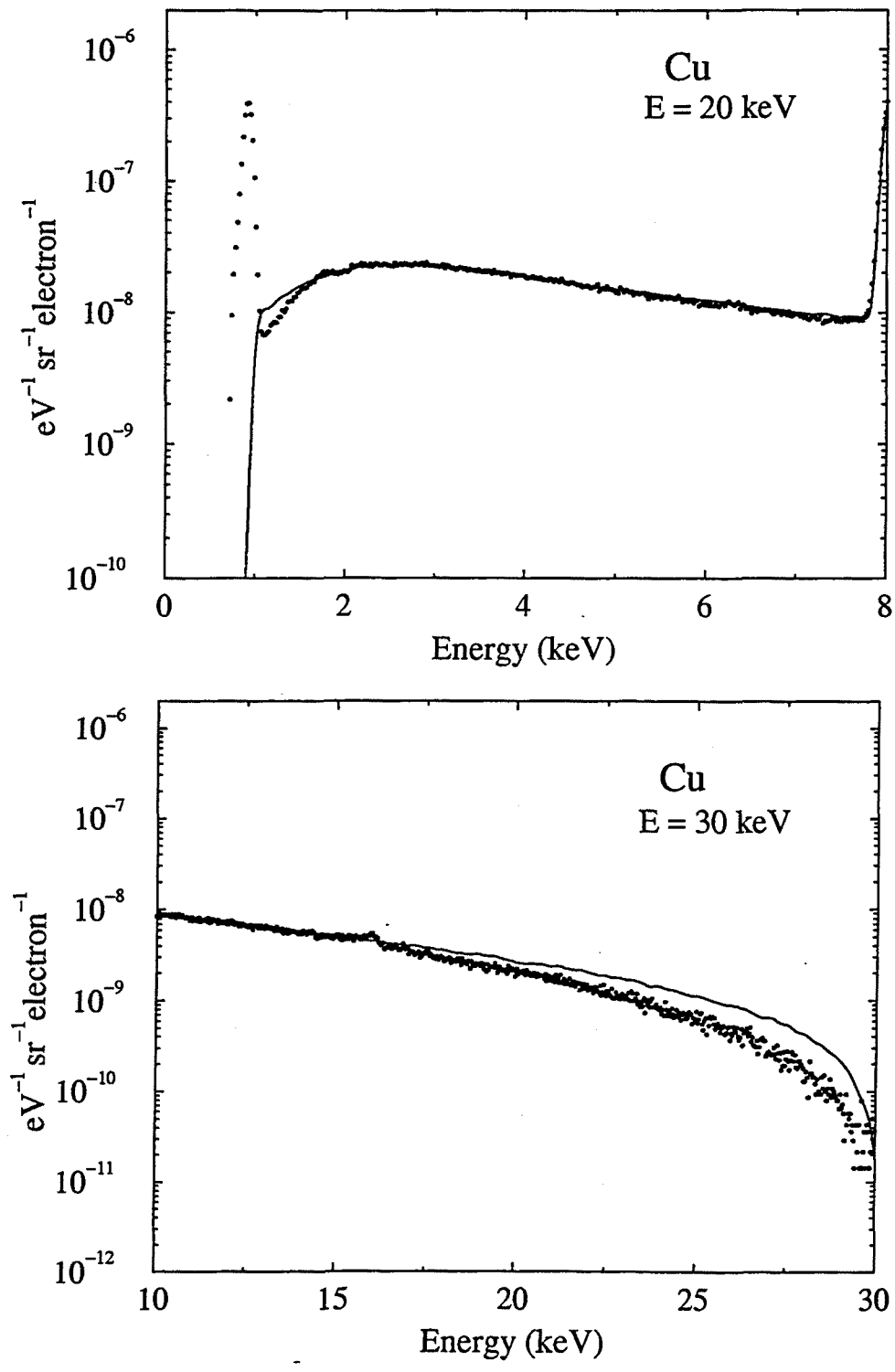

Figure 6.1: Direct comparison of simulated (solid line) and experimental (dots) x-ray spectra for bulk copper with excitation energies of 20 keV (a) and 30 keV (b). Experimental data were not corrected for detector efficiency.

assume that the simulation results are reliable, the calculation of the detector efficiency is straightforward from Eq. (6.2). This method has been suggested by several authors (e.g. Weathers et al., 1991).

Finally, uncertainties from counting statistics range typically from 3 to 6% in the continuous component of the spectra, and 1-2% in the characteristic peaks. Other sources of uncertainty, such as errors in the estimate of the take-off angle and target uniformity, are considered to be negligible. The various error contributions discussed above lead to an overall uncertainty of 5-7% for the experimental absolute spectra.

6.3 Comparison of simulated and measured spectra

Energy distributions of x-rays emitted from the specimen in directions close to that of the detector have been simulated using the code described above. To account for the response of the detector, Monte Carlo spectra have been convoluted with a Gaussian distribution with an energy-dependent Full Width at Half Maximum (FWHM). The dependence of the FWHM on incident photon energy has been estimated by measuring x-ray spectra for different pure specimens, whose characteristic x-ray energies span the region between 1 and 10 keV (see chapter 3). Simulated spectra have been normalized to one incident electron to make them directly comparable to measured absolute spectra.

Simulated and experimental spectra, at incident electron energies of 20 and 30 keV, for Cu and Ag metallic targets, are compared in Figs. 6.2 and 6.3. It can be observed that the agreement is, in general, satisfactory in the "meaningful" region between 3 and 15 keV. The calculation also describes the continuous component of the spectra accurately, even in regions where uncertainties in $\epsilon(E)$ may be somewhat larger. For Ag, the peak at approximately 3 keV corresponds to $L\alpha$ x-rays, that are not simulated by the present version of the code. The code, however, does give a realistic description of the spectral background below this peak, thus providing valuable information for background subtraction in quantitative analysis. The Cu $L\alpha$ line also appears in the Cu spectra. Furthermore, the experimental Cu spectra at 30 keV shows a small sum peak.

When comparing simulations with experimental data, we must recall that there are various detection artifacts, such as incomplete charge collection, pulse pile-up and sum peaks (Statham, 1981), which cannot be totally avoided, and whose effects are not taken into account in the simulations. These effects, combined with the uncertainty of the adopted ionization cross sections, originate small discrepancies in the characteristic peaks. It should also be noted that, due to incomplete charge collection, the low-energy end of the spectrum accumulates degraded counts from all higher energy x-rays, especially in the 0-3 keV region (Statham, 1981). We think that this effect could contribute to the "high" detector efficiency found in this region.

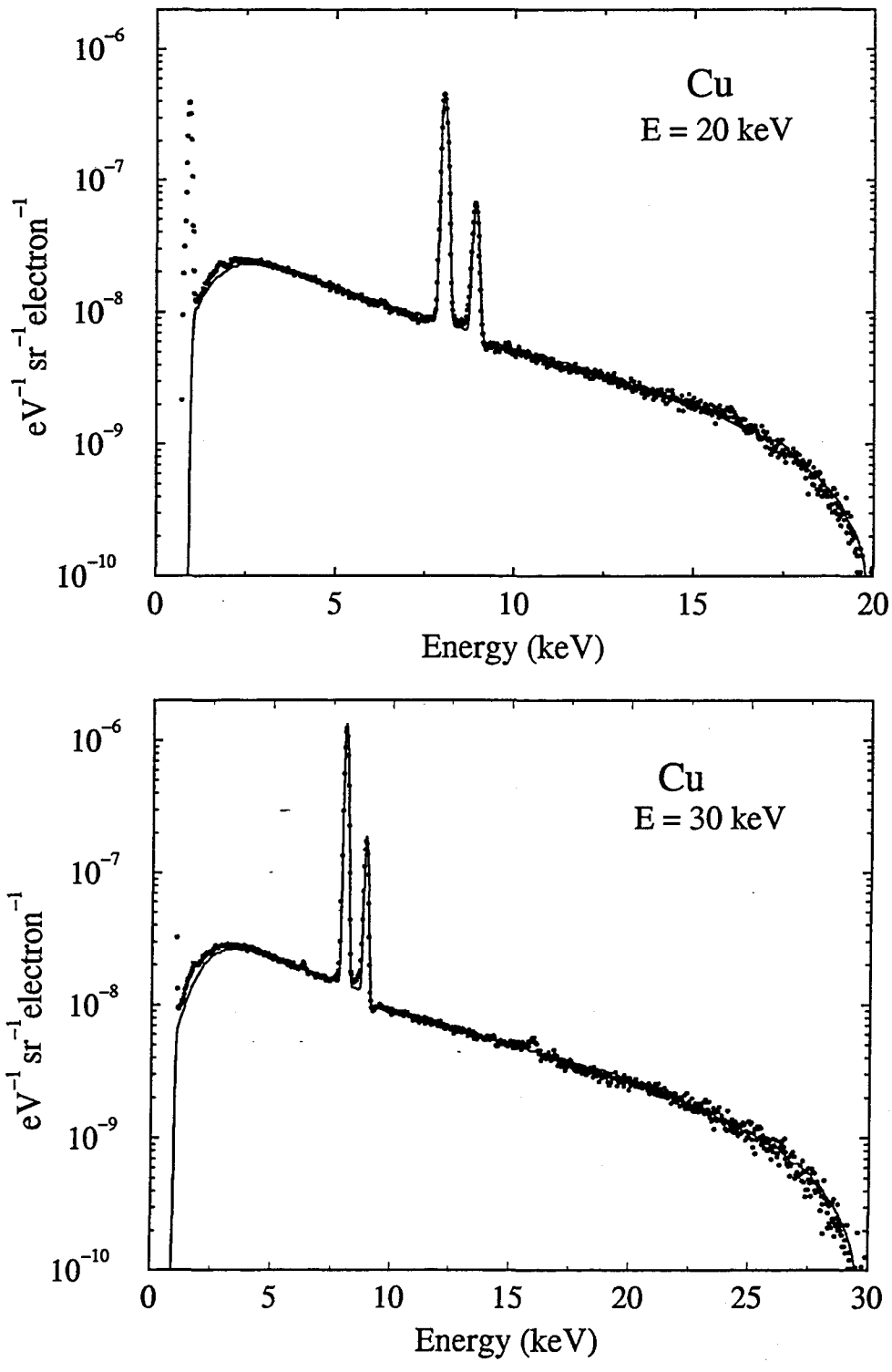

Figure 6.2: Comparison of simulated (solid line) and experimental (dots) x-ray spectra for bulk copper with excitation energies of 20 keV (a) and 30 keV (b).

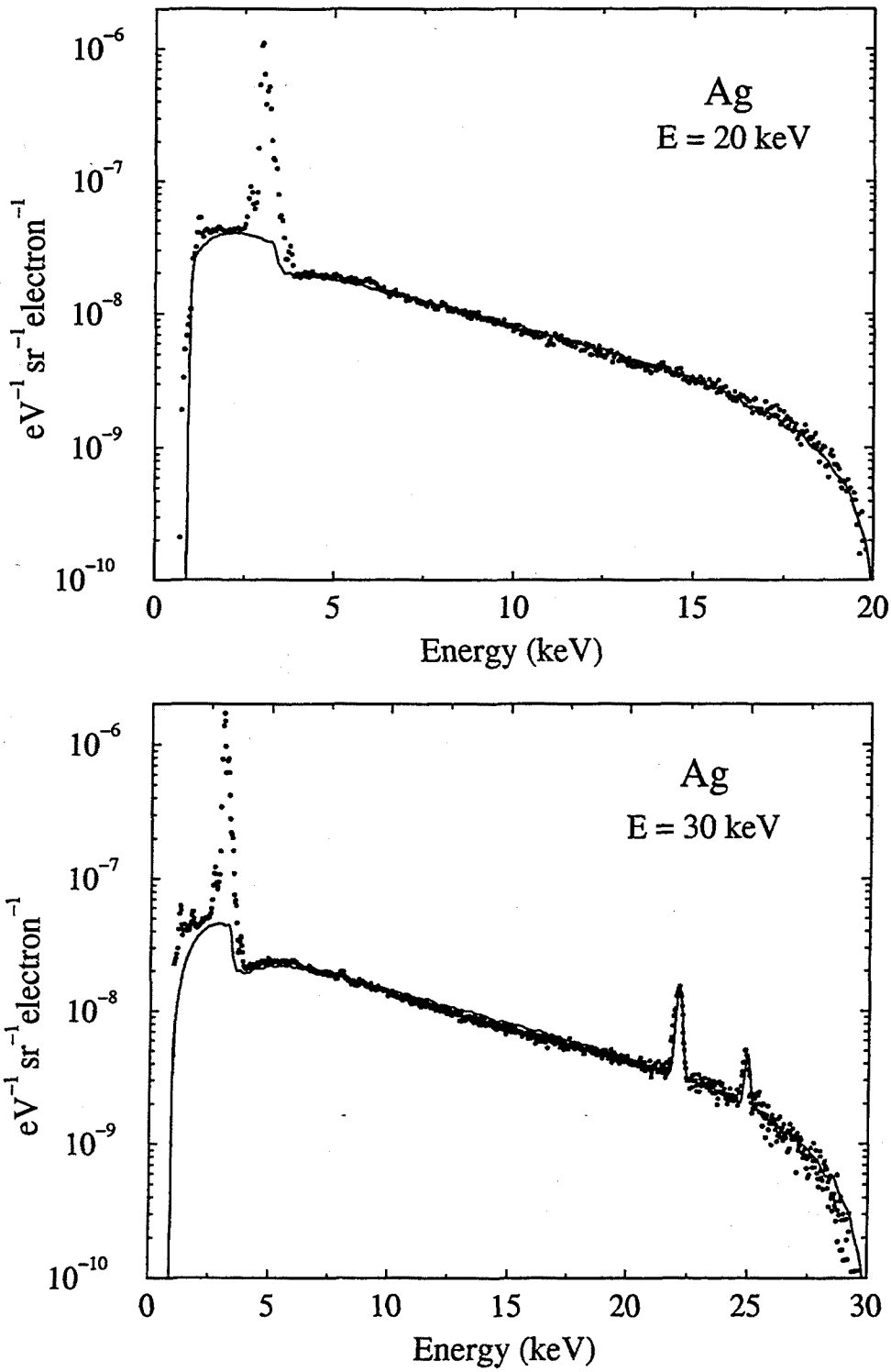

Figure 6.3: Comparison of simulated (solid line) and experimental (dots) x-ray spectra for bulk silver with excitation energies of 20 keV(a) and 30 keV(b).

Fig. 6.4 displays spectra obtained at incident electron energies of 20 and 30 keV from Fe-Cr-Ni alloy (Standard Reference Material 479a, certified by the National Bureau of Standards), with weight concentrations of 71, 18.1 and 10.9%, respectively. Although characteristic peaks again show small discrepancies, duplicating the differences found for pure targets, the agreement between simulation and experiment is again satisfactory. This indicates that the implemented method works correctly not only for pure but also for multielement samples.

Monte Carlo simulation of electron-photon showers can be used to study secondary fluorescence produced by bremsstrahlung photons and characteristic x-rays produced elsewhere in the sample. This extra radiation is difficult to account for by analytical procedures. While generally this is a minor contribution to the total x-ray emission, secondary fluorescence can be an important issue in particulate matter, when the electron beam is near a phase boundary. Figure 6.5 shows a comparison between complete simulated spectra for ZnS target and the simulation of same target disregarding ionizations produced by electron impact. It is seen that although electron impact ionization has not been taken into account, there is an important count rate at the characteristic line energies due to continuum fluorescence. Therefore, Monte Carlo simulation of electron-photon showers can be effectively used to validate analytical models describing the continuum fluorescence contribution, which is impossible to discriminate experimentally. Successful application of the developed code as regards secondary fluorescence estimation in small Cu-particles in Fe-containing slag has been recently described by Heikinheimo and Jalkanen (1998).

It can be concluded that the physical models presented here offer a consistent description of x-ray spectra generated by kV electron beams. The developed code is well suited to compute x-ray spectra from elemental and compound targets, and is a valuable tool for quantitative microanalysis.

6.4 Application to other geometries

In this section, we give a few examples of the application of the developed code to other geometries such as multilayered targets and oblique incidence.

Fig. 6.6 displays spectra obtained at incident electron energies of 20 keV from multilayered targets consisting of 2–nm–thick Ni films deposited on 40.5–nm–thick Cu films deposited, in turn, on bulk Cr and Ag, respectively. We can see that characteristic peaks, especially for Ni, show discrepancies with experiment. These discrepancies could be attributed to the uncertainties of the thickness estimation. The simulation is seen to predict the shape of the spectral background accurately in the energy range 3-15 keV, where the uncertainty in $\epsilon(E)$ is small. This comparison confirms again the validity of

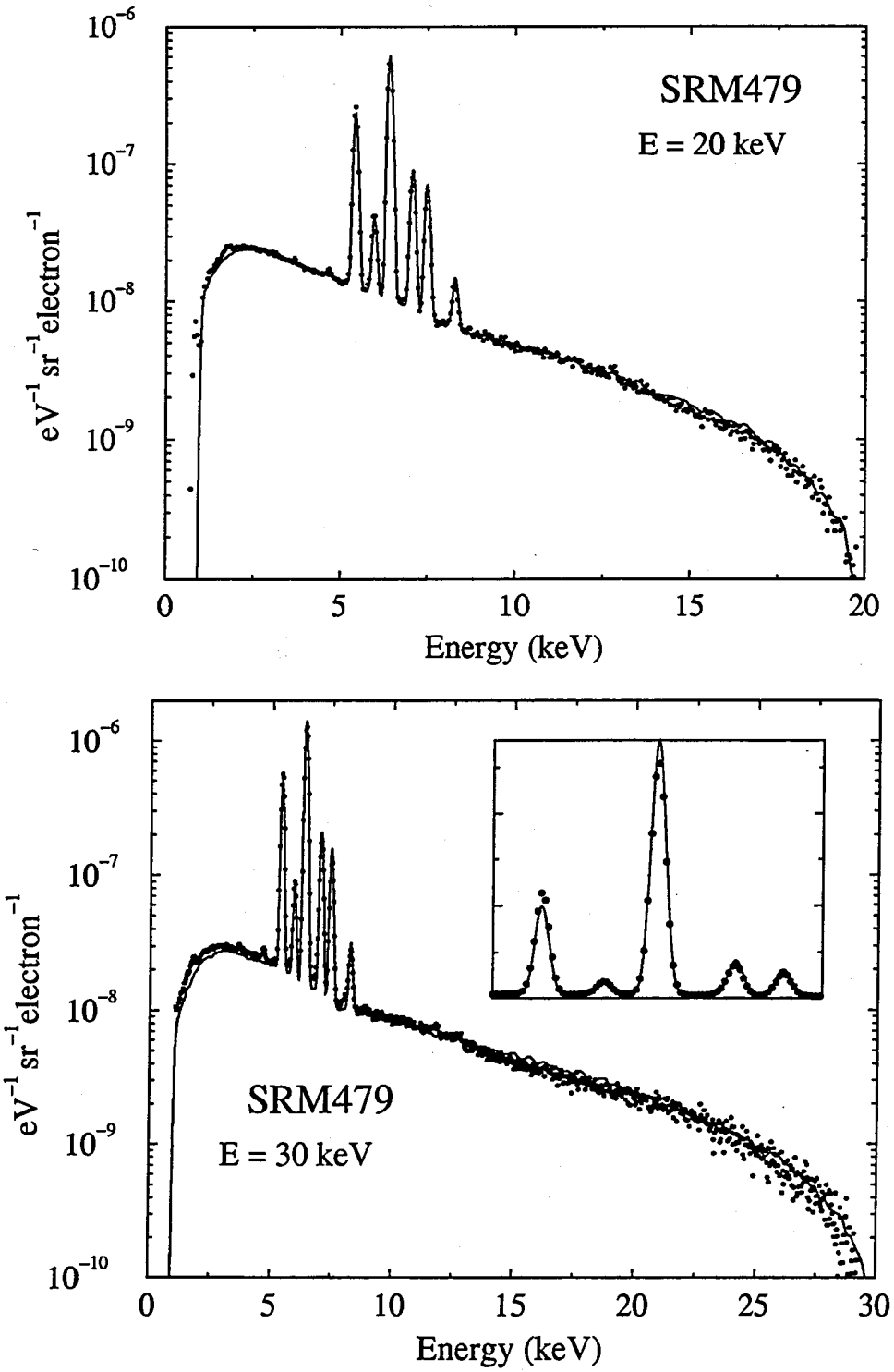

Figure 6.4: Comparison of simulated (solid line) and experimental (dots) x-ray spectra for SRM479a NBS certified standard, with excitation energies of 20 keV and 30 keV.

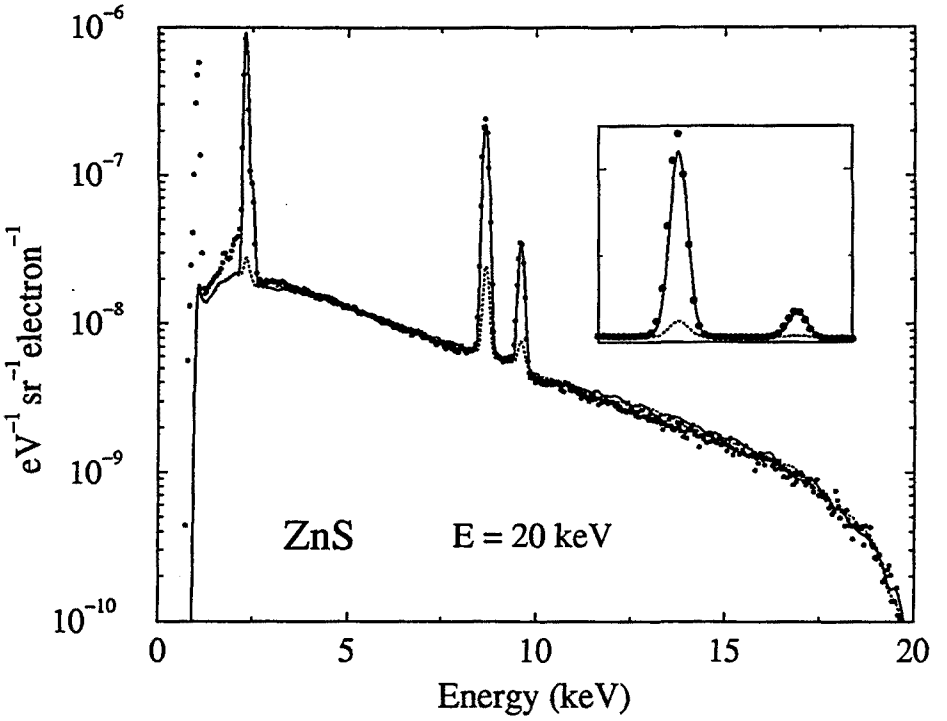

Figure 6.5: Comparison of experimental x-ray spectra (dots) and simulations of complet spectra (solid line) and simulation without electron impact ionization (dashed line) for bul ZnS with an excitation energy of 20 keV.

the simulation procedure as regards the crossing of an interface between two material

Fig. 6.7 sets out measured and calculated spectra for a 98 $\mu g/cm^2$ thick Cr filr deposited on a silicon wafer. These were obtained with 19 kV electron beams at norma incidence and at an angle of 30 deg relative to the surface normal. The thickness of th Cr film was determined by previous electron microprobe measurements, with an esti mated relative error of about 5%. It can be seen that even for thin samples, where th number of interactions is small, the agreement with the experiment is satisfactory. I this case, a JEOL JSM840 scanning electron microscope equipped with a LINK AL1000 energy dispersive spectrometer was employed, allowing the possibility of recording th spectra in oblique incidence. Special care has been taken to determine the energy tha the beam electrons actually have when entering the sample. Unfortunately, in this cas conversion to absolute units was not possible due to the lack of knowledge about the rea area of the detector (and without the possibility of placing an aperture in front). In thi case, simulated spectra have been re-scaled so as to match the measured spectra in a region free of characteristic peaks. The energy-dependent FWHM was also experimen tally evaluated and the simulated spectra properly convoluted to take into account th detector response. Finally, it is worth recalling that scanning electron microscopes are in general, not equipped with beam regulator devices, therefore acquisition times can not be very large. For this reason measured spectra may be affected by large statistica fluctuations.

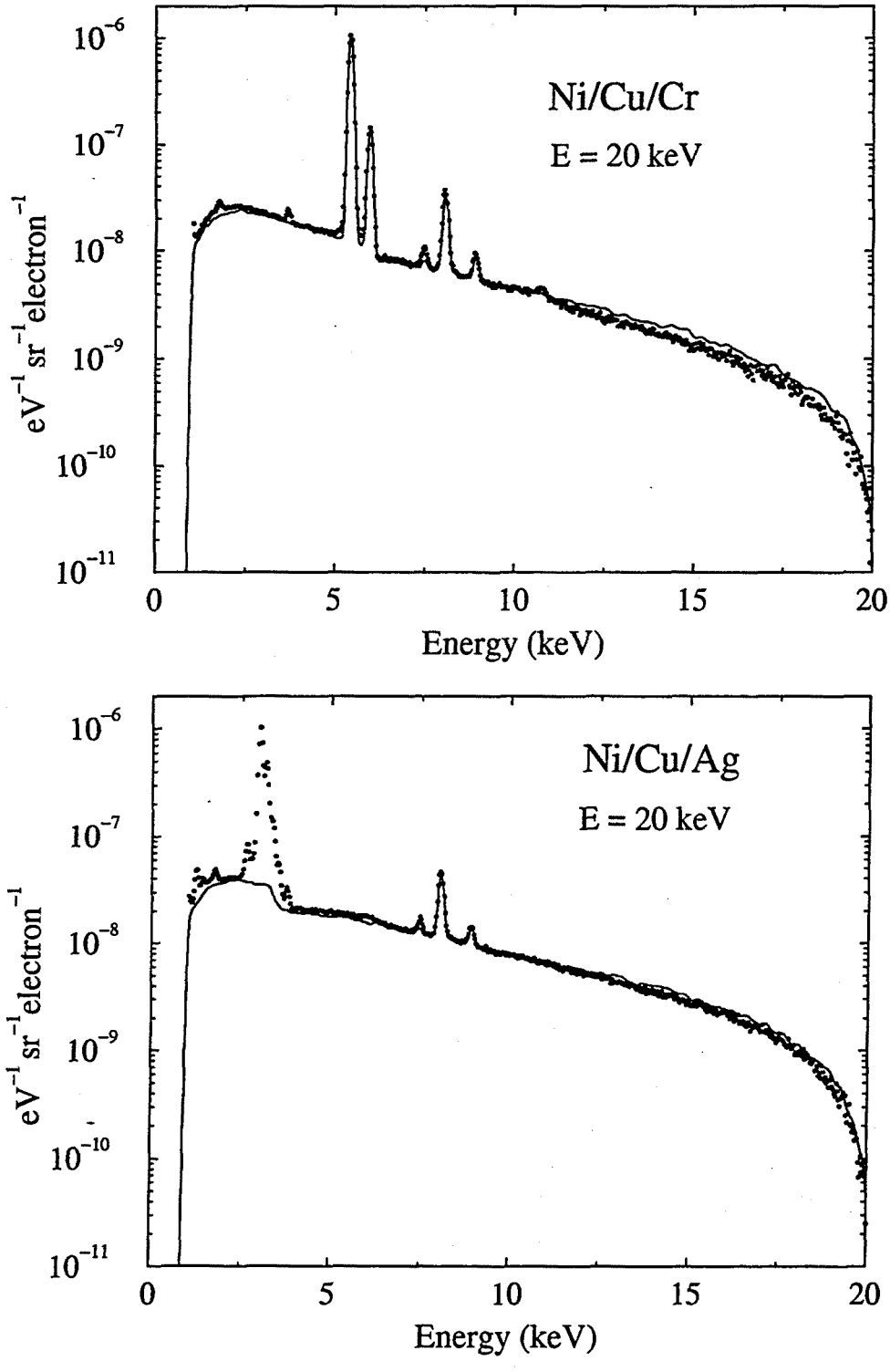

Figure 6.6: Comparison of simulated (solid line) and experimental (dots) x-ray spectra for multilayered structure consisting of Ni/Cu/Cr (a) and Ni/Cu/Ag (b). The thickness of the Ni and Cu layers are estimated to be 2 nm and 40.5 nm, respectively.

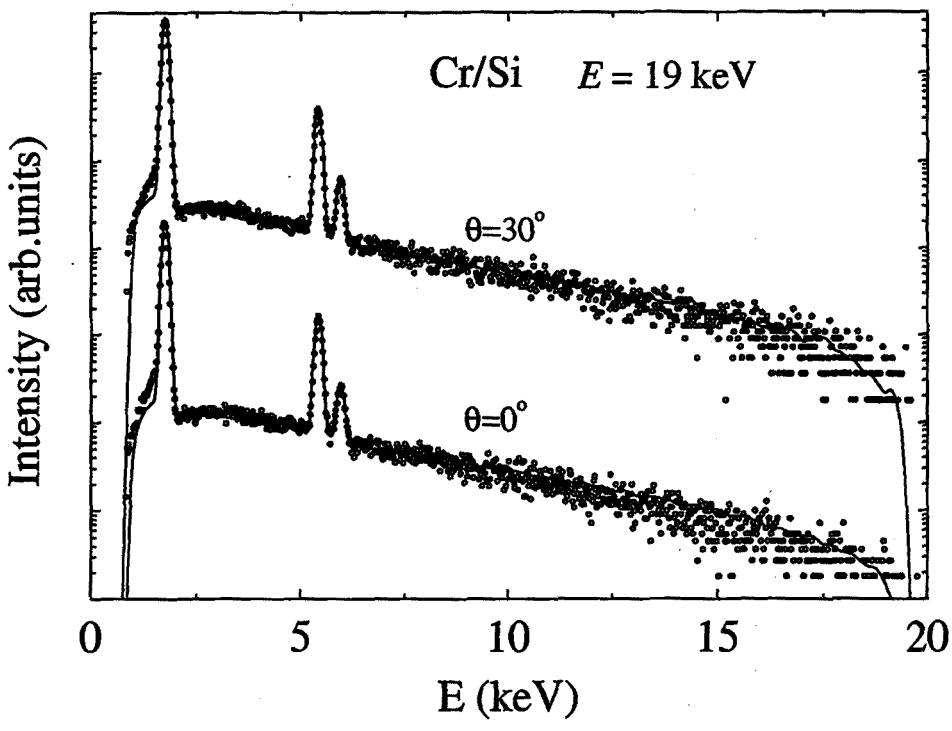

Figure 6.7: Simulated and experimental X-ray spectra for a composite sample consisting of a 98 $\mu g/cm^2$ chromium film on a silicon wafer, for a 19 kV electron beam with the indicated angles of incidence.

It is to be expected that the x-ray spectra vary with the angle of incidence. In particular, the peak-to-background ratio will increase with increasing tilt angle. This is mainly due to the fact that radiation originated in the zone near the surface is lost, affecting characteristic and bremsstrahlung radiation in different ways. The good agreement found for non–normal incidence is a good reason to believe that the bremsstrahlung angular distribution model adopted correctly describes this process.

The availability of reliable peak–to–background ratios may well lead to improvements in the results obtained in the characterization of rough surfaces, small particles or inclusions. Some of the existing models for analyzing the latter (Armstrong, 1991) are based on the use of these intensity ratios, but assuming that their value is the same in a small particle as in a bulk sample. This is a major drawback in the mentioned method which could be overcome with the use of peak to background ratios obtained from simulation of the particles. The possibility of reproducing the x-ray spectrum provides a unique and powerful tool which enables new possibilities for the solution of analysis problems not yet solved in a closed manner.

6.5 Determination of detector efficiency

The determination of the detector efficiency is needed for quantitative x-ray spectrometry in many different fields, such as x-ray astrophysics, or materials characterization techniques. In EPMA, knowledge of the detector efficiency is required in standardless methods of analysis. Traditionally, standardless methods use EDS rather than WDS, since the efficiency of the latter is difficult to calculate.

Smith and Reed (1981) estimated the relative efficiency of a WDS, with LiF crystal, by comparing experimental x-ray spectra with calculated spectral distribution, over the same background region. Wernisch (1985) estimated the relative efficiency of a WDS, with LiF and PET crystals, by comparing calculated count rates with measured count rates of integrated K or L pure-element spectra. In both cases, calculations were performed by relatively simple, analytical formulas. One advantage of the first approach is that a continuous efficiency curve as a function of x-ray energy is obtained with a single measurement, while the second method requires different measurements at discrete photon energies. A second advantage is that the first method requires bremsstrahlung cross sections, which can be obtained with relatively good accuracy (see chapter 1), while the second method uses ionization cross sections that are affected by large uncertainties. The disadvantage is that experimental measurement of background is affected by statistical uncertainties larger than in the measurement of characteristic peaks, especially when one uses the WDS. In this section, we have followed an approach similar to that of Smith and Reed (1981). We have calculated the required spectral distribution by using the developed MC code and we have compared them with measured absolute x-ray spectra.

Let $P(E)\,\mathrm{d}E$ denote the theoretical number of photons with energies between E and $E + \mathrm{d}E$ emitted by the target. The efficiency evaluated at the wavelength channel corresponding to $\lambda_i = hc/E_i$ is obtained by the relation

$$\epsilon(\lambda_i)\,\Delta\Omega = \frac{N_i \Delta\lambda}{\int_{E(\lambda_i+\Delta\lambda)}^{E(\lambda_i)} P(E)\mathrm{d}E}, \tag{6.3}$$

where $\Delta\lambda$ is the width of wavelength channel, and N_i is the number of photons detected at the channel $(\lambda_i, \lambda_i + \Delta\lambda)$ per incident electron.

Fig. 6.8 displays the absolute efficiency of a WDS, with LiF and PET monochromator. These efficiencies were obtained by comparing experimental x-ray spectra of pure Zr and Cu targets acquired at 20 keV electron incident energy, using the LiF and PET crystals, with simulated spectra of the same targets and irradiation conditions. We can see that the efficiency of the WDS is not constant as happens for EDS; in general, it increases continuously with increasing x-ray energy. This variation is more important in the case of the PET monochromator. For the LiF monochromator, the increase is

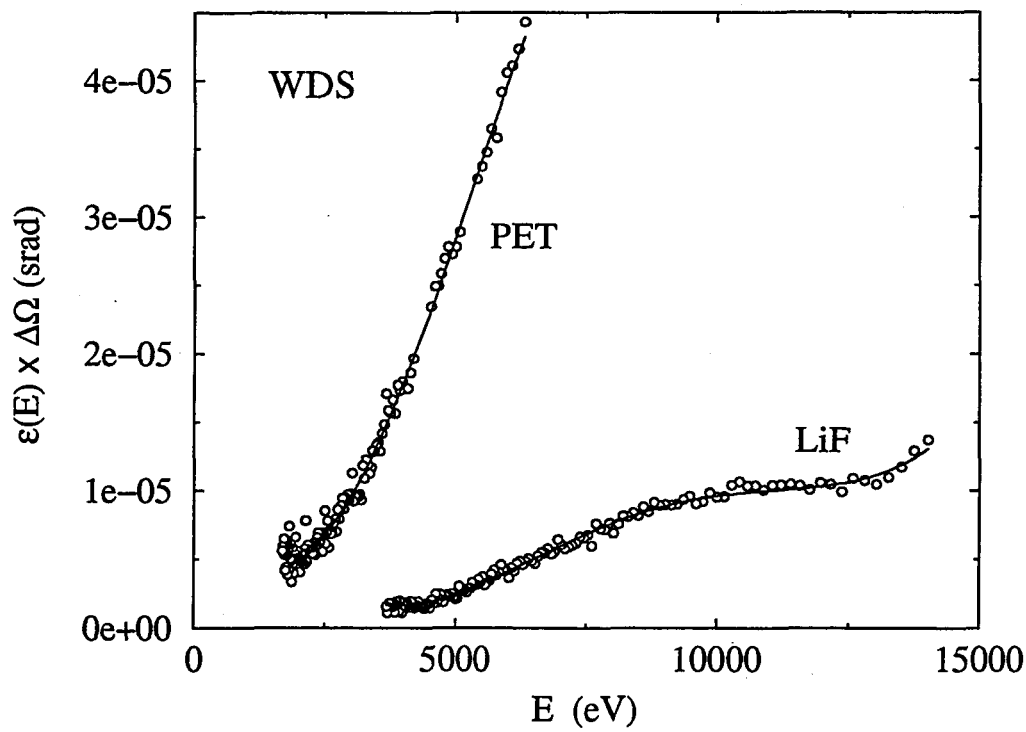

Figure 6.8: Dependence of the detection efficiency of a WDS with LiF and PET crystals Dots are estimated efficiencies; continuous curves represent a polynomial fits of 3rd order, fo the PET, and 4th order, for the LiF.

smoother and it changes the curvature at ~5 keV and at ~12 keV. The increase of th efficiency for increasing x-ray energy will deviate the spectral background shape fron the typical bremsstrahlung shape found in EDS spectra. At the same time, we can se that the efficiency of PET is always higher than that of LiF. This could be expecte from its lower spectral resolution (see chapter 3).

The continuous curves in Fig. 6.8 represent the functions

$$\epsilon(E)\,\Delta\Omega = a_0 + a_1\,E + a_2\,E^2 + a_3\,E^3 + a_4\,E^4, \qquad (6.4$$

with the parameters determined by least square fitting of the calculated efficiencies. The parameter values obtained in this way are given in Table 6.1.

Table 6.1: Parameters obtained from the fit of Eq. (6.4) to the determined efficiency.

Crystal	a_0	a_1	a_2	a_3	a_4
LiF	2.574E-05	-1.552E-08	3.339E-12	-2.724E-16	7.719E-21
PET	1.619E-05	-1.355E-08	4.649E-12	-2.896E-16	

Conclusions

- A general-purpose Monte Carlo program for the calculation of ionization depth distributions and x-ray spectra produced by kV electron irradiation has been developed. The code is based on the PENELOPE subroutine package, which has been suitably modified to extend its range of application to lower energies. In particular, it incorporates a new double differential cross section for bremsstrahlung emission, which combines a modified Bethe-Heitler DCS with the Kirkpatrick-Wiedmann-Statham angular distribution. Ionization of inner-shells by electron impact is described by means of an optical-data model proposed by Mayol and Salvat (1990). Interaction forcing is systematically applied to both bremsstrahlung and impact ionization to improve the efficiency of the simulation. The simulation program is applicable to samples with arbitrary geometries (multilayers, particulate samples, etc.).

- A systematic method for the measurement of ionization cross sections by electron impact, using the electron microprobe, has been proposed and applied. Measurements of ionization cross sections for Ni, Cr and Cu have been performed, from threshold up to 40 keV. Our results provide the electron-energy dependence of the ionization cross section to an accuracy of about 3%. The transformation to absolute cross section values increases the global uncertainty to about 12%. The comparison between experiment and various theoretical formulas confirms that the optical-data model yields a more reliable energy dependence of the ionization cross section in the energy range of interest in microanalysis. Further work to reduce errors in the determination of the target mass thickness is required to draw a definite conclusion about its accuracy in absolute magnitude.

- Simulated depth-distribution of ionizations and surface ionization, for different homogeneous targets and energies, have been shown to be in satisfactory agreement with experimental data taken from the literature.

- We have performed systematic measurements of the surface ionization for Ni Kα, in Cu films of 40.5, 67, 100 and 196 nm deposited on a wide variety of substrates covering the periodic table, and for incident electron energies between 10 and 30 keV. Owing to the difficulties in preparating the targets and to the smallness of

the peak-to-background ratio of the measured peaks, experimental uncertainties could not be reduced below 5%. Results from simulation of these experiments have been found to agree to within 5% with the measured data. We have derived a new scaling rule, which gives the surface ionization in terms of the bulk values of the substrate and the overlayer. Simulated ionization distributions for layered targets have been presented.

- The reliability of our simulation code has been globally assessed by comparison of measured x-ray spectra with simulation results. Absolute x-ray spectra have been measured using the energy-dispersive spectrometer, for different targets and irradiation conditions. The result of the various experimental sources of error lead to an overall uncertainty of 7-8%. The agreement between simulation and experiment is satisfactory in the "meaningful" region of the spectra (say, between 3-15 keV), where the detector efficiency is essentially constant. Comparison of simulated and measured x-ray spectra obtained with the wavelength-dispersive spectrometer allows us to derive the absolute efficiency of the latter as a function of the x-ray incident energy. This information is essential for standardless x-ray microanalysis using wavelength-dispersive spectrometers.

- In short, we have developed a realistic Monte Carlo code adequate for the simulation of x-ray generation by electron irradiation of samples with complex geometries. We have already demostrated its usefulness for EPMA of layered specimens. Although further work is required to include L- and M-shell ionization, the code has an evident potentiality for quantitative EPMA of samples with complex geometries. With the increasing availability of fast parallel computers, the day where simulation can be used as the basis of quantification procedures seems not too far in the future.

Appendix A

Sampling procedure for bremstrahlung emission

In this appendix we describe the algorithm used to sample the initial direction of bremsstrahlung photons from the KWS distribution (1.38),

$$p_{\mathrm{KWS}}(\cos\theta) = N_\theta \frac{\sigma_x(1-\cos^2\theta)+\sigma_y(1+\cos^2\theta)}{(1-\beta\cos\theta)^2}.$$

We first note that this distribution can be cast in the following form

$$p_{\mathrm{KWS}}(x) = u_1 p_1(x) + u_2 p_2(x) + u_3 p_3(x) \tag{A.1}$$

where $x \equiv \cos\theta$ and

$$p_1(x) = N_1 \frac{1-x^2}{(1-\beta x)^2}, \qquad p_2(x) = N_2 \frac{1}{(1-\beta x)^2}, \qquad p_3(x) = N_3 \frac{x^2}{(1-\beta x)^2} \tag{A.2}$$

are distributions, normalized to unity, with normalization constants

$$N_1 = \frac{\beta^3}{2[-2\beta + \ln(1+\beta) - \ln(1-\beta)]} \tag{A.3}$$

$$N_2 = \frac{1-\beta^2}{2} \tag{A.4}$$

$$N_3 = \frac{\beta^3(1-\beta^2)}{2\{2\beta - \beta^3 + (1-\beta^2)[\ln(1-\beta) - \ln(1+\beta)]\}} \tag{A.5}$$

The relative weights in equation (A.1) are given by

$$u_1 = \frac{N_\theta \sigma_x}{N_1}, \qquad u_2 = \frac{N_\theta \sigma_y}{N_2}, \qquad u_3 = \frac{N_\theta \sigma_y}{N_3} \tag{A.6}$$

The distribution $p_2(x)$ can be sampled by using the inverse transform method, which gives the sampling formula

$$x = \frac{2\xi - 1 + \beta}{2\beta\xi + 1 - \beta}, \tag{A.7}$$

where ξ is a random number uniformly distributed in the interval (0,1).

The distributions p_1 and p_3 can be rewritten as

$$p_1(x) = \frac{N_1}{N_2} r_1(x) p_2(x), \qquad r_1(x) = 1 - x^2 \tag{A.8}$$

$$p_3(x) = \frac{N_3}{N_2} r_3(x) p_2(x), \qquad r_3(x) = x^2 \tag{A.9}$$

Since $r_1(x)$ and $r_3(x)$ are smaller than 1, a rejection method can be used to sample x from p_1 and p_3.

The sampling algorithm for the combined distribution (A.1) is:

1. Sample an integer i(=1,2,3) from the point probabilities

$$\pi(1) = \frac{u_1}{\sum u_j} = \frac{N_\theta \sigma_x}{N_1}, \quad \pi(2) = \frac{u_2}{\sum u_j} = \frac{N_\theta \sigma_y}{N_2}, \quad \pi(3) = \frac{u_3}{\sum u_j} = \frac{N_\theta \sigma_y}{N_3}. \tag{A.10}$$

2. Sample a value t from $p_2(t)$ using eq. (A.7).

3. If $i = 2$, deliver $x = t$

4. If $i = 1$, generate a random number ξ

   (a) If $\xi > r_1(t) = 1 - t^2$, go to step 2

   (b) Deliver $x = t$.

5. If $i = 3$, generate a random number ξ

   (a) If $\xi > r_3(t) = t^2$, go to step 2

   (b) Deliver $x = t$.